University of Alberta

Microstructural Characterization of Chromium Carbide Overlays and a
Study of Alternative Welding Processes for Industrial Wear Applications

by

Steven Douglas Borle

A thesis submitted to the Faculty of Graduate Studies and Research
in partial fulfillment of the requirements for the degree of

Master of Science

in

Welding Engineering

Department of Chemical and Materials Engineering

Abstract

Microstructural features of chromium carbide overlays (CCOs) were examined in this work. It was found that the microstructures can contain unmelted alloy powders. It was also shown that the structures of the primary M_7C_3 carbides are long hexagonal rods. Change in the microstructure from the top to the bottom of the welds was found to be caused by compositional changes. Understanding these and the other microstructural characteristics of CCOs will help develop products that have better and more uniform wear resistance throughout. The effect of changing process parameters in SAW and the use of alternative welding processes of LBW, GMAW, and PTAW were also examined. It was found that as the balance was decreased in SAW the amount of dilution declined, which led higher amounts of hypereutectic microstructure, higher volume fraction of primary carbides, and larger primary carbide size.

Acknowledgments

Table of Contents

List of Tables

List of Figures

1.   Introduction

1.1.   Relevance of SAW CCOs

The cost of abrasive wear has been estimated to range between 1% and 4% of the gross national product of an industrialized nation. This high number can be attributed to the fact that eighty to ninety percent of machine parts fail because of surface wear.[1] In Canada alone wear is estimated to cost $2.5 billion a year [2]. In order to cut down on the cost of wear hard facing or the application of overlays is employed. Overlaying is a surface treatment aimed at improving the surface properties of metals, in which a welded overlay is deposited onto the surface of a substrate to improve the parts resistance to wear, oxidation, corrosion, or impact. It is applied to parts exposed to wear environments in order to protect them and to extend their service life [3]. There are a number of different types of material systems that are employed as overlays; this research focuses on chromium carbide overlays (CCOs).

CCO's are used in circumstances where metals are undergoing wear caused by abrasion, impact, erosion, corrosion and various combinations of these different wear modes [4-7]. CCO's are used in a large number of industries including mining, mineral processing, cement production and pulp and paper manufacturing [8-10]. Some specific examples of their uses in the oils sands include crusher teeth, hydro transport screens, and centrifugal pumps, wear-plate for truck bed liners and in pipelines used for slurry transport [7, 11-13]. One of the reasons for their large success across numerous industries is that in comparison to other overlay types such as WC based overlays and some polymer liners, CCO's tend to be relatively inexpensive and easy to apply [13, 14].

These overlays have high wear resistance because they contain 2-6 wt. % carbon and 8-35% chromium which combine to form M_7C_3 carbides. M_7C_3 has good wear resistant properties because of it high hardness of around 1500-1700 HV[15]. The wear resistance of these overlays can vary greatly and is often hard to predict. However, the volume percent of primary M_7C_3 carbides is often a good indicator of the relative wear resistance of similar overlays.

Even with their extensive use there are still a large number of areas that are not thoroughly understood and equally a large number of possibilities for improvement. This work will look at characterizing some of the less understood microstructural features and

delve into contradictory arguments concerning CCOs. Along with the microstructural characterization the effect that the process has on the overlays properties will be examined. The submerged arc welding (SAW) process is one of the most commonly employed processes for CCOs due to its high productivity and deposition. The possibility of improving production or performance of CCOs by adjusting the welding polarity using alternating current (AC) welding and contact tip to work piece distance (CTWD) will also be examined. This research will also look at some alternative welding processes for CCOs including gas metal arc welding (GMAW) process, which is a common alternative to SAW and two welding processes plasma transferred arc welding (PTAW) and laser beam welding (LBW) which are not known to be used substantially for the application of CCOs.

1.2. Description of Process

The bulk of the research revolves around the production of overlays using Submerged Arc Welding. [16]. There are many advantages to SAW including no ultraviolet radiation, little fumes and spatter. In addition to these advantages the process achieves high penetration, high weld quality and high deposition rates. SAW does suffer from some disadvantages such as the need for slag and flux removal and the fact that welding is confined to the 1G position [17]. When using SAW for chromium carbide overlays a powder that is high in alloying elements such as chromium, carbon, manganese, and molybdenum is placed down in front of the welding head. The welding head then moves forward welding over the powder with a low alloy steel wire while performing a weave function in order to increase the width of the weld bead. In SAW the weld pool and arc are protected by shielding gases and slags that are formed as the granular flux is melted[17]. Fluxes are used to get acceptable weld deposits in SAW, SMAW and FCAW welding processes. In order to work effectively the flux must have a melting range such that the weld metal solidifies before the molten slag does and the slag must have a density such that it floats to the top of the weld pool and collects there. The flux also acts to help maintain the arc and reduce spatter. Another important characteristic of fluxes is the slags ability to detach from the solidified weld deposit [18].

The ability to easily adjust the final composition by altering the composition of the powders is an advantage of using this process. CCO`s are often produced using SAW on large plates that are then worked, plasma cut, and welded into desired shapes. Another common use is cladding of pipes. For large diameters this can be done using SAW but for

2

smaller id's flux core is commonly used. The process is also highly automated which helps to increase the productivity of the process, these are huge advantages in a market such as Alberta with skilled labour shortages.

1.3. Challenges

CCO's commonly have transverse cracking that result from contraction of the weld pool during cooling [13]. This is commonly referred to as relief cracking, check cracking or tension cracking it is acceptable as long as the crack width stays below designated sizes and does not continue into the base plate [17, 19].
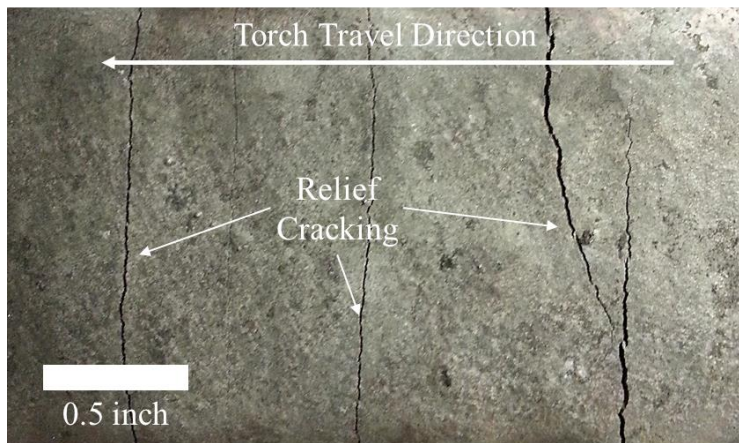
Figure 1-1: Relief Cracking

While the cracks are undesirable because they can lead to crack propagation during service of overlays they may be beneficial because they relieve contraction stresses and may help prevent spalling[20].

Other problems that can arise with the process is the large amount of distortion in the plates during welding. To overcome this problem a heavy duty clamping system must be employed along with careful observation from an operator to make needed adjustments based on any varying CTWD caused by the distortion. A downside to SAW is that it can only be performed in the flat position. The large and cumbersome equipment involved in SAW means it cannot easily be done manually which makes it a difficult process to use for repair of weld defects that occur during production or in the field.

This is easily solved by using a different process such as FCAW for the small repair jobs on the larger sheets as FCAW is much more flexible process for these small jobs and there are already many commercially available flux core wires with composition ranges

suitable for the COO's. One advantage is that some wires can are all position capable. This process still suffers from the problem of dilution that SAW encounters but in most cases the welding procedures of the overlay accounts for this problem by calling for minimum of 2-3 layers of the overlay. One drawback to the flux core wires is that they tend to experience problems with spalling of thicker sections made with multiple passes.

1.4.   Purpose of this Thesis

The purpose of this thesis is to examine and discuss microstructural features that unclear, conflicting or not discussed in previous work. With a better understanding of the microstructure it should be easier to control and produce an overlay with the desired properties. This work also looks at possible process improvement that has not been explored for CCOs. The work with process control will allow CCOs to be produced with a higher level of control and productivity of a currently industrially produced product.

1.5.   Thesis Outline

The following chapters will first discuss the appropriate methodology for sample preparation and analysis since there are many more intricacies involved with the analysis of CCOs than conventional welding. The analysis of some of the more unclear, unexplained microstructural features are then examined including rice crispies, rod vs. blade, and segregation. The last few sections deal with the actual production of CCOs. Firstly the ability to replicate an industrial scale product on a research level is examined. This is important as one of the goals of this research is to improve a product produced industrially that currently suffers from difficulty in reaching needed mechanical and microstructural properties. The effect of cooling rate, contact tip to work piece distance (CTWD) and balance in AC welding are all examined. The last section deals with the effect of different processes on CCOs, how they affect the microstructure and some of their advantages and disadvantages.

2.   Physical Metallurgy of CCOs

2.1.   Solidification modes of CCOs

The microstructure of chromium carbide overlays is largely dependent on the composition of the weld metal. As shown in Figure 2-1 the composition of the overlays

tend to fall in the range of the box which between 8-35% Chromium and 2-6% Carbon [4, 17, 21, 22].
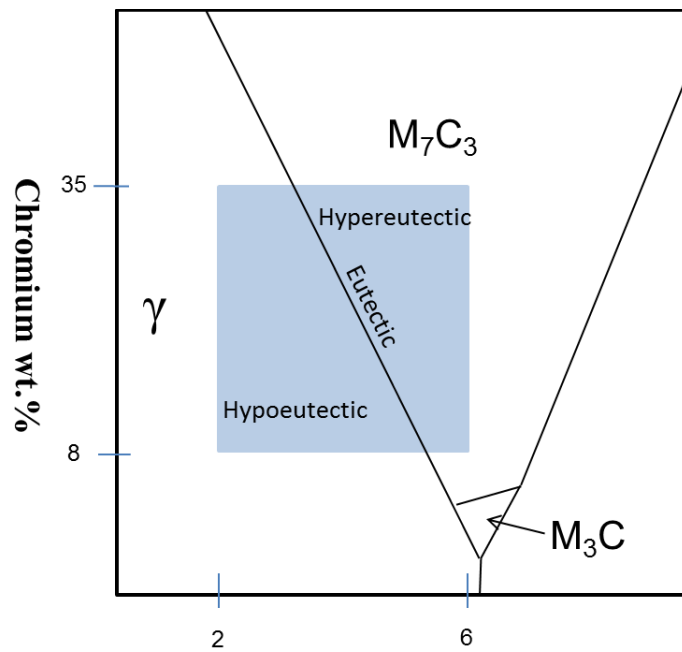
Figure 2-1: Pseudo Ternary Showing Composition Range of CCO's

This range of compositions means that there are three possible categories that the resulting solidification paths. These solidification paths can lead to hypoeutectic, hypereutectic or eutectic microstructures [22-24]. Examples of compositions where these different microstructures solidify from is shown in the simplified pseudo ternary phase diagram in Figure 2-2.

Three possible
solidification paths

A-Hypoeutectic

B- Eutectic

C- Hypereutectic
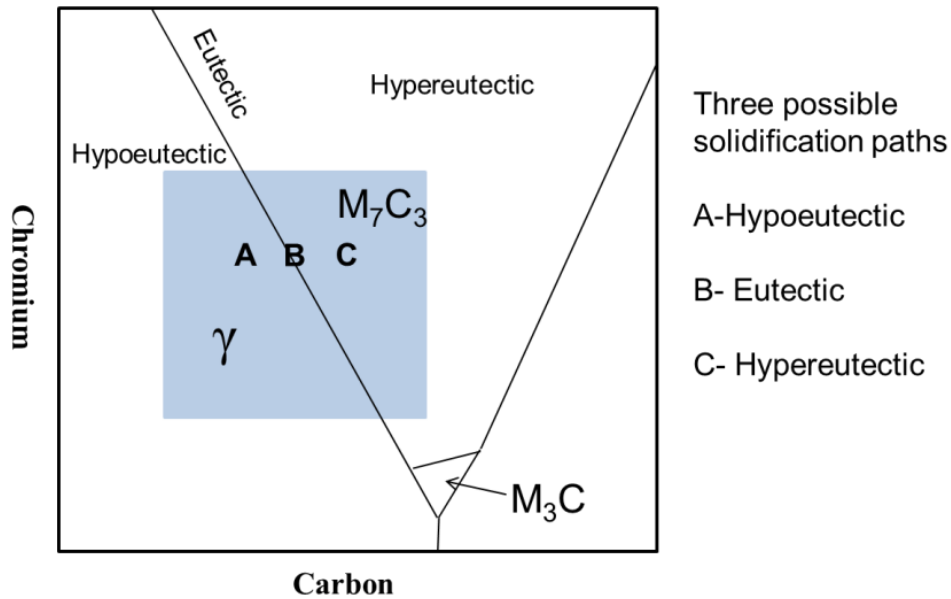
Figure 2-2: Illustration of three solidification possibilities

2.1.1 Hypoeutectic

In the case of a composition that would result in hypoeutectic microstructure such as one represented by point A in Figure 2-3 the solidification would begin at point A as primary austenite (γ) [23]. During the solidification of the austenite there is a pronounced amount of recalescence after the solidification of primary austenite. [25]. As the solidification of primary γ continues as shown in Figure 2-3 (a) the overall composition changes in the direction of the arrow because of rejection of Cr and C into the surrounding liquid [26]. Then as illustrated in Figure 2-3 (b) the overall composition reaches the eutectic line; at this point the solidification becomes a eutectic structure of γ and M_7C_3[27, 28]. This eutectic structure fills in the spaces between the previously solidified dendrites. The previous growth of the austenite constrains the growth of the eutectic carbides which causes them to be less faceted in comparison to eutectic carbides in hypereutectic and eutectic alloys [29].

6
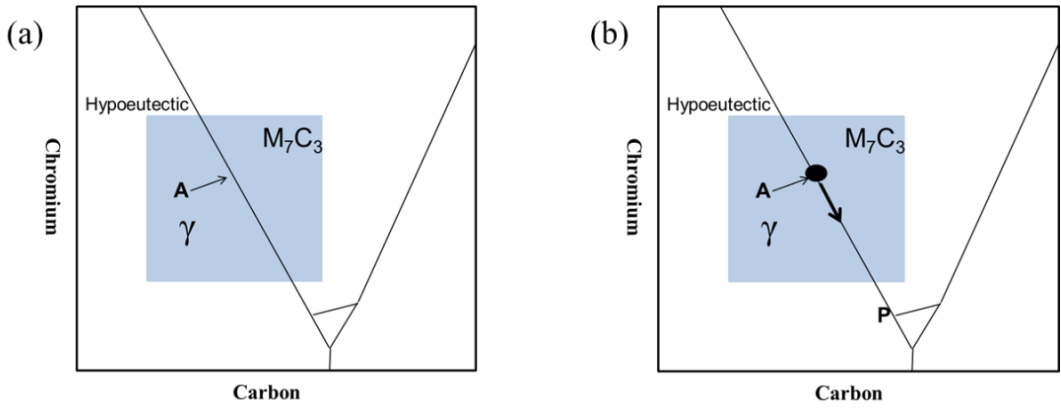
Figure 2-3: Hypoeutectic solidification path

Solidification then continues as a eutectic until all of the liquid is consumed unless there is still liquid left when the overall composition reached point P. Point P represents the peritectic reaction $L + M_7C_3 \rightarrow M_3C$. If it reaches this point there will be a peritectic reaction that will cause the rims of the M_7C_3 carbides to transform to M_3C. The peritectic is quickly stifled if it does occur, as the M_3C forms on the outside of the M_7C_3 carbides, which means that the M_7C_3 can no longer react with the liquid [30]. In the majority of cases this does not occur because this reaction is suppressed by the addition of alloying elements such as manganese and molybdenum [30]. Examples of the final microstructure of a hypoeutectic alloy are shown in Figure 2-4 and Figure 2-5. In general the hypoeutectic alloys are most commonly applied and produced in the casting method [24].
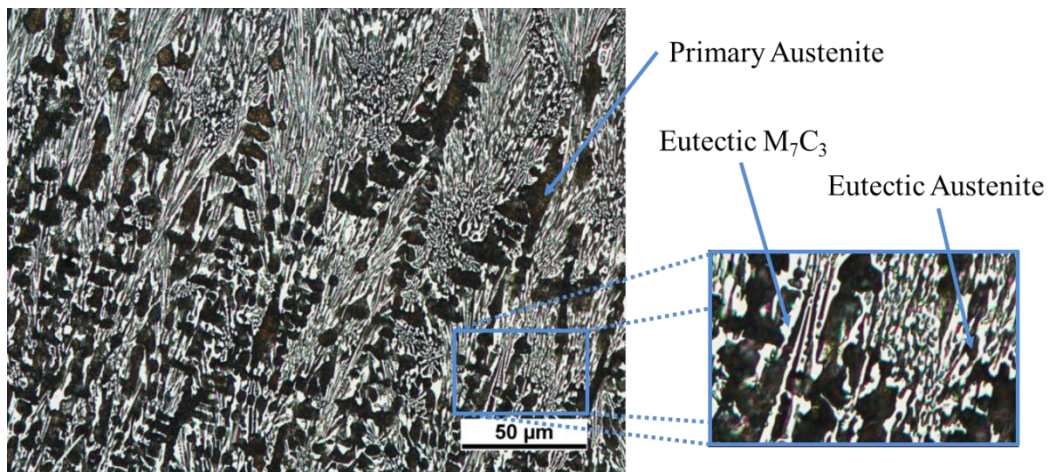
Figure 2-4: Optical micrograph of hypoeutectic microstructure of primary austenite dendrites surrounded eutectic M_7C_3 and austenite
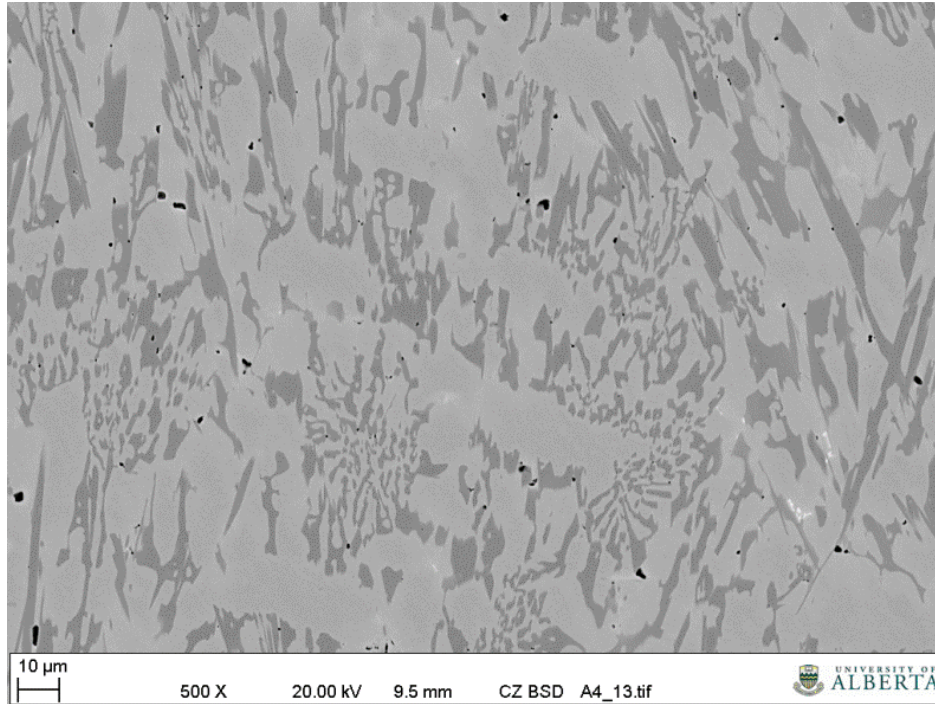
Figure 2-5: Scanning electron microscope (SEM) backscattered electron detector (BSD) image of hypoeutectic microstructure

2.1.2 Eutectic

In the case of eutectic or near eutectic (3-4 wt% C) alloys the composition of the alloy is very close to the eutectic line of the phase diagram as represented by point B in Figure 2-6 [17]. In this case the solidification starts as a eutectic of austenite and M_7C_3 carbides and does not solidify as anything else, unless as is the case for hypoeutectic alloys the composition of the alloy reaches the peritectic point before solidification is complete.[27]
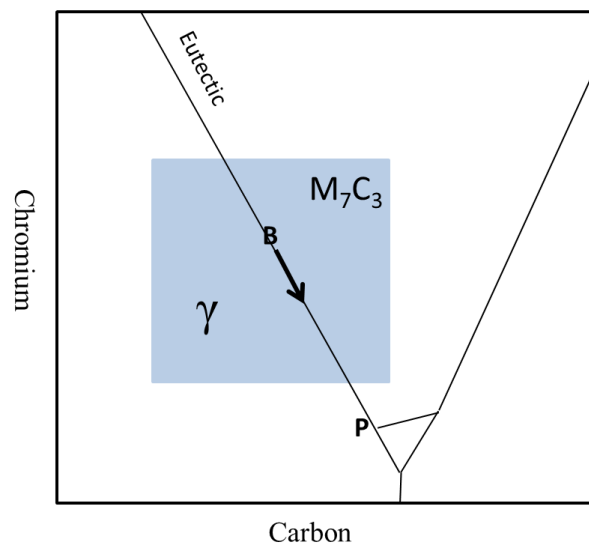
Figure 2-6: Eutectic solidification path illustrated on pseudo ternary

The resulting microstructure of eutectic austenite and carbide can be seen in Figure 2-7 and Figure 2-8 . The eutectic can either be rosseta like morphology as shown in the Figure 2-7 or can be fibrous bundles [29, 31, 32].
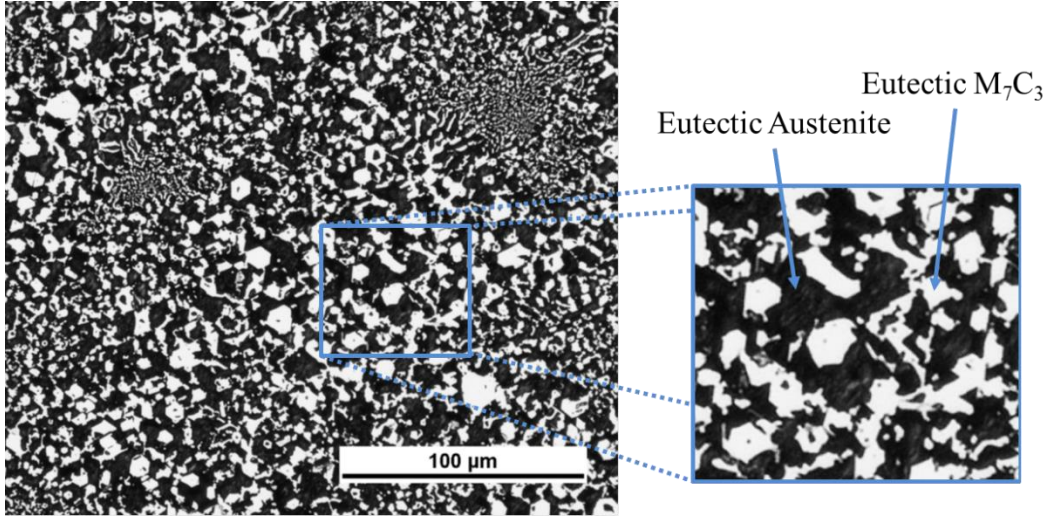
Figure 2-7: Optical micrograph of eutectic microstructure of austenite and M₇C₃

The eutectic cells are finer at the center of the eutectic cells and larger at the edge. This is attributed to the fact that as solidification progresses the amount of undercooling decreases because of the latent heat released during solidification. This causes the carbides that are formed last to be coarser [31].

In other cases the morphology of the eutectic carbides is very different. In this case the eutectic is bundles of fine fibrous carbides caused by high cooling rates [32].
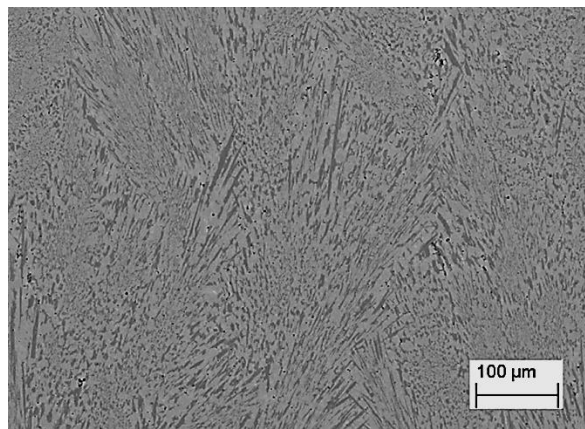
Figure 2-8: BSD imaging of fibrous eutectic

9

2.1.3   Hypereutectic

In the hypereutectic case such as a composition corresponding to point C in Figure 2-9, usually starting at around greater than 3.5-4 wt. % C primary M_7C_3 is the first phase to form out of the liquid. The composition of the liquid moves toward the eutectic line as illustrated in Figure 2-9 (a) [17, 23]. As with the hypoeutectic case after the liquid reaches the composition of the eutectic the solidification changes to that of a eutectic as illustrated in Figure 2-9 (b). This results in a microstructure of primary M_7C_3 surrounded by the eutectic of M_7C_3 and austenite as shown in Figure 2-10 and Figure 2-11. [33-35]. As with the other two alloy types it is possible to get a peritectic reaction, but this is also commonly purposefully avoided in these alloys. In the case were it does occur in hyper eutectic alloys the large primary carbides do not react with the remaining liquid to form cores of M_7C_3 carbides surrounded by M_3C. This is because their surroundings are solid before the peritectic reaction occurs [9].
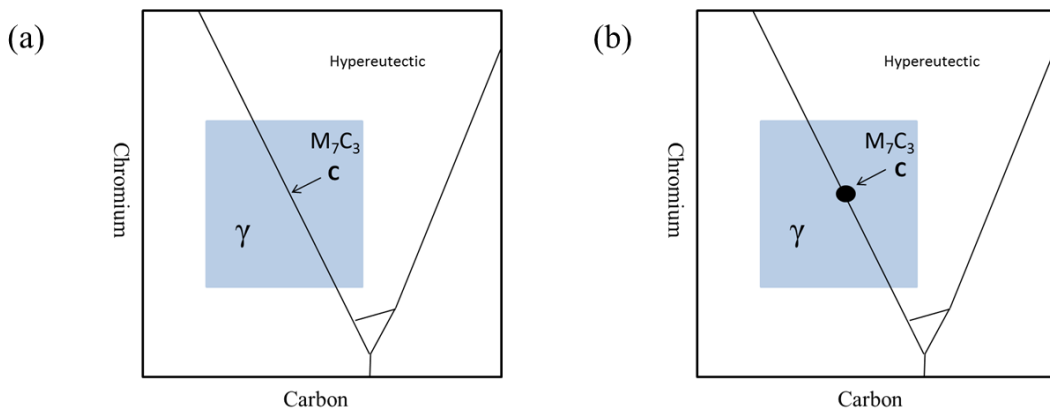
Figure 2-9: Hyper Eutectic Solidification

The primary carbide crystals formation and growth occur along their long axis which is parallel to the direction of heat flow [9, 24]. The primary carbides grow as a single crystal while the eutectic carbides consist of many different crystals [10]. The thin layer of austenite around the primary carbides is thought to be caused by depletion of chromium in the liquid surrounding the primary carbides [36]. Unlike hypoeutectic alloys, hypereutectic are most commonly applied using surfacing techniques because of its decreased cast ability [24].

10

Primary M_7C_3
Eutectic M_7C_3
Eutectic Austenite
50 μm
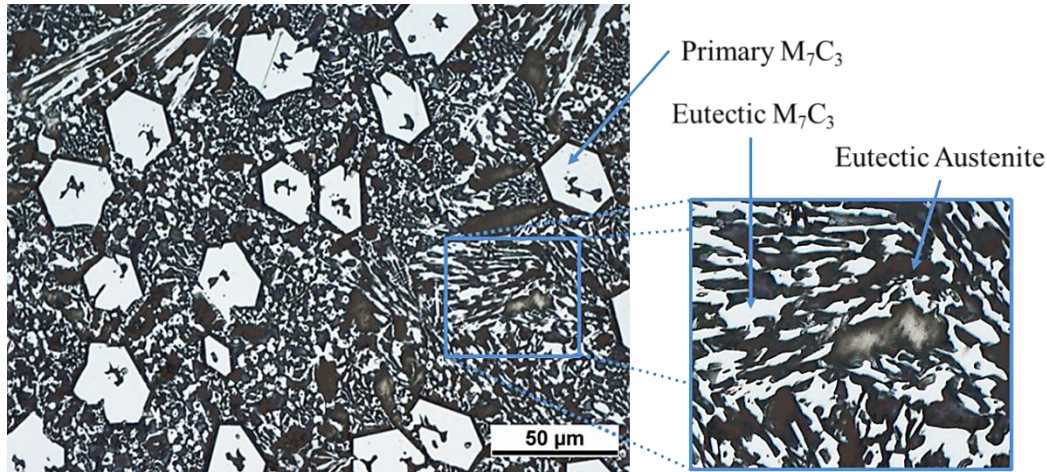
Figure 2-10: Hypereutectic Microstructure

Powell found that there is little recalescence after the nucleation of primary M_7C_3. The primary carbides in hyper-eutectic alloys grow rather slowly because of the low recalescence. They also believe that M_7C_3 carbides does not nucleate austenite, since there is no twining in the primary crystals so there are no crevices with re-entrant angles to facilitate nucleation of the austenite [25]. Others believe that the primary carbides do act as nucleation points for the eutectic reaction [29, 31, 33]. They also believe there is a large undercooling of the melt in contact with the primary carbides prior to nucleation of austenite. This means that at an undercooling of 140K below the M_7C_3 liquidus M_7C_3 nucleates and grows as a complex regular pattern until the remaining liquid undercools 100K before the austenite grows and rapidly fills the space between the carbides. [25].

100 μm
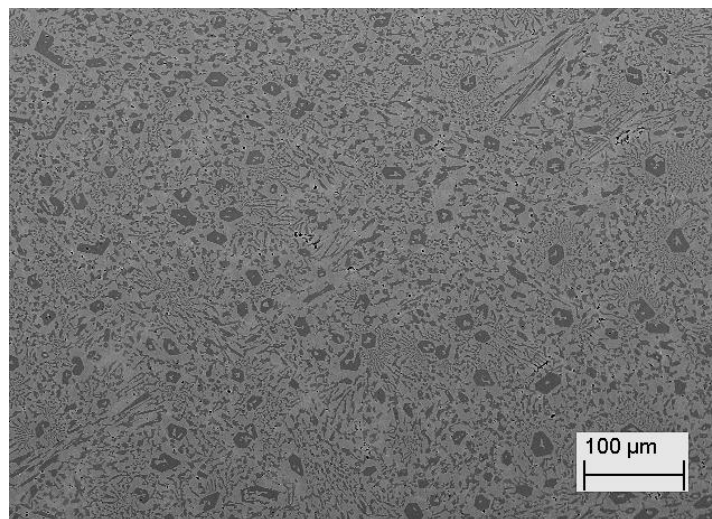
Figure 2-11: SEM BSD of hypereutectic microstructure

11

2.1.4 Other Solidification Modes

There are a few other variations to these three that can develop, such as precipitation of other primary carbides because of the addition of other carbide forming elements such as vanadium and titanium. As seen the primary phase is dependent on the composition of the overlay. In a hyper eutectic overlay the primary phase is M_7C_3, conversely in the hypoeutectic system the primary phase is austenite (γ). There are other primary and secondary phases possible such as MC, martensite and M_3C, $M_{23}C_6$ depending on the initial concentration [4, 35, 37].

An example is if there is Nb in the alloy system, Nb carbides begin to form first at roughly 1573 K. As the formation of these carbides continues a layer forms that is rich in Cr and Fe. This increase in chromium and iron raises the austenite start temperature, causing NbC act as nuclei for austenite. Because the partition ratio of Cr and C in austenite is smaller than one, Cr and C will be expelled into the surrounding area during the formation of austenite. Because of the short cooling time associated with welding there is no time for the Cr and C to diffuse which creates a favorable condition for nucleus formation of chromium carbide. This means the nucleus forms on the NbC and then the chromium carbide forms on the nucleus which leads to them clustering together [38] .

There is some disagreement however with that solidification path, an alternative hypothesis for solidification of a system with MC carbides is described by Zhou et al. They believe the MC precipitates out first followed by a small amount of M_7C_3. After that austenite and additional M_7C_3 forms after the liquid disappears, the mass fraction of M_7C_3 increases with a small reduction in the amount of austenite. After this M_7C_3 transforms into austenite below 1053K there can be a transformation of austenite to martensite [24].

2.1.5 Effect of Cooling Rate on solidification modes

One factor that may have a large effect on the final microstructure of overlays is the cooling rate. Little work has been done on the effect of cooling rate on CCOs [39], It has been studied more in white cast irons [9, 33, 40] and some correlations between the two systems can be drawn, but the large differences in CR's and dilution mean that there may be large differences in how the cooling rate affects the final microstructure.

Atamert and Bhadeshia also found that the phase compositions do not change significantly below about 1573 C. What this means is that the phase chemistries are almost entirely set immediately after solidification as a consequence of the high cooling rates associated with welding [36]. Wang and Li claim that water cooling during welding will promote the formation of primary carbides [38] .

Wang et al. also examined the effect of cooling rate and composition on CCO's. Water cooling of the hard facing with a higher Cr/C also causes the carbides to be aligned perpendicular to the top surface of the overlay. Normal cooling from the air and samples that were preheated to 523K are not aligned perpendicular to the surface. They found that as the Cr/C ratios decreased under natural cooling and there was an increased tendency for the alignment to be perpendicular to the surface. In the sample with the highest carbon amount (6.5wt%) they found that the primary carbides in the water cooled alloy were much finer and compact than the naturally cooled alloy. In the sample that was preheated the primary carbides were much coarser than those in the naturally cooled specimen as shown in Figure 2-12 [39].
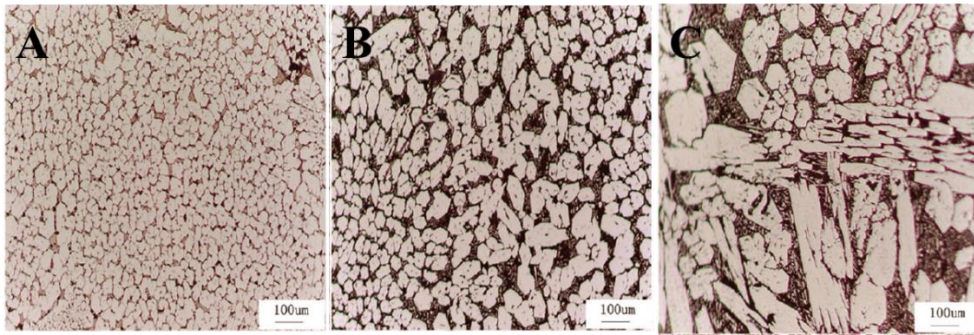
Figure 2-12: (A) Water Cooled (B) Naturally Cooled (C) Pre-Heateated [39]

The reason for this refinement is thought to be because as the undercooling increases atomic diffusion becomes more difficult and the probability of carbide nucleation increases. Since the time at high temperatures at which carbide growth occurs is decreased and the nucleation rate is increased the carbides become more refined [39].

Zhi et al found that the fluctuation caused by adding metal powders to the melt during the pouring of the liquid metal into the mold caused a decrease in the carbide size.[33] The fluctuation agents absorb copious heat and are melted which causes the temperature of the alloy to reduce sharply. This increases the solidification rate which in turn increases

the nucleation rate of the alloy refining the structure. Surface chill also produces a refinement of the carbide structure.[33]

2.2.   Other possible phase transformations

This section looks at two other phase transformations that can occur in CCOs when the situation is favourable. The peritectic reaction and austenite to martensite transformation are examined.

2.2.1   Peritectic

As previously discussed there is a possibility of a peritectic $L + M_7C_3 \rightarrow M_3C + (\gamma)Fe$ [41]. Dogan et al. examined an alloy in which the peritectic reaction occurred. Figure 2-13 shows the morphology of the M_3C. Note the core and rim structure that is representative of the peritectic reaction. It is also interesting to note that a large amount of peritectic is not apparent around the hexagonal shapes. [9]
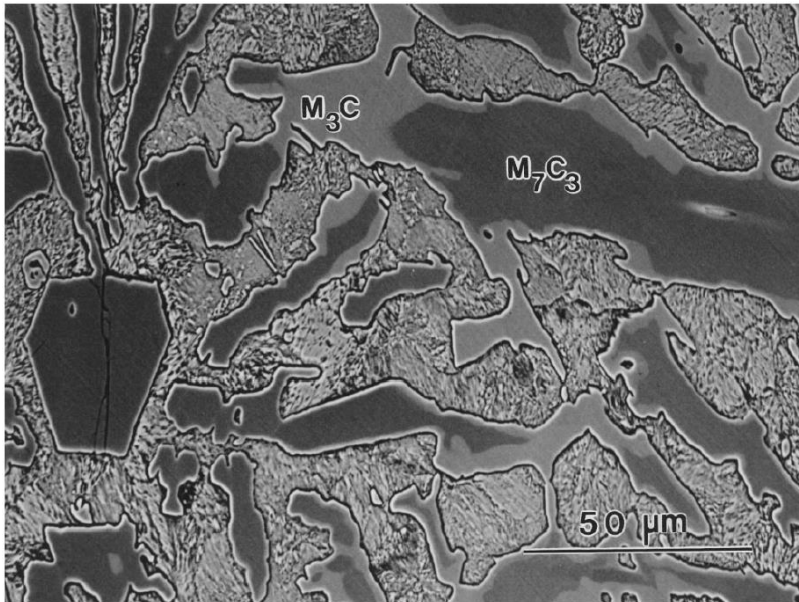
Figure 2-13: Backscatter electron microscope illustrating the product of preitectic reaction $(L_+ M_7C_3 \rightarrow M_3C)$ in hypereutectic 15Cr alloy [9]

In hyper eutectic alloys the large pro-eutectic carbides do not react with the remaining liquid to form theses cores of M_7C_3 carbides surrounded by M_3C rim because their surroundings are solid before the peritectic reaction. This means they most likely act as nucleation points for the eutectic reaction [31].

2.2.2 *Austenite to Martensite Transformation*

Carpenter et al. used SEM, XRD and TEM to perform microstructure characterization of Cr-C alloys and found that the depletion of Cr can lead to the transformation of austenite to martensite at the eutectic carbide edges as seen in the Figure 2-14. This segregation may be caused by the fact that carbon has a stronger affinity for chromium than it does for iron [42].
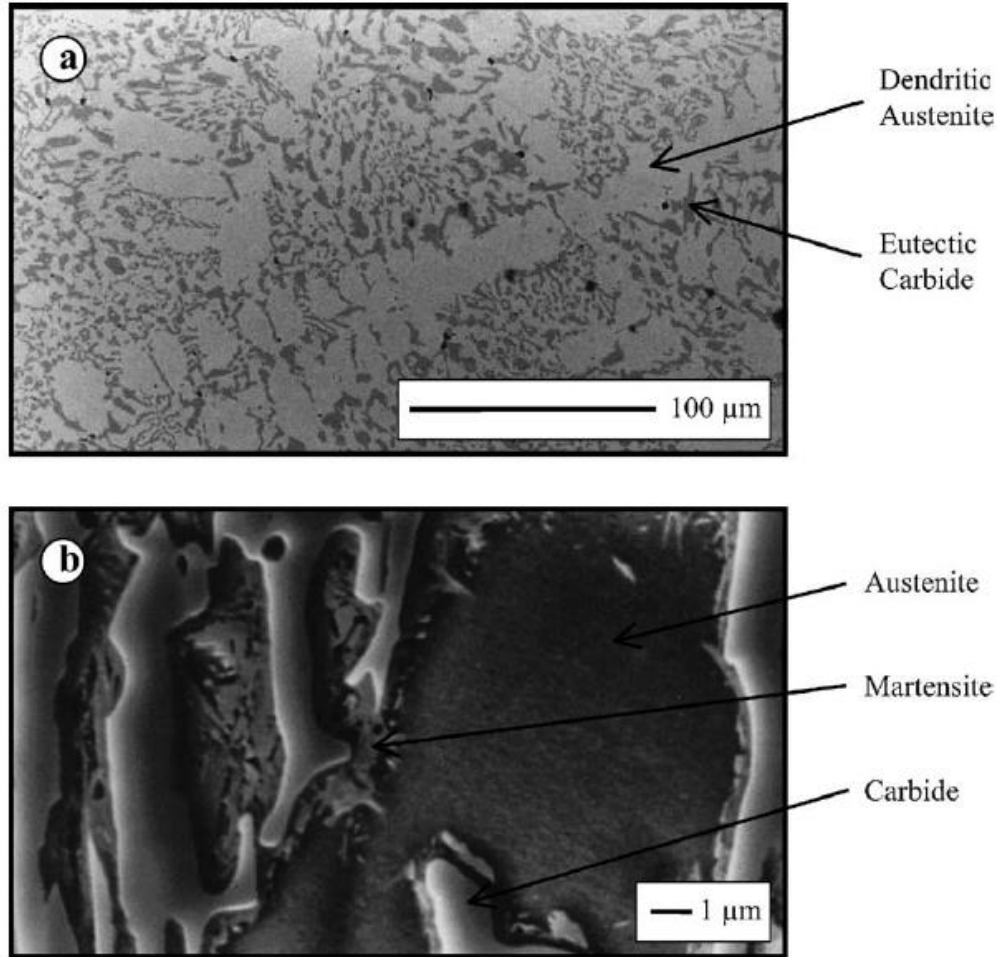
Figure 2-14: (a) Secondary electron micrograph showing the as-cast dendritic structure of the white iron (b) Secondary elctron micrograph showing martensite surrounding eutectic carbide[42]

Sabet et al. found that work hardening of the microstructure occurred during a wear test when the austenite became martensite through a stress induced transformation (SIT) mechanism. The transformation was more predominant and occurred on a larger scale with hypoeutectic and eutectic alloys [14].

15

2.3. Microstructure Constituents

This section looks at the specific phases that compose the microstructure of CCOs. Their morphologies along with what causes their differences are examined. The alloying elements that change their features and properties are also discussed.

2.3.1 Primary Austenite

When the alloy is hypoeutectic the first phase to form is austenite; this austenite that forms before the eutectic reaction is referred to as primary austenite [36] . Jiyang found that in white cast irons the morphology of primary austenite can follow two different morphologies. The first is a spiking morphology which long rod like dendrites show obvious orientation and parallel arrangement to form large coarse austenite grains. The second morphology is equiaxed dendrites this type of dendrite is arranged randomly and form fine austenite grains. In castings the rod like tend to form in molds along the wall where the equiaxed form when crystals nucleate and then form and grow inside the mold [43].

The primary austenite is not believed to be good a nucleant of the following eutectic solidification [31]. Atamert and Bhadeshia note that there is strong evidence that austenite is kinetically favored over ferrite because even when ferrite is the expected phase to be thermodynamically stable phase under non-equilibrium cooling conditions austenite is formed rather than ferrite [36]. The addition of chromium and carbon inhibit the development of pearlite and bainite. Further additions of molybdenum, manganese, nickel, and copper can avoid the formation of pearlite in almost any white cast iron. Other cast irons are purposefully high in silicon to help promote martensite formation [44].

Even though chromium is a ferrite former it helps to slow the rate of austenite decomposition which allows austenite to be retained under non-equilibrium cooling or in some cases transformed to ferrite and carbides or Martensite. Austenite is favored in cases where there is fast cooling after solidification, high Cr-C ratios, Molybdenum additions, and Nickel , Manganese, Copper. Molybdenum is especially effective because it reduces the rate of carbide precipitation. These carbides remove Cr from the austenitic matrix which therefore raises the martensite start (Ms) temperature. [35].

2.3.2 Primary M_7C_3 Carbide

When the alloy is hypereutectic the first phase to form is M_7C_3; this carbide that forms before the eutectic reaction is called the primary M_7C_3 carbide. A couple other names for the primary carbides M_7C_3 are primary carbide or pro-eutectic carbide [33] M_7C_3 carbides have a constant stoichiometry of M_7C_3 where M can be any carbide forming metal such as Cr, Fe, Mn, Mo [29]. Primary carbides are monocrystaline and have a dominant growth direction of [0001] [19, 29] .

Carbides tend to have high hardness and high melting points [43]. The high hardness of the carbides is major factor in the wear resistance of the overlays [15]. Because of their high melting temperatures in castings the first phase to form along the mold walls in hypereutectic alloys is primary M_7C_3 particles, these frozen particles are free to move about the mold cavity. They will often not re-dissolve because the superheat of the bulk will not be enough and the slow dissolution kinetics will slow the dissolution even if the melt temperature is high enough [31]. In the hyper eutectic alloy M_7C_3 forms first and then acts as nucleation points for the subsequent growth of M_7C_3 during the eutectic reaction [29].

Dogan et al. found that the carbide volume fraction increases with increasing carbon content and to a lesser extent with increasing Cr content [9]. Other researchers have also noted that increased chromium decreases the carbide size, however it is unclear if the cause in the increase in size was only linked to the increase in chromium amount or if it was the change in Fe/Cr mass ratios [43]. It has also been found that larger superheats and slower cooling rates increase the size of primary carbide rods [9, 43]. When fast cooling occurs the primary carbides are fine and difficult to distinguish from eutectic carbides while in slow cooling situations the rods are large and noticeable different from the eutectic carbides [43] .

Atamert and Bhadeshia found that chromium and manganese partitions preferentially into the carbides. Conversely they found silicon was rejected during the growth of the M_7C_3 carbides. They found that the eutectic M_7C_3 carbides have approximately the same composition as the primary M_7C_3 carbide [36].

Chang et al. found that additions of carbon decrease the average size of the primary carbides because it increases the nucleation rate of the primary carbides. They found this was caused because with the increase in number of solidifications of the primary carbide the latent heat increases causing a reduction in the undercooling. As the amount of

17

primary carbides increased there was a reduction of the undercooling at the solid/liquid interface which resulted in the decreased size of carbides [21].

2.3.3 Crystal Structure of M_7C_3

Zhang et al. examined of a number of the $Fe_{7-x}Cr_xC_3$ carbides using first principles in order to compare their structural stability and mechanical properties. They found that the electronic structures of $Fe_{7-x}Cr_xC_3$ carbides had a combination of metallic, covalent, and ionic characteristics. They also found that $Fe_4Cr_3C_3$ showed higher elastic moduli so it could potentially be a high strength hard material that still has ductile properties. Using theoretical calculations the hardness of $Fe_4Cr_3C_3$ should also be higher than the other carbides which are consistent with current experiments [45]. Fe_7C_3 crystals are ferromagnetic and have a curie temperature of about 523 K. [46].

There is some disagreement over the number of possible crystal systems for M_7C_3 carbides. Authors such as Fang et al. believe that there are only two different crystal structures possible, the hexagonal h-Fe_7C_3 and the Orthorombic o-Fe_7C_3 [46]. On the other hand Jiyang states that there are three crystal systems of Cr_7C_3 which are hexagonal, orthogonal, and rhombohedral [43]. The values for the lattice parameters of the three crystal structures are given in Table 2-1 .

Table 2-1: Lattice parameters of three possible crystal structures of M_7C_3 carbide [43]

Crystal system/type	Lattice constant nm	Density g•cm^{-3}
Hexagonal	$a = 0.688$ $b = 0.454$	
Orthogonal	$a = 0.454$ $b = 0.688$ $c = 1.194$	6.92
Rhombohedral	$a = 1.398$ $b = 0.452$	

Bauer-Grosse et al. also looked at a variety of M_7C_3 carbides to examine their crystal structure. They looked at synthetic Cr_7C_3 carbides, M_7C_3 carbides in cast irons, chromium steels along with $(Fe,Cr)_7C_3$ coatings formed using ion bombardment, and Fe_7C_3 carbide formed by crystallization of amorphous alloys. Previous research had proposed a hexagonal cell to describe Fe_3C_7 and orthorhombic and trigonal to describe M_7C_3

18

carbides. The three different cells are very similar and but can be thought of as three different oriented varieties with volumes that are one, two and four times the volume of an average hexagonal cell respectively. For all types of M_7C_3 carbides they found that the true structure was the orthorhombic structure with 1, 2 or 3 variants at 120 degrees from each other that can exist simultaneously in the same crystal. In primary M_7C_3 there are numerous planar defects in the $\{1\bar{1}00\}$ plane [47]

It appears from previous research that there may be a number of different crystal structures possible which are dependent on composition, production method, and phase solidification order.

2.3.4   Use of other Primary Carbides

While commonly the only carbide present in CCOs are M_7C_3 there are a number of other possibilities that can occur based on the chemical composition of the overlay. Other carbide types that are possible include M_3C, M_2C and M_6C and $M_{23}C_6$ [35]. These other carbides can form because of carbide forming elements such as Mn, Mo, W and V that are added to the weld metal. Theses alloying elements don't always form other primary carbides and can sometimes also be found in the eutectic carbides along with in the austenite [35, 38]. The addition of WC promotes the formation of WC rich intermetallic phases, which will increase the micro hardness and erosion corrosion performance [12].

2.3.5   Eutectic Carbides

In all three types of microstructure there is a point where the eutectic reaction occurs when austenite and M_7C_3 carbides form together. These carbides that form along with the austenite are called eutectic carbides. In hypereutectic alloys the eutectic carbides are generally not connected to the primary carbides [33]. In the case of hypoeutectic alloys austenite solidifies first followed by the eutectic solidifying in the large pools of liquid between the primary austenite. This unrestricted growth in between the austenite dendrites leads to rossetta type growth.[29] The third possibility is a eutectic composition where the solidification is of the eutectic is the first to occur. Dogan et al. found that the eutectic carbide size was the finest in eutectic alloys [9]. The presence of finer primary carbides increases the density of nucleation sites for eutectic solidification and accordingly, eutectic carbides are refined. [33] The TEM images reveal that the eutectic carbide rods are often made up of more than one crystal and in fact were often consisting of a cluster of crystals as shown in the following Figure 2-15 [37] .

19

The carbides in hypoeutectic alloys are randomly oriented, even adjacent rods have very different orientations [25]. As the amount of eutectic solidification increases the eutectic forms clusters that contain fibers of the M_7C_3 carbide and blades that radiate from the centers of the interdendritic spaces. The eutectic structure becomes completely fibrous when greater than 30% carbide is present. It appears that the fibrous type of eutectic grows rapidly as dendrites because of twinning mechanisms. It has also been shown that the fibrous eutectic carbide is interconnected which may be associated with the twinning occurring. In near-eutectic alloys the eutectic M_7C_3 carbides have been found to be interconnected in slightly hypereutectic alloys the rods are found to be arranged in a triangular pattern. It was found that the hypereutectic alloys had the same orientation over extensive areas of the specimen while for the hypo eutectic they were randomly oriented [25].
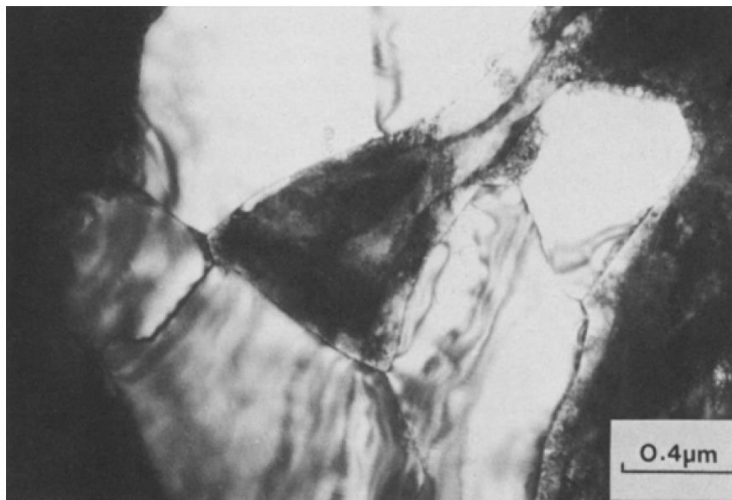
Figure 2-15: Cyrstal Boundaries in a cluster of eutectic M_7C_3 [37]

There appear to be two different textures of the eutectic carbide a rod and a blade like. [29] Jiyang found that the difference in the morphologies is caused by differences in the crystal structures. They found that the rod like ones follow a hexagonal crystal growth system and for the blade like the rhombohedral growth system is followed [43].

Laird et al. found rod and blades like carbides in hypereutectic, hypoeutectic and near-eutectic in white iron compositions. The differences in the texture were attributed to the differences in solidification sequence. As the solidification goes from hypereutectic to hypoeutectic the M_7C_3 carbides are more constrained during growth so the carbides become less faceted [29]. Dogan found that in hypereutectic alloys the blade like are more likely to form around the large primary carbides. He believes that a lower undercooling caused by the latent heat of formation during solidification of primary carbides lead to the blade like morphology in these locations. As evidence that the morphology is linked to the cooling rate they point out that the rod like is predominately found in circumstances opposite to around the primary carbides such as close to mold walls where the cooling rate is high [31]. Zhi et al. believe that the blade like morphology around the primary carbides is due to the fact that the primary carbides act as nucleation sites for austenite [33]. They also believe that there is coupled growth in the eutectic colonies because of strong micro textures and that the growth starts from a single nucleation site.[41]

Atamert and Bhadeshia have found that the composition of eutectic carbides closely matches the composition of primary carbides; however other researchers such as Zhou have found large differences in the composition of the eutectic carbides and the primary carbides [36, 48]. Chromium greatly affects the eutectic carbide. Increasing the Cr amount leads to and increases in the volume fraction of the eutectic carbide volume. Increasing the Cr content also increases the chromium content in the carbides which leads to an increase in the proportion of Cr to iron in the carbides which increases the carbide hardness [30].

2.3.6 Eutectic

While the previous section dealt with the eutectic carbides specifically this section deals with the eutectic as a whole which is also sometimes referred to as the matrix. Chromium is added to decrease matrix hardenability and increase corrosion resistance [38, 49]. Addition of chromium also decreases the amount of carbon in the eutectic [38]. Problems that can be caused by the alloying elements include under alloying where insufficient additions have been made to avoid the formation of pearlite. Over alloying can cause an over stabilization of austenite. Molybdenum suppresses pearlite formation and increases hardenability the amount added vary between 1-4%. Other alloying elements such as nickel and copper that are used to delay pearlite formation are more effective when added

with molybdenum. Molybdenum does not have much of an effect on Ms and the effect of it amplifying the effect of other alloying elements is not well understood. Molybdenum is somewhat expensive which has led to a tendency to attempt to decrease the amounts used [30].

Laird et al. found that silicon does not have any effect on the partitioning of C and Cr between the austenitic matrix and the M_7C_3 carbides during eutectic solidification. Silicon also does not have an effect on the eutectic carbide volume fraction or modify its shape [50]. When vanadium is added to an alloy it is found in the austenite matrix, eutectic carbides and primary carbides and in fine carbides with W and C. V can act to strengthen the matrix. Additions of tungsten also reinforce the matrix [38].

The eutectic is sometimes in the form of rossettas as shown in Figure 2-16. The eutectic carbide spacing and colony size is dependent on solidification and chromium content. The fracture toughness of white cast irons can be increased by a refinement of the eutectic carbides or a reduction in the continuity of the eutectic carbides [35]. Dogan attributes the fact that the eutectic cells are finer at the center of the eutectic cells and larger at the edge because as solidification progresses undercooling decreases because of the latent heat released during solidification. This causes the carbides that are formed last to be coarser [31]. In contrast Kumar believes that the change in size is related to the room for growth available. He believes that there are a large number of nucleation points and at the beginning of eutectic solidification the growth is less restricted. Since the resulting size of the carbides is proportional to available growth space at the later stages of solidification the carbides are much finer since there is less room for growth [26].
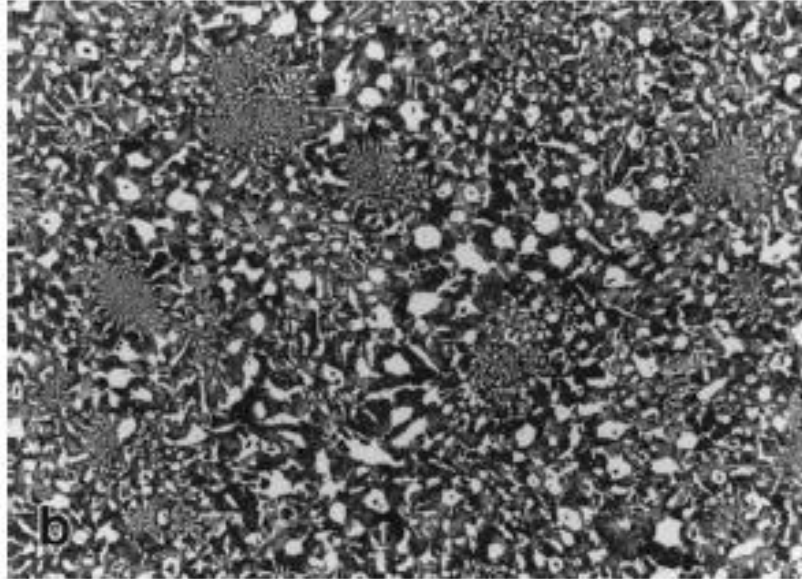
Figure 2-16: Rossetta like morphology of eutectic carbides [9]

2.4. Microstructural features

Some microstructural features that are particular to CCOs and will be discussed below include the cored structure of the primary carbides, the halo effect, rod vs. blade, and micro texturing.

2.4.1 Cored structure/ Growth of M_7C_3

An interesting characteristic of the primary carbides is that they often contain a different microstructure in the middle of the carbides compared to the M_7C_3 of the rest of the carbide. According to literature it appears that the cores can consist of austenite, martensite, eutectic or porosity [37, 51-53]. One portion of the growth of the carbides that is fairly well agreed upon is that they grow along their long axis in the direction of the heat flow in the [0001] direction [24, 51]. Unfortunately the growth of the primary carbides along their width is not well understood and there are a few of competing theories. For example Zhou et al. believe that the primary carbides continue to thicken after they nucleate until the composition of the liquid reaches the eutectic composition [48]. In contrast to this Ohide, T and Ohira, G. believe that during solidification primary hexagons have an inner core of liquid. The outer core of primary M_7C_3 then grows inward enclosing the eutectic melt. Because of poor photocopy quality what they mean by the structure is unclear but based on the text it is believed they were talking about a structure on the inside of primary carbides as shown in Figure 2-17 [53]. Jiyang et al. also

believe that the crystals grow inwards with their reasoning being that each side of primary carbide is smooth meaning that the growth is inward as the crystal is enveloped by its sides [51].
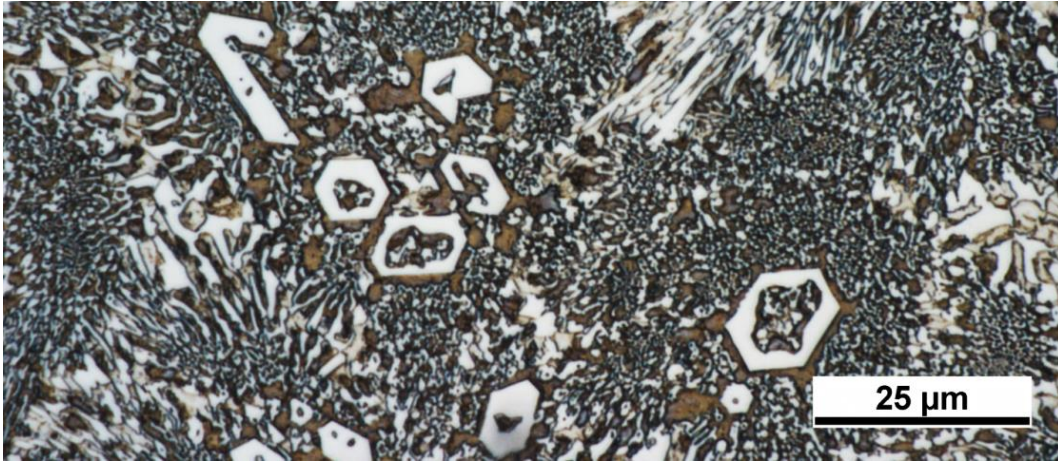
Figure 2-17: Primary carbides with eutectic microstructure in core

Though there is little literature on the primary carbides growth some inference may be taken from studies looking at eutectic carbides that have the same characteristic inner cores. Pearce examined the inner cores of the eutectic carbides and found that they were martensitic which he believed is caused by a decrease in the chromium and carbon caused the growth of the eutectic carbide in the vicinity. Because of this he believed that the growth is of hexagonal shell which grows inward with the remaining melt or shrinkage similar to the proposed by Ohide and Ohira for primary carbides [37]. Kumar however dismisses this possibility under the assumption that for this type of solidification to occur you would need nucleation sites similar to a mold wall present in the liquid which is a hypothetical case and not possible in real life [26].

2.4.2 Halo Effect

Another interesting characteristic of the primary carbides is the halo effect where the primary carbides are surrounded by a thin layer of austenite and then the eutectic structure starts as illustrated in Figure 2-18. This thin layer has approximately the same composition as the eutectic austenite which is believed to be because the both evolve over a narrow temperature range. Atamert and Bhadeshia believe that the halo is caused by a depletion of chromium in the liquid close to the primary carbides [36].
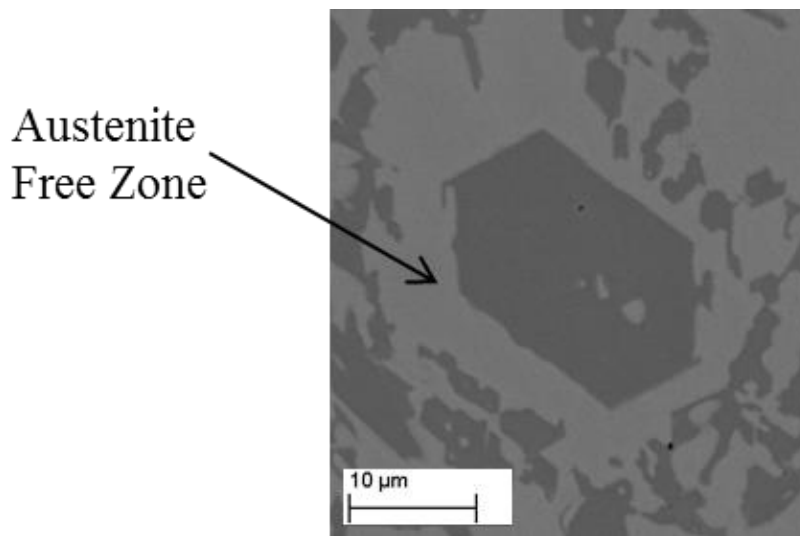
Figure 2-18: SEM BSD picture illustrating carbide free area around primary carbide

Gigliotti et al. have proposed one theory as to why there is often a primary phase that is surrounded by a layer or halo of the second phase. In general for a faceted-nonfaceted system a faceted phase is a good nucleant while a nonfaceted is not a good nucleant. They explain that halo formations can be explained in terms of the growth velocities of the phases involved and how they vary with undercooling and solute content. The reasoning given for these phenomena is similar to one proposed by Kofler for organic eutectics [54].

Kofler found that there is a composition-temperature area where coupled growth can occur. Coupled growth means that both phases are growing at the same temperature. The growth rate of phases were found to have two values one if its growing as a primary phase and a second one if growing as a secondary act of crystallization. The differences in growth velocities of the phases as secondary crystals indicate that the liquid composition tends to move to one boundary of the coupled zone where there is a definite leading phase. With this analysis the halo formation is explained; if for a given composition and undercooling the primary formation has moved and composition away from the coupled zone then a halo will be formed [54].

The phenomenon can be explained in Figure 2-19. If a composition of C1 is cooled at some temperature below TL1 primary α nucleates and grows the liquid composition follows the liquidus line and its metastable extension. At temperature T$\beta\alpha$ and composition C$\beta\alpha$, β is nucleated by α since the liquid lies in the coupled region eutectic

25

growth can begin immediately. On the other hand when an alloy of C2 cools from primary β will first form the liquid moves to composition Cαβ and temperature Tαβ before α is nucleated by β. This composition temperature point lies outside of the coupled region. At this point α has a higher growth velocity than β and thus α grows as a halo and moves the liquid composition back to the coupled region. The cooling rate and the amount of latent heat released determine the amount of recalescence [54].

Figure 2-19: Hypothetical phase diagram for a faceted-nonfaceted eutectic system. B, the faceted phase is the good nucleant. The coupled zone is skewed to the β side of the phase diagram [54]

An extension of Koflers theory extended to a faceted non faceted system where the non-faceted slower growing phase would be phase α. Because the coupled zone extends around the liquidus of the nonfaceted there will be a halo of non-faceted around the facteted phase but no halo of the faceted phase about the nonfaceted[54].

2.4.3 Microtexturing (equilateral triangles)

In hypereutectic alloy you can get a pattern of equilateral triangles as shown in Figure 2-20.

Figure 2-20: micrographs showing equilateral triangle pattern

Powell et al. note that in the carbide rods in these triangular arrays are vertical to the plane of section [19]. Deep etching technique shows that this is caused by the regular alignment of carbide rods [25]. These carbide rods within a eutectic grain are interconnected. Powell came up with a possible solidification process that causes this microstructure. He believes they are caused when cooling rates are approximately 25 K/s which lead to undercooling before nucleation and growth [19].

These microstructures can cause apparent differences in areas of the overlay. The can cause one area to appear bladelike and another area to have a rod like appearance because of growth of different grains. In this case the term grain is used to indicate a growth of a faceted-nonfaceted eutectic from a single nucleation center. It has been shown that these are different grains because Laue photographs and EBSD techniques showed the carbides within a given grain have the same orientation.[19]

2.4.4 *Rod vs. Blade*

Looking at previous research it appears that there may be two different morphologies of primary M_7C_3 carbides [21, 55]. Figure 2-21 shows the two types and their morphologies. The two morphologies look quite different with the rod being smaller and hexagonal in shape while the blade like have a larger length to width ratios that are much larger. Upon further examination however it becomes clear that these two different morphologies are

caused by how the samples are cut. Wang et al. showed how the rod like carbides were in the longitudinal direction and the lath-shaped ones were in the transverse and vertical directions, this showed the apparent morphology differences is related to the carbides orientation to the cut direction [56].
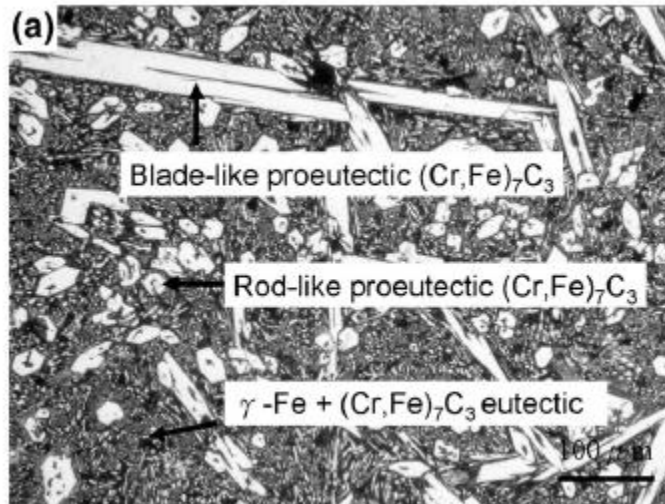
Figure 2-21: Difference in blade and rod like morphology of primary M₇C₃ carbides [21]

This orientation dependency is also seen in research by Liu et al. They found a random orientation of the M_7C_3 carbides but by adding an electromagnetic field they were able to align the carbides as represented in Figure 2-22 . By causing all of the carbides to align the blade-like carbides disappeared and the microstructure consists of only rod like carbides [55].
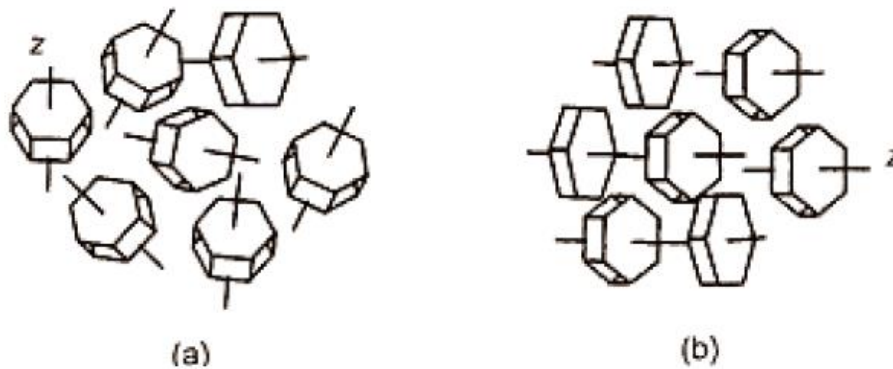
Figure 2-22: Schematic of the effect of Magnetization of primary carbides in an external magnetic field. (A) no alignment without a magnetic field (b) alignment with magnetic field [55]

Chang et al. also discussed how previous research has classified the morphology of the carbides into rod and blade-like. They found that the compositions of the two different morphologies are similar to one another. They also discuss how previous research had shown that the microstructure transitions from blade-like to rod-like as the composition of carbon increases. They believe that when the carbon content is low the number of nuclei sites of the carbides is fewer, which causes their growth directions to be random. When the nuclei sites is higher the growth is less random leading to more rod like and less bladelike primary carbides. They believe that this apparent difference in microstructure between samples is because of this difference in whether or not the growth is random causing differences in the carbides axis relationship to the viewing surface [21].

Literature from Triten, a company that produces CCOs makes note in a service publication that the appearance of the primary carbides vary based on how they are cut. When they are cut perpendicular to the crystal they appear hexagonal. Figure 2-23 is a schematic showing how the appearance of the carbides can change based on the angle of viewing compared to the length of the crystal. When they are not cut perpendicular they can appear needle like but regardless the two share the similarities that they usual contain a black cavity near there center and have very sharp corners [57].
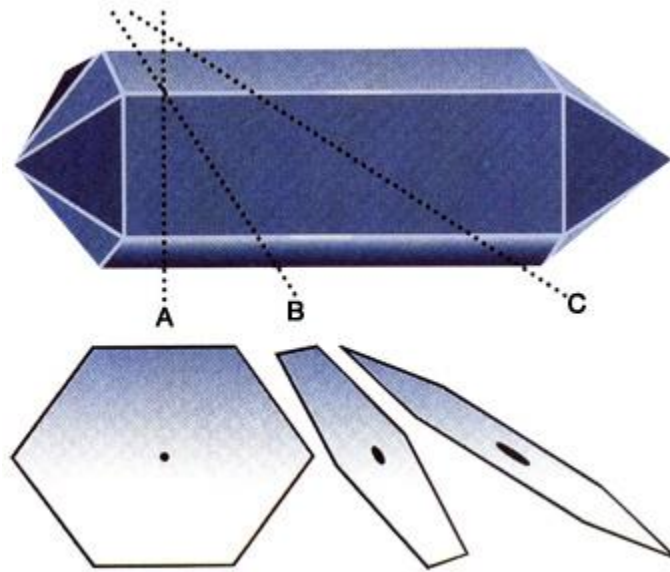
Figure 2-23: Schematic showing change in appearance of M_7C_3 carbide depending on viewing angle [57]

Another factor that makes the blade-like rod-like discussion less clear is the use of those two terms to describe the shape of the eutectic carbides rather than the primary carbides [9, 29, 58]. Figure 2-24 shows how the eutectic clusters can consist of rods in the middle and blades at the peripherals [58].
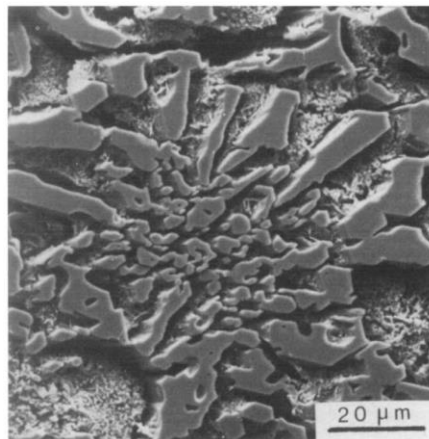
Figure 2-24: Eutectic colony deep etched showing rod like carbides in the middle of the eutectic colony and blade like ones at the edge of the colony[58]

An argument may be made that the rod-like/ blade-like differences in eutectic carbides can be explained using the same reasoning as with the primary carbides but previous research indicates that this is not the case. Powell and Lloyd used a deep etching technique to look at the morphology of eutectic carbide clusters in white cast irons. Figure 2-25 shows when a sample is cut parallel to the growth there is a distinct differences in the appearance of the rods and blades indicating they are distinct morphologies not caused by differences in sectioning orientation to the carbides [58].
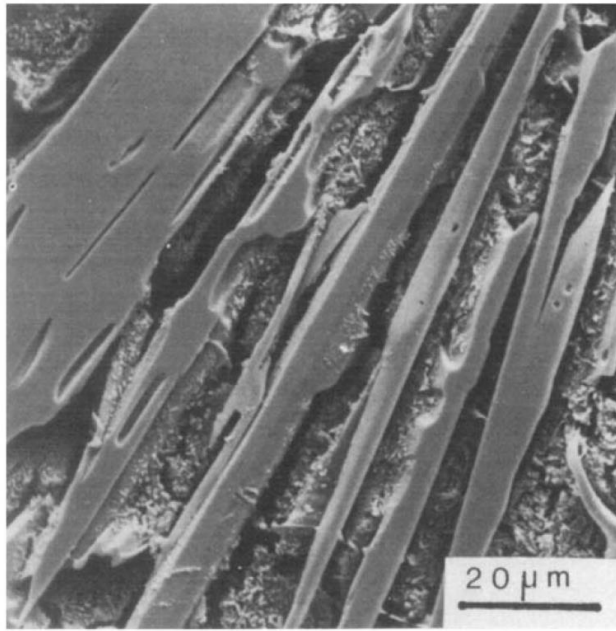
Figure 2-25: Eutectic carbide cluster sectioned parallel to growth direction, rods are apparent on the right hand side and blade like on the left hand side [58].

Dogan et al. have also examined the differences in eutectic carbides between hypereutectic, eutectic, and hypoeutectic alloys. They found that the morphology of the carbides are always rod like in the eutectic alloys but can be either rod or blade in the hypo and hyper eutectic alloys. In the hyper eutectic the pro-eutectic M_7C_3 alloys are always rod shaped. They pro-eutectic alloys are often surrounded by blade shaped carbides which they believe suggests that when undercooling is smaller the blade like ones are favored. Another area of the microstructure that may be corroborate this hypothesis is that close to the wall of castings there are more carbides that are rod like than the in the inner part of the cast [9].

Laird et al. also examined the differences in the morphology of three different compositions of white cast iron get the following results shown in Table 2-2.[29]

Table 2-2: Examination of three alloy types and the their carbide morphologies [29]

Alloy	Composition (Wt Pct)							Carbide Morphology	Carbide Volume Fraction
	Mo	Cu	Ni	Mn	Cr	Si	C		
A hypereutectic	0.5	0.1	0.3	0.5	28.8	0.2	3.2	hexagonal	35
B near-eutectic	1.9	0.8	0.4	0.7	20.2	0.5	3.0	hexagonal + blade	28
C hypoeutectic	0.0	0.0	0.4	0.5	18.4	0.3	2.2	blade	14

The reasons given for the differences in morphology were explained by their differences in solidification sequences. In the hyper eutectic alloy M_7C_3 forms first and then acts as nucleation points for the subsequent growth of M_7C_3 during the eutectic reaction which results in a microstructure consisting of mainly faceted hexagonal shaped carbides. The near eutectic alloy however first solidifies as austenite with the eutectic reaction occurring in large pools of liquid. Because of this the faceted hexagonal shaped carbides are allowed unrestricted growth among the Rosetta type structures. The growth of austenite in the hypoeutectic alloy constrains the growth of the M_7C_3 phase during the eutectic reaction, this results in less faceted carbides. [29] Jiyang found that the difference in the morphologies is caused by differences in the crystal structures. They found that the rod like ones follow a hexagonal crystal growth system and for the blade like the rhombohedral growth system is followed [43].

2.4.5 *Banding of microstructure in CCOs*

The microstructure of CCO's can be a mixture of hypoeutectic, eutectic and hypereutectic [19, 24, 59, 60]. Figure 2-26 shows how the microstructure of a SAW CCO can be hypereutectic at the top, eutectic and hypoeutectic at the bottom of the weld. This layering can occur because of differences in composition along the height of the weld [19]. It is unclear between solidification, segregation, diffusion, lack of mixing, and diffusion what the main cause of this microstructural layering. These different areas of microstructure are of interest because the primary austenite in the bottom of hypereutectic alloys will result in poor wear performance at the bottom of these alloys [59]
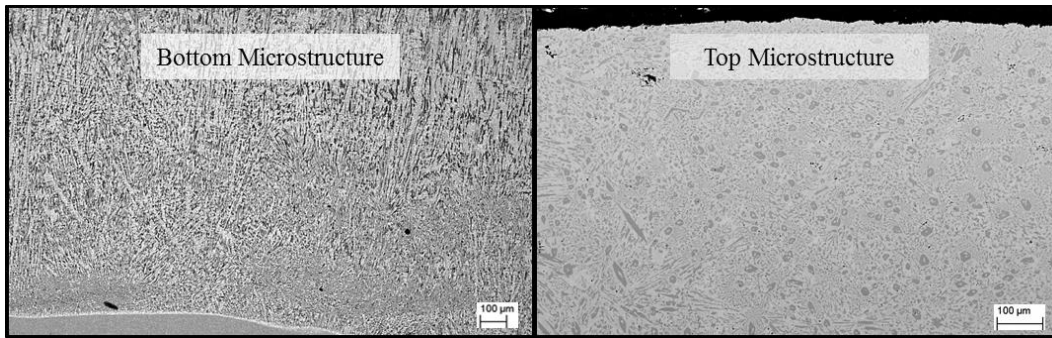
Figure 2-26: SEM BSE images of microstructure highlighting differences in the top and bottom of overlays

Dilution of the hard facing alloy by base metal is often noted as being a very important factor in the microstructure of hard facing because it can cause the weld composition and microstructure to vary from the intended properties. Normally the dilution or penetration is attempted to be kept at as low as possible values. A range of the dilution amounts for the processes studied in this paper are SAW single wire 30-60%, GMAW 10-40%, PTA 5-15%, and LBW 1-10% [17, 61].

In many cases multiple passes are used to overcome the problem of dilution but it is not always possible and may not always be straight forward. There are many factors during welding that can change the amount of dilution occurring. Some of these may be alternatives to multipass welding for dealing with dilution effects. Sannikov looked at how the effect of electrode stick out changed the weld geometry. He found that there was almost no change in joint width and reinforcement height while the depth of penetration decreased by about 40-50% going from 30 to 100mm electrode stick out. [62]. Lee et al. note that the microstructure of the overlays is very complex because of the large thickness of layers and because diffusion can occur between the layers due to the heat input during welding [63].

2.5. Effect of different alloying elements

Alloying elements play a huge role in the resulting microstructure. The direct effects of adding single elements and how they cause the changes are examine in this section. The last portion of this section examines studies that have looked at how different alloying elements changed the wear properties, in comparison to other alloys that do not contain the alloying elements or additional alloying elements.

2.5.1 Boron

Boron is sometimes added to produce more hard phases and increase wear resistance by adding boron to M_7C_3 carbides or through the formation of new borides such as $M_{23}B_6$, M_3B, M_2B, and M_3B_2. Boron can also be used to achieve finer carbides, because boron decreases the solubility of carbon in austenite. This increases the number of carbide nuclei that results in a larger number of finer carbides. TiB_2 has also been added to flux core wires to form TiC-Tib_2 particles that help increase the hardness and wear resistance. This also increases the number of carbide nuclei once again resulting in a larger number of finer carbides. Boron can also promote the formation of martensitic matrixes. [30, 38, 52, 64-67]

2.5.2 Carbon

Carbon is probably the most critical alloying component as it has a strong role in determining the carbide volume. Kotecki and Ogborn examined around 200 hard facing samples which ranged in microstructure and included martensitic deposits, buildup alloys, primary austenite with carbide, eutectic, austenitic manganese, near eutectic alloys, and primary carbides with eutectic. They found the most critical variable was carbon content. As the carbon content increased there was a trend for the wear resistance to increase [59]. Carbon increases the hardness and wear resistance but it also decreases the fracture toughness and increases brittleness [43].

One study looking at the effect of carbon content was carried out by Chang C et al. who examined the effect of increasing the carbon content in three CCOs. Specimen A had a low carbon content at 3.61 wt. % while specimen B had 4.47 wt. % and specimen C had 5.21 wt. % carbon. The weight loss of the alloys decreased with increasing carbon after undergoing erosion tests as shown in Figure 2-27. We can also see that the carbides are more numerous and refined as the carbon content increased in the micrographs in Figure 2-28[21].
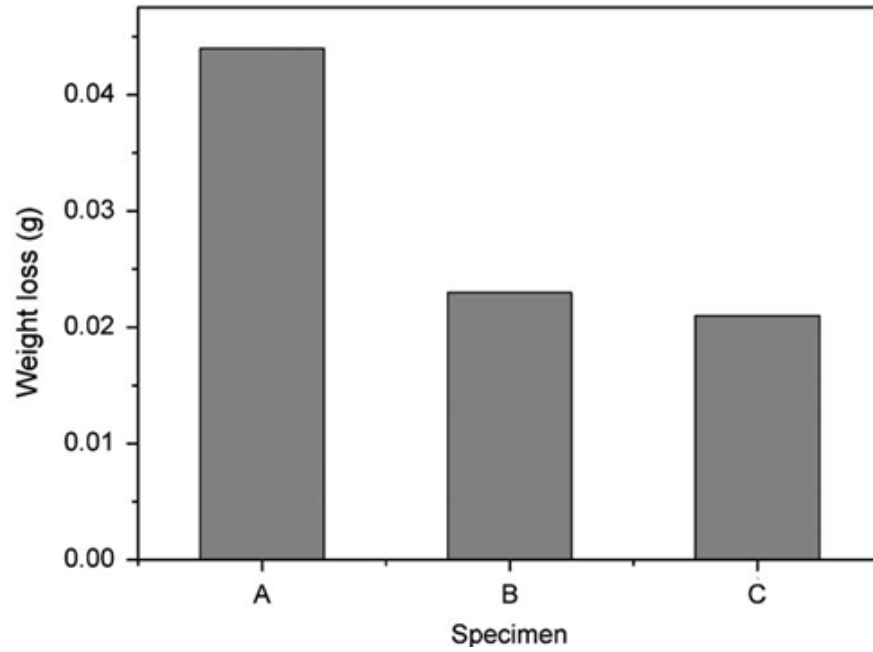
Figure 2-27: Weight loss comparison of alloys with varying carbon contents (a)3.61wt% C (b) 4.47 wt% C (c) 5.21 wt% C [21]
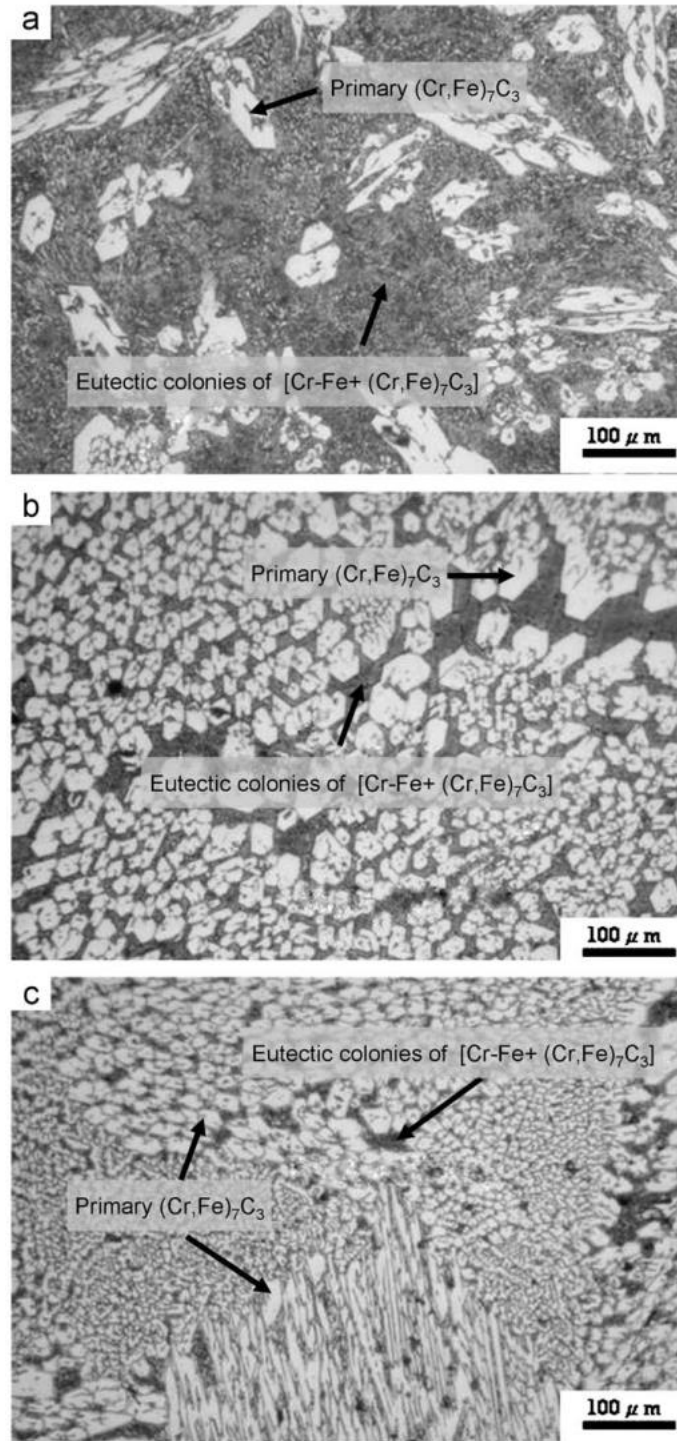
**Figure 2-28: Microstructure of Varying Carbon content
(a)3.61wt% C (b) 4.47 wt% C (c) 5.21 wt% C[21]**

The general trends were that the wear resistance, volume fraction and hardness all increased as the carbon content increased. These traits in the higher carbon content

overlays were accredited to the fact that the addition of graphite promoted the formation of hard M_7C_3 carbides.[21]

2.5.3 Ceria

A rare earth alloying addition that has been explored recently is ceria (Ce_2O_2). Ceria was added to a hypereutectic alloy in varying amounts of 0, 0.5, 1, 2, and 4 wt. %. As seen in Figure 2-29 they found that the ceria refined the primary carbide but after increasing above 2 wt.% the amount of refinement decreased from the 2 wt. % sample [48].
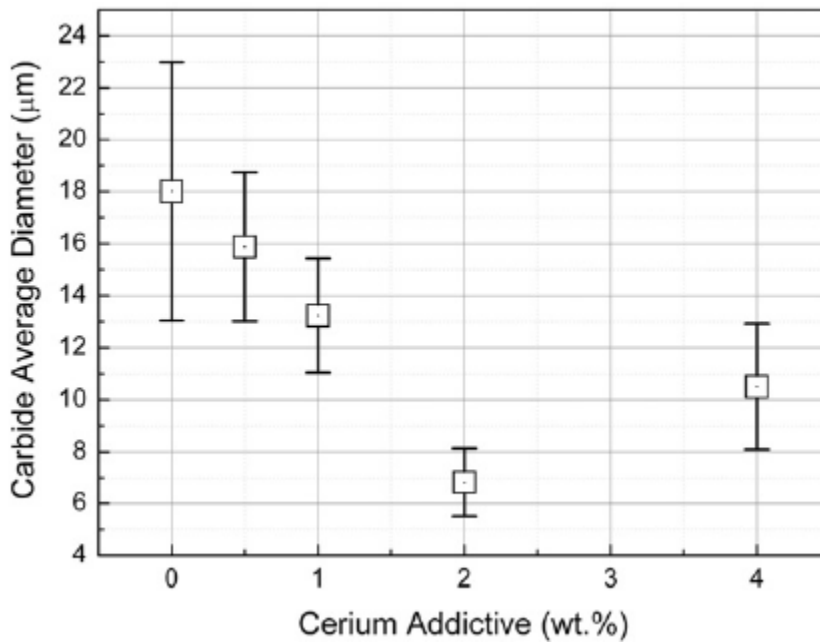
Figure 2-29: Effect of Ceria Addition[48]

Along with the most refinement belonging to the sample with 2 wt. % this sample also exhibited the best wear resistance of all the samples when undergoing testing on a belt abrasion tester. The cerium that was added in the ceria showed up in the microstructure as inclusions of Ce_2O_2S with none of the original Ce_2O_2 being observed in the microstructure after welding. The Ce_2O_2S inclusions were found distributed within the primary M_7C_3 carbides. Their findings also suggest that ceria plays an active role in deoxygenation and desulfurization of CCO's. Examining the lattice misfit between M_7C_3 and Ce_2O_2S they that found that Ce_2O_2S should also be middle effective at acting as a heterogeneous nuclei of the primary carbide, which could be the cause of the carbide refinement [48].

2.5.4   Copper

Copper is used to reduce the formation of pearlite and increase hardenability. It is normally limited to 1.5 wt% because of its limited solubility in austenite [30, 64]. Cu is found exclusively in the matrix and lowers the Ms temperature which often results in a decrease in the as cast hardness as it is increased [30].

2.5.5   Chromium

Chromium is added to white cast irons to form carbides, improve corrosion resistance and stabilize the structure at high temperatures [43].Chromium is also added when austenite structures are desired because high Cr/C ratios favor austenite microstructures [35]. Even though chromium is a ferrite former it helps to slow the rate of austenite decomposition which allows austenite to be retained under non-equilibrium cooling [35]. The Cr/C ratio also has a strong influence on the orientation and volume amount of primary carbides. Wang et al. found that lower Cr/C corresponded to higher volume fractions and a carbide orientation that is perpendicular to the overlay surface [39]. For a constant CV ratio an increase in chromium/carbon ratio increased the wear resistance. Increasing the Cr content in the matrix is also expected to increase the corrosion resistance [30]. Some researchers have also noted that chromium decreases the carbide size, however it is unclear if the cause in the increase in size was only linked to the increase in chromium amount or if it was the change in Fe/Cr mass ratios [43].

Chromium also greatly affects the eutectic carbide. Increasing the Cr amount leads to and increases in the volume fraction of the eutectic carbide volume and it also increased the chromium content in the carbides. This leads to an increase in the proportion of Cr to iron in the carbides which increase the carbide hardness [30].

2.5.6   Manganese

Manganese is added to increase hardenability and decrease pearlite formation. It lowers the Ms temperature which often results in a decrease in the as cast hardness. Manganese has been considered to be detrimental to wear resistance because it increases the stabilization of austenite which increases the austenite amounts in heat treated alloys and reduce SIT in as cast [30]. Manganese has been found to partition preferentially into carbides but is also found in the matrix [36, 64].

2.5.7 Molybdenum

Molybdenum is a carbide forming element and is found in the M_7C_3 carbides. Molybdenum has increased wear resistance through retardation of the formation of pearlite. Unlike Mn and Ni it does not lower the Ms start temperature. It has been found that greater than 1 pct. is needed to prevent pearlite but greater than 3% does not improve properties [30, 64]. Molybdenum additions are also added to help retain austenite. Molybdenum is especially effective because it reduces the rate of carbide precipitation. These carbides would remove Cr from the austenitic matrix which would raise the Ms temperature [35]. At high temperatures molybdenum decreases the wear rate it is believed that it could possibly be because Mo is prone to oxidation at temperatures above $500^{\circ}C$. Since Mo has a tendency to concentrate in the pro-eutectic carbides so if Mo is oxidizing it would have a large effect on the carbides.[68]

2.5.8 Tungsten

The addition of the tungsten to high chromium white cast iron leads to the formation of M_6C that crystallizes in a finely dispersed form as eutectic in the final stage of solidification. Tungsten increases the matrix hardness of white iron alloys; the wear resistance increases as tungsten increases [52].

2.5.9 Nickel

Nickel has very little solubility in in carbides and remains almost entirely in the matrix, it helps stabilize the austenite by the lowering Ms temperature and prevents the formation of pearlite [30, 35].

One study looked at replacing Fe with Ni resulted in a microstructure consisting of a matrix and M_7C_3 carbides precipitated as primary or eutectic carbides. They are very similar to conventional white irons with the largest difference being a mostly austenitic matrix. They also found that the Cr content in in the M_7C_3 carbides increase with increasing Ni content. One downside is that the amount of graphite forming will increase since Ni is a graphite forming element [69].

2.5.10 Niobium

Other exotic elements such as niobium, vanadium, and tungsten have also been added the white cast irons and CCOs. These have usually been added in an attempt to modify the eutectic carbide. Niobium forms primary niobium carbides that helped increase the bulk hardness and the wear resistance. Niobium does not increase the hardness of the primary

carbides. Niobium carbides also appear to cause finer rounder eutectic carbides which may increase the wear resistance because of the refinement of the matrix [30, 38].

2.5.11 Phosphorous

There may be a relationship between the wear rate and phosphorous amounts, Lopez et al. believe phosphorous may join with iron to form steadite which is hard and brittle which would decrease the wear resistance [68].

2.5.12 Silicon

Silicon can also increase wear resistance. However, the maximum silicon content is often limited to 1% as the silicon can increase the Ms temperature and can lead to an increased tendency for pearlite and graphite formation. Silicon has little solubility in carbide phases and therefore remains in the matrix. The effect of silicon on the eutectic microstructure has been conflicting [30, 35, 43]. Silicon has been found to lower carbon and chromium amounts in austenite by promoting the growth of carbides. It has also been found to promote undercooling in hypereutectic alloys to a complex regular microstructure which reduces toughness [64].Silicon has a large effect on decreasing the number of nucleation centers [19].

Laird and Powell found that in comparing hypoeutectic alloys with no silicon to ones with silicon that Si depresses the eutectic reaction temperature but that it has no effect on the volume of carbides. They found the primary dendrites had lower Cr and carbon amounts than the alloys without Si. They found that silicon does not have any effect on the partitioning of C and Cr between the austenitic matrix and the M_7C_3 carbides during eutectic solidification. Silicon inhibits the nucleation of M_7C_3 but does not affect its subsequent growth. Consequently it results in slightly larger eutectic carbides. Silicon raises the martensite start temperature which can increase the hardness of the alloys. They found the maximum microhardness was in samples with at 2.2 wt. % Si, but bulk hardness decreased at this amount probably due to an increase in the formation of pearlite.[50]

In hypoeutectic castings silicon can move the chemical composition of the alloy closer to the eutectic and hypereutectic region of the phase diagram. Because the solidification range is shorter as the composition moves closer to the eutectic line the microstructure becomes finer. Si also stabilizes the ferrite phase leading to less retained austenite. Silicon also leads to a decrease in the secondary dendrite arm spacing [70].

2.5.13 Titanium

TiC particles can act as substrates for heterogeneous nuclei's for primary M_7C_3 carbides. This leads to a significant refinement of the final size of the primary carbides [30, 71] Liu et al, found that the addition of TiB_2 changed the alloy significantly. The TiB_2 acted to increase the rate and number of nucleation of primary carbides. The increase in number of primary carbides generated increases the latent heat of fusion which inhibits the growth of primary carbides. This leads alloys that have TiB_2 additions to have a decrease in the average size of carbides while having an increase in the number of carbides. It has been found that the TiB_2 that was added in flux core wires generated TiC and TiB_2 in the hard facings. These additions significantly increased the Rockwell hardness and wear resistance of hard facings compared to a base sample that did not contain TiB_2 [65].

Huang et al examined the effect of Ti on high chromium cast irons and found primary M_7C_3 carbides are refined gradually and their morphology becomes more equiaxed as titanium amount increases but the changes slow after the addition of 0.95 wt. % of titanium. They found that when TiC contacts M_7C_3 type carbide tightly, orientation relationships develop which increase the possibility of TiC providing preferential heterogeneous substrate for M_7C_3 carbide nucleation. Further evidence of this may be that the TiC was often found to be in contact with or inside of carbides as seen in Figure 2-30.They also found that the lattice misfit between $(11\bar{1})_{TiC}$ and $(01\bar{1}0)_{M7C3}$ is 1.32% showing that TiC may be an effective substrate plane for M_7C_3 nucleation to improve the morphology and size of M_7C_3 carbides which would improve impact toughness [72].

Zhou et al. also found Ti can be added to help refine primary carbides but if too much is added the overall composition may become hypoeutectic. The MC carbide precipitates prior to the precipitation of M_7C_3. They determined the lattice misfit between $(110)_{TiC}$ and $(010)_{Cr7C3}$ is 9.257% is indicative that TiC acts as an heterogeneous nuclei of Cr_7C_3 which leads to a refining of the M_7C_3carbides. The primary MC phase precipitates out at 1843 $^{\circ}$K. The removal of carbon caused by the precipitation of MC carbides can cause a decrease in the mass fraction of M_7C_3 Carbides. [24]
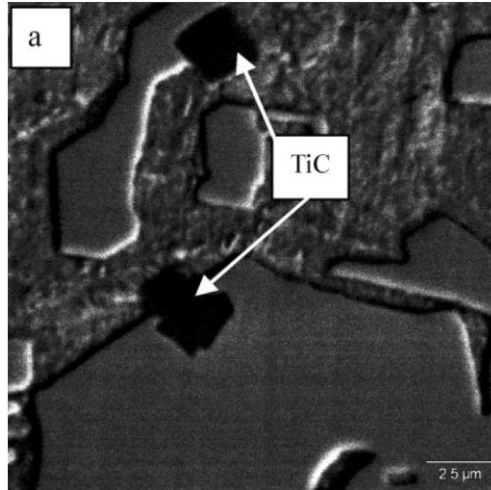
Figure 2-30: Examples of TiC in contact with primary M_7C_3 carbides[72]

2.5.14   Vanadium

Vanadium also increases the wear resistance by forming carbides and their refinement of the matrix. Formation of vanadium carbides and niobium carbides appear to cause finer and rounder eutectic carbides [30].

2.5.15   Comparisons of ternary Fe-Cr-C with alloyed variants

Many studies look at what the effect of certain elements are compared to other alloys that do not contain them or contain other additional alloying elements. These will be called comparison of ternary Fe-Cr-C with alloyed variants studies because the microstructures often have different microstructural characteristics that are caused by the additional elements and not just the traditional differences between hypoeutectic, eutectic, and hypereutectic alloys. An example of this is research by Leite and Marques looking at Fe-Cr-C alloys. They looked at a standard CCO alloy and then one with additions of just Nb and a third with additions of Nb and B. They found the microstructures of the Fe-Cr-C and Fe-Cr-Nb-B-C were hypereutectic while the alloy with just Nb additions was hypoeutectic. The wear resistance from greatest to least was Fe-Cr-Nb-B-C, Fe-Cr-Nb-C and Fe-Cr-C alloy. The presence of niobium and boron in Fe-Cr-Nb-B-C alloy contributed to the improved wear resistance of it over the Fe-Cr-C alloy. The formation of Nb carbonates in the hypoeutectic alloy is thought to be why the hypoeutectic alloy uncharacteristically outperformed a hypereutectic alloy [73].

Another study comparing a number of different samples was carried out by Menon et al. They examined four different wires commonly used for hard facing. The designation for

42

the wires was 2C-23Cr, 5C-25Cr, 5C-25Cr-M, and 5C-25Cr-CLX(5C-25Cr-Nb-V). The microstructures of these alloys were hypoeutectic, hypereutectic, hypereutectic with the addition of alloying elements to refine the microstructure, and hypereutectic with complex carbides of Nb and V respectively. The hardness values are lowest for the hypoeutectic alloy and highest for the complex carbide deposit as shown in Table 2-3 [67].

Table 2-3: Iron Based Cr-C overlay alloys showing resulting microstructure and hardness values [67]

Designation/Nominal Composition	Typical Hardness (HRC)	Microstructure
2C-23Cr	38	Austenite-Eutectic Carbide
5C-25Cr	47	Austenite-Primary Chromium Carbide
Microalloyed, 5C-25Cr-M	62	Austenite-Primary Chromium Carbide
Modified Complex, 5C-25Cr-CLX	65	Austenite-Primary Chromium Carbide-Complex Nb, V Carbides

Table 2-3 shows the hardness of the alloys is increased with the addition of alloying elements such as Mn, V, and Nb that form secondary carbides. The 2C-23Cr wire has very good ductility but poor abrasion resistance. The 5C-25Cr is the most commonly used wire because of its ability to be used for multipass welding and suitability for low to moderate wear purposes. The 5C-25Cr-M alloy is used in critical applications where a combination of wear and toughness is needed such as cladding of pipe for slurry transport in the oil sands. For the more severe abrasion applications the 5C-25Cr-CLX wire is used. The general trend of all these different wires is that alloying elements such as C, Mn, Nb, and V can be used to increase the hardness and wear resistance of the overlays [67].

3.   Performance of CCOs

This section examines some of the important properties of CCOs. The most general one is most likely hardness because in order to have good wear resistance the material being worn needs to have microstructural constituents harder than the wear particles. The hardness measurements can be misleading so the most accurate way to measure their wear properties is through wear testing. The difficulties and subtleties of using this as a

measure are discussed. The last portions of this section examine studies that have looked at the wear resistance, corrosion resistance, and toughness of these alloys and highlights what can be done to improve these properties.

3.1. Hardness

Hardness is often one of the main measures used to quantify the quality of wear resistant overlays. This is because the high hardness of carbides is a main reason for the wear resistance of overlays. Therefore as a generality it is thought that the harder the carbide and overlay are the better the wear resistance is. This is because this trend of high hardness correlating to higher wear resistance is often seen when examining overlays of like materials systems[21]. But, Kotecki and Ogborn note that hardness values must be taken carefully as 50 to 55 HRc can be obtained from low-alloy marteniste, work hardened austenitic manganese and near eutectic austenite carbide, but in low stress abrasion near eutectic alloys outperform the other two by a large margin.[59] Similar results showing coatings with similar hardnesses but significantly different wear rates were noted by Liete et al.[73]. Other examples when higher hardness may not increase wear resistance is carbides that experience brittle chipping. Also in conditions where the hardness of the carbides is significantly lower than the abrasive particles the actual hardness of the carbides are much less important [15].

The relationship between the hardness of the carbides and the wear particles are of upmost importance. Table 3-1 shows hardness of different microstructural constituents and carbides and some of the common abrasive media used for testing and that the overlays come into contact with in service. In CCOs the wear resistance comes from the M_7C_3 type carbide because its hardness is higher than that of quartz and garnet which are common particles it encounters in the minerals industry [30]. For example oil sands are typically composed of 80-95% quartz that is generally less than 150um in size with a semi angular shape.[13]

Table 3-1: Hardness of abrasive materials relative to hardness of microstructural constituents of alloy white irons [30]

Abrasive material	Hardness Knoop	Vickers	Microstructural constituent
Silicon carbide	2585	2500–2600	...
	2660	2800	Vanadium carbide
Corundum (Al$_2$O$_3$)	2020	1800–2000	...
	1735	1200–1800	M$_7$C$_3$-type carbide
	...	1060–1240	M$_3$C-type carbide
Garnet	1360	...	...
Quartz (silica)	840	900–1280	...
	...	770–800	High carbon martensite
	...	350–400	Austenite

Figure 3-1 and Table 3-2 show the typical hardenss values of other types of carbides. Of particular intrest is the note at the bottom of Table 3-2 Jiyang and Jincheng note that the dissolution of Fe into Cr$_7$C$_3$ to form M$_7$C$_3$ can lower the hardness from 2,100 HV to a range of 1500 to 1800 HV
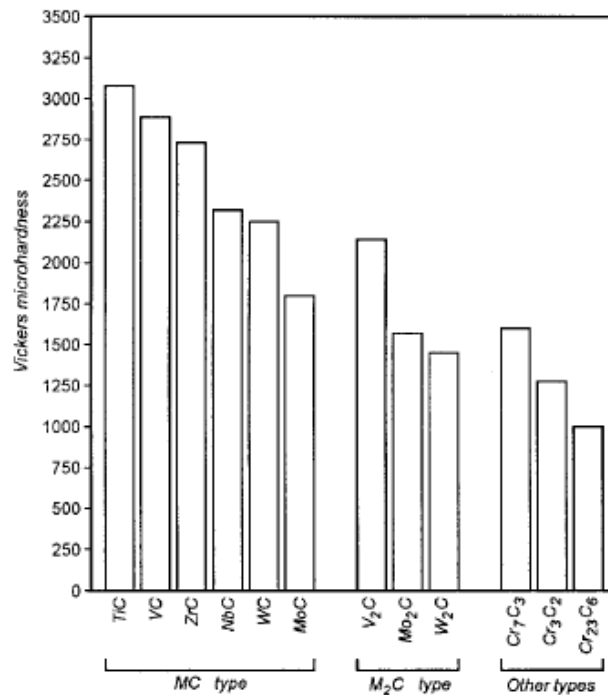
Figure 3-1: Average hardness of carbides [15]

45

Table 3-2: Characteristic Parameters of Carbides [43]

Carbide	Crystal type	Lattice constant nm	Melting point °C	Hardness HV
Fe_3C	Rhombic	$a = 0.4514$ $b = 0.5087$ $c = 0.6728$	1,650	860
Cr_7C_3	Hexagonal	$a = 0.688$ $b = 0.454$	1,780 (decompose)	2,100
$Cr_{23}C_6$	Complex cubic	$a = 1.064$	1,520 (decompose)	1,650
Mo_2C	Hexagonal	$a = 0.30$ $c/a = 0.158$	2,600 (decompose)	1,500
W_2C	Hexagonal	$a = 0.298$ $c/a = 0.1578$	2,750	2,060 HM
WC	bcc	$a = 0.2901$	2,867	2,400
VC	fcc	$a = 0.4130$	2,830	2,800
NbC	fcc	$a = 0.4458$	3,500	2,400
TiC	fcc	$a = 0.432$	3,150	3,200
ZrC	fcc	$a = 0.4687$	3,530	2,890

Note: If a carbide dissolves another element, its hardness will change, for example if it dissolves Fe:
$(Fe,Cr)_3C$: 840–1,100 HV; $(Fe,Cr)_7C_3$: 1,500–1,800 HV; $(Fe,Cr)_{23}C_6$: 1,140–1,500 HV

While harder carbides are often beneficial to wear resistance it is important to keep in mind that the key to the best possible wear resistance is often a good combination of hard carbides and a tough matrix [38].

3.2.   Wear performance

The wear resistance of CCO's is probably the most critical property of the overlays. This can be very difficult to measure because wear encompasses so many different aspects.

Figure 3-2 illustrates the amount of corrosive, abrasive, impact and metal to metal wear that occurs in industry.
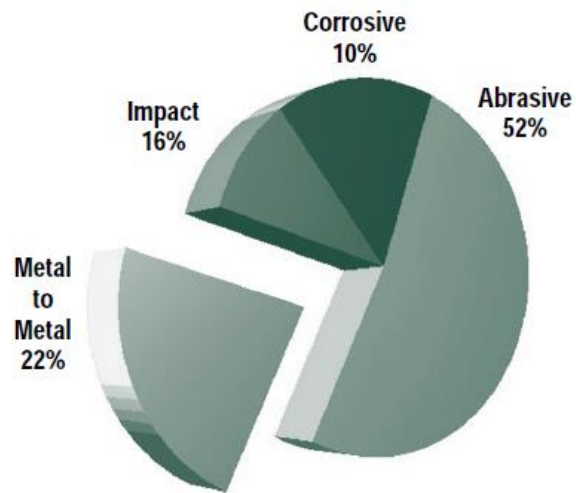
Figure 3-2: Illustration of the ratio of different wear categories in industry [74]

Figure 3-3 and Figure 3-4 show that CCO's tend to be used for abrasive wear, impact, corrosion indentation and gouging [11, 74]. The largest amount of CCO's are used in circumstances where they are undergoing abrasion. This simplifies the type of wear we want to examine when discussing CCO's. However, abrasive wear can still be broken down into smaller categories. According to Dumovic abrasive wear can be classified into gouging abrasion, high stress grinding abrasion, low stress scratching abrasion (or erosion) [74].
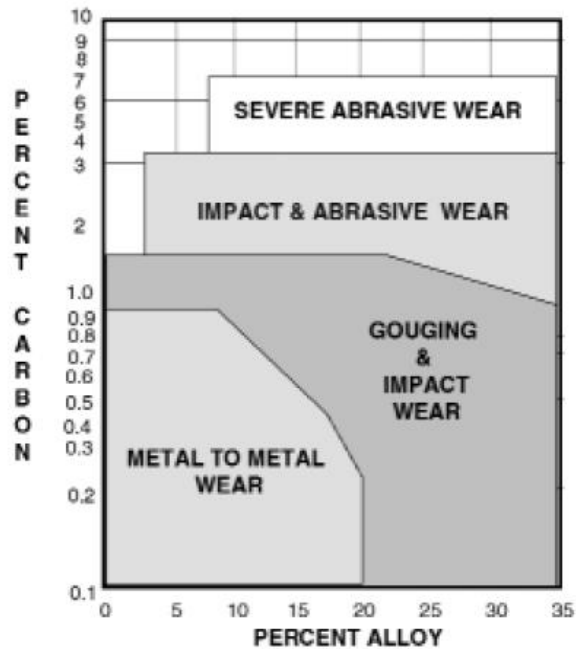
Figure 3-3: Illustration showing correlation of carbon and alloy percent and type of wear material is commonly used for [74]

Applications	Conditions	Materials
Roadways and material collection	Abrasive wear	High-grade steel
Break up mined material	High-stress abrasion, indentation, gouging	CrC overlays, cast iron
Separate and remove big rocks	Corrosion, erosion–corrosion	CrC overlays
Transportation of tailings	Corrosion, erosion–corrosion	Hardened carbon steel, CWIs
Pumping of slurry and tailings	Low-stress abrasion, erosion–corrosion	CWIs, CrC
Transportation of slurry and tailings	Corrosion, erosion–corrosion	Hardened carbon steel, CWIs

Figure 3-4: Examples of common wear in oil sands and wear resistant products used[11]

Because abrasion is the most common type of wear CCO's undergo a common test to determine the wear properties of chromium carbide overlays is the ASTM G65 test [30]. An effort has been made to explicitly state in this thesis when a statement concerning wear properties was not found through ASTM G65 testing.

The actual wear rates of overlays are dependent on a number of factors including carbide type, free mean path of the matrix between carbides, morphology of carbides, orientation, carbide volume fraction (CVF), carbide size and chemistry. Some work has shown that the abrasion resistance is governed mainly by volume fraction (VF) and distribution of carbides within the matrix while the matrix hardness is only of secondary importance

48

[75]. Wang on the other hand believes that the key to the best possible wear resistance is a good combination of hard carbides and a tough matrix [38].

The weight percent of carbon also plays a huge role in the resulting wear resistance and hardness [4, 8, 12, 48]. An increase in the surface fraction of primary carbides usually leads to an increased wear resistance when the abrasives are softer than the target material, however in some circumstances this can be reversed [8, 30, 76]. This is because the hard primary carbides normally provide protection to matrix from the indentation, grooving and cutting caused by the abrasive particles. Chang et al. found this relationship to be nonlinear meaning the wear resistance increases quickly as the surface fraction increases [8]. Using pin on disk wear testing Kagawa also found that the wear resistance increased as the volume fraction increased but found it to be linearly correlated for a number of bulk $(Fe,Cr)_7C_3$ alloys [77]. When the interparticle spacing is small compared to the abrasive particle size the wear resistance can increase. Chang et al. has shown that volume losses decrease linearly as (hardness/mean) free path increases [8]. Liu et al found that the hardness and wear resistance of CCO's increases by obtaining a regular hexagonal distribution rather than random distribution of M_7C_3 carbide when testing using a plastic core-rubber wheel abrasion test.[55] Similarly Dogan noted that previous research has shown that high Cr white iron castings have better wear resistance when the carbides are oriented perpendicular to the wear surface [9].

When comparing a large number of different types of hard facing Fe-Cr-C alloys Kotecki and Ogborn found that carbon was the most important indicator of wear resistance with other alloying elements playing only secondary importance. They also showed that macro hardness does not correlate to abrasion resistance; however quantity and hardness of micro constituents did correlate to abrasion resistance [59]. The addition of niobium and vanadium to form harder secondary carbide types can also improve the abrasion resistance in CCOs [30].

The abrasion resistance of high chromium irons can has been shown to be twenty to twenty five times better than low carbon steels when the wear particles are softer than the carbides as with alumina and quartz particles, but when the wear particles are harder the ranking changes [76]. For example the wear resistance was 20, 7 and twice as much for chromium white irons when eroded with cement clinker, blast furnace sinter and silica respectively. This shows that for low stress abrasion the wear resistance of CCOs greatly

49

outperforms low alloy steels, but under high stress abrasion the wear resistance may not increase nearly as much [17]. In comparison to other wear resistant materials CCOs have been found to have 2.83 times higher abrasion resistance [78]. Specifications for wear rates of overlays used in oil sand applications generally call for WC overlays to have at 4 times better wear resistance than CCOs.

3.2.1   Wear Testing G65 Apparatus

Since abrasion is the most common type of wear CCO's undergo the most common test to determine the wear properties of chromium carbide overlays is the ASTM G65 test [30]. The G65 test is a dry sand-rubber abrasion test in which the sample is held against a rubber wheel that is rotated as an abrasive is introduced between the test piece and the rotating wheel [79]. A schematic of a G65 test setup is shown in Figure 3-5. There are a number of prescribed procedures that are used based on the wear resistance of the type of material being tested. For highly wear resistant materials such as CCO's, procedure A is the most commonly used because it employs the highest force and largest number of wheel rotations. The abrasive used is quartz sand as specified by the ASTM standard. The test parameters of the different procedures are given in Table 3-3.

Table 3-3: G65 Test parameters[79]

Specified Procedure	Force Against Specimen,[B] N (lb)	Wheel Revolutions	Lineal Abrasion[A] m	(ft)
A	130 (30)	6000	4309	(14 138)
B	130 (30)	2000	1436	(4 711)
C	130 (30)	100	71.8	(236)
D	45 (10.1)	6000	4309	(14 138)
E	130 (30)	1000	718	(2 360)
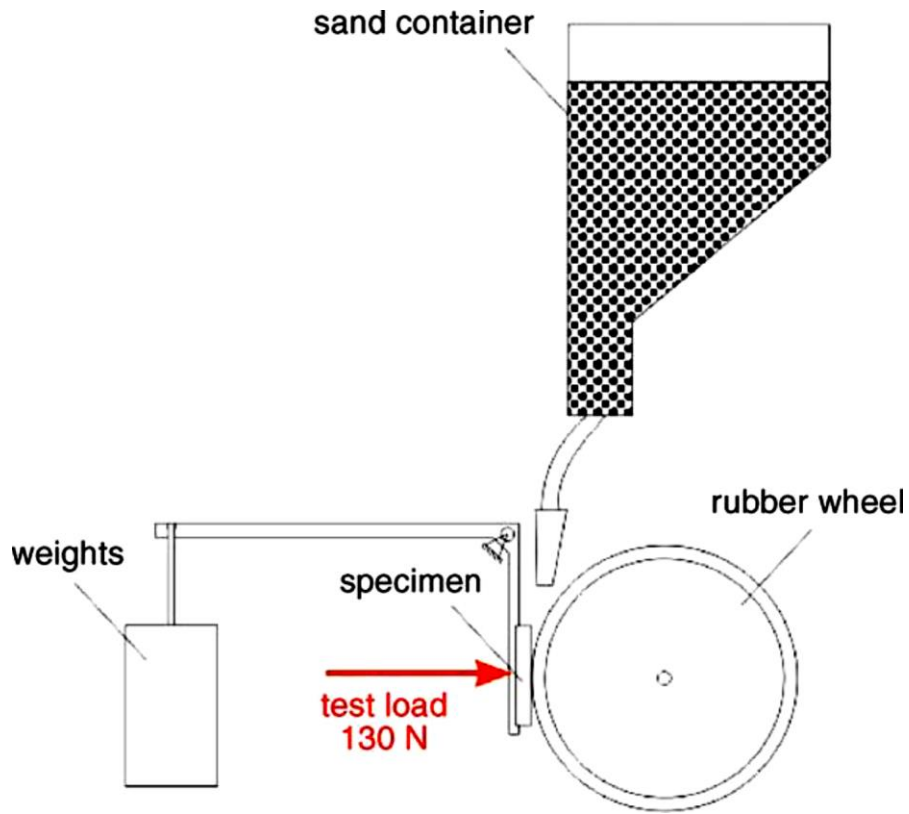
Figure 3-5: G65 wear apparatus schematic[78]

The specimen that is tested must be 1x3 inches and between .12 and .5 inches thick with a surface finish of 0.8um or less [79]. After the test has been carried out the original specimen will have lost a portion of medal where the wheel, sample, and sand come in contact with each other as illustrated in Figure 3-6.
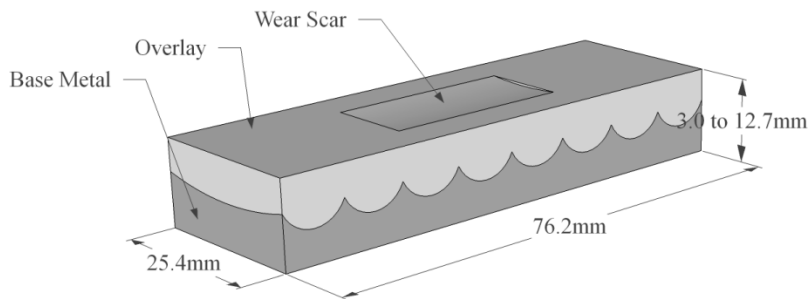
Figure 3-6: G65 specimen schematic post testing

Because of issues with dilution in the CCO's it is common for end users to require producers to provide the results of G65 tests performed at the surface and at 75% through

the overlay. The hardness is also often measured between the top and bottom of the overlay with average hardness requirements.

3.3. Previous Studies on the Wear of CCOs

The previous section dealt general rules and guidelines for improving wear resistance, this section will deal with the effect of changing parameters on wear resistance and actual values of wear resistance or mass loss. The process of material removal will also be examined. Previous work has shown how there can be a huge variance in the wear resistance based on the different microstructures and compositions of CCOs. However, there is a trend for decreased wear resistance going from hypereutectic, eutectic to hypoeutectic microstructures [59]. The volume loss for hypereutectic overlays tend to range between 15 and 68 mm^3 [11-13, 38, 48, 55, 59, 67, 78, 80, 81]. Koeteki and Ogborn found that wear loss range between 84.6 and 205 mm^3 for hypoeutectic overlays and 34.6 and 171mm^3 for near eutectic overlays. [59]. A large part of this increased wear resistance going from hypoeutectic, eutectic to hypereutectic microstructures can be attributed to the increase in the amount of hard carbides.

Unlike most other research Sabet et al. found that the wear resistance of a hypoeutectic alloy was greater than that of both the eutectic and hypoeutectic alloy. One reason given for this is that it gains maximum hardness after the wear test. They believe that it is related to the characteristic of the hard phases and the ability of the matrix to undergo work hardening. They found that some of the austenite in the samples transformed to martensite. The highest amount transformed was in the hypoeutectic alloy followed by eutectic and hypereutectic with the least transformed. This transformation led the hardness that was originally 701, 745 and 809 HV to become 857, 816, and 813 HV for hypoeutectic, eutectic, and hypereutectic respectively after wear testing. The reason for this difference in trends of wear resistance between microstructural types compared to the majority of other research may be that their samples are relatively low in alloying Si and Mn alloying elements which lead the A to M transformation to have a significant role on wear resistance. It should be noted that the lowest wear loss of the hypoeutectic alloy is still much higher than the traditional wear rates of hypereutectic alloys. This leads to the belief that there is something significantly different about the microstructure wear behaviour in these samples that have changed their wear characteristics [14].

The relationship between the matrix and the primary carbides on wear has not been clearly shown. There are two different trends of thinking, one the primary carbides protect the matrix from being worn out. The second is that the primary carbides are worn away only after sufficient matrix has been removed so that the matrix is no longer providing mechanical support. This means that the role of the matrix when the primary carbides are protecting the matrix is to provide mechanical support to the carbides. The second theory suggests a much more complex relationship, where if the matrix can be preferentially removed the carbides become unsupported which can lead to a susceptibility of spalling and fracture of the carbides. In this mode the matrix is the critical step in controlling the wear resistance because the carbides will wear at a rate proportional to how quickly they are no longer supported by the matrix. It has been suggested that for hard abrasives austenitic matrix is preferred while for softer abrasives martensitic matrix performs best. It is also thought that conditions that promote strain induced transformation of austenite to martensite also increase the wear resistance. A stronger interface and similar lattice parameters between austenite and carbides are also thought to improve the abrasion resistance [30]. It should also be noted that the wear mechanisms may change based on the type of wear that the overlay experiences which may change the relationship between the matrix and the primary carbides.

Lin et al. found that if the hardness of the reinforcement particle is lower than that of the abrasive particle then the reinforcement particles tend to be extracted from the matrix. While if the abrasive particle is not as hard as the reinforcement particles the matrix is damaged preferentially and then the reinforcement particles undergo brittle fracture. For samples that had a hypereutectic microstructure of primary M_7C_3 carbides surrounded by a eutectic matrix they found the wear mechanisms was the removal of the matrix followed by the reinforcement particle undergoing brittle fracture. This was found using a dry sand-rubber wheel abrasion test[1] .

Wang et al. examined why carbide orientation plays a role in wear resistance using a shot blasting machine to test impact-abrasive conditions. They found that M_7C_3 carbides paralleling the shots flow direction possessed higher hardness and fracture toughness than that of ones perpendicular to flow direction. They note that literature states that when the long axis is perpendicular to the wear surface the wear resistance is high, while others say that the orientation has no significant role in wear resistance. They explain this as being the large difference in experimental set ups used to determine wear resistance. In the

samples where the carbides were perpendicular to the wear surface the wear in the matrix was found to be through delamination wear mode and distinct grooves show plasticity dominates the wear mode. The carbides damages however are caused by subsurface cracks due to plastic shearing on the sliding surface. The subsurface cracks propagate and eventually break open to give particle like wear debris as illustrated in Figure 3-7. Under impact abrasion wear cracks occur because of tensile stresses exceeding the strength limit of the carbide. Because the hardness and elastic modulus is higher for carbides are that are parallel to the impact surface this orientation of carbides has a higher wear resistance compared to when the impact is perpendicular to the long axis of carbides [56].
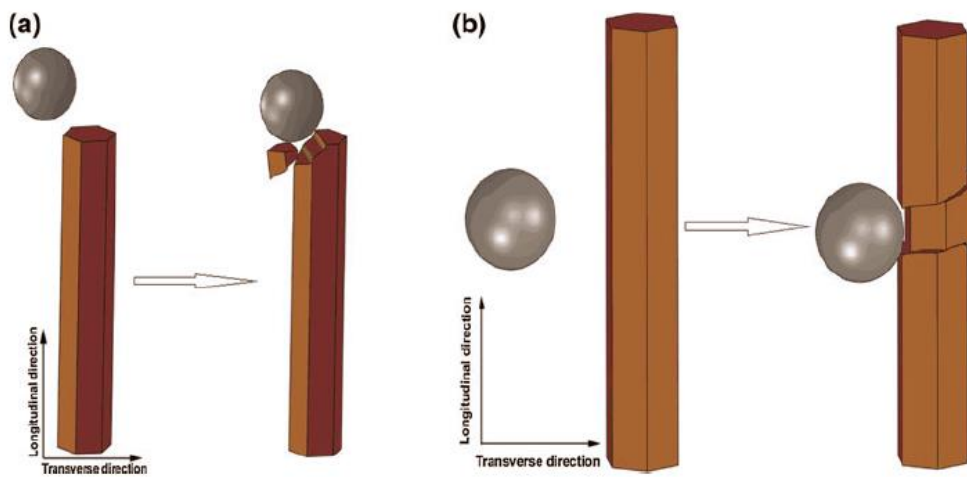
Figure 3-7: Schematic diagram illustrating how cracks form: (a) n Impact direction parallel to the long axis of the carbides and (b) Impact direction perpendicular to the long axis of the carbides[56]

In ductile materials the peak erosion occurs at a 20-30° impingement angle while the maximum erosion rate normally occurs at a normal impact angle for brittle materials. It has been found the erosion resistance correlation to CVF becomes less as strong as the severity of the erosion increases [76]. Erosion rates also show very different trends based on erodent particle hardness and erosion conditions. Under mild conditions erosion rates decrease with increasing CVF. With silica particles erosion rate increased with increasing CVF under severe conditions and at normal impingement during moderately severe conditions. Using silica At 30^0 angle during moderate erosion conditions an increase in CVF did improve erosion resistance. When the erosive particle was alumina a large number of carbides proved detrimental during moderately severe conditions. The erosion rates can be explained based on the actual material wear. In the case of mild erosion

conditions carbides protrude from the surface while under severe conditions the carbides appear depressed. The alumina particles plastically indent and cause lateral fracture of carbides. Gross fracture of carbides when impacted with silica particles occurs at normal impact angles while at lower angles small scale chipping and micro fracture occur [76].

Maldonado-Ruiz et al examined the microstructural of high chromium and high carbon cast irons. The wear testing was carried out by impacting the wear surface with reduced iron pellets at 823 $^\circ$K. The size distributions of the primary M_7C_3 carbides were found to influence the wear but they found no correlation between the hardness of the different constituents and the wear rate. They did find that samples with higher amounts of molybdenum had higher wear rates. It was also found that the samples with the highest wear rate had higher proportions of large carbides. They a have also suggested that there may be a relationship between the wear rate and phosphorous amounts, they believe phosphorous may be join with iron to form steadite which is a hard brittle structure that would decrease the wear resistance. They are not sure why molybdenum decreases the wear rate but they believe it could possibly be because Mo is prone to oxidation at temperters above 723 $^\circ$K. Mo has a tendency to concentrate in the pro-eutectic carbides so if Mo is oxidizing it would have a large effect on the carbides.[68]

Flores et al. looked at the erosion corrosion of plasma transferred arc welded Fe-Cr-C and WC-Fe-Cr-C overlays using an impinging jet apparatus. The MMC of this alloy (WC-Fe-Cr-C) was made using the same powder Fe-Cr-C with an addition of 65wt% of WC to the powder. The addition of WC promoted the formation of WC rich intermetallic phases, which increased the micro hardness and increased the erosion corrosion performance. The type of erosion that occurred was dependent on the microstructure. The erosion of The Fe-Cr-C matrix was micro cutting and micro ploughing degradation at 293° K. The erosion of the Fe-Cr-C-MMC was through removal of the metal matrix caused by the erosive effects of the sand through a process where the matrix goes through a micro crack formation, propagation and then brittle fracture caused by the impact of the sand particles. [12]

3.3.1   Effect of matrix on the abrasive wear performance

The effect of the matrix particularly between martensite and austenite becomes very complicated as the abrasive material appears to play a critical role as seen in Figure 3-8. The hardness of the abrasive material plays a role along with other factors such as the

angularity of the particles, the grit size and load. Under low stress high hardness applications as long as the carbides do not become unsupported by the matrix the wear rate is largely controlled by the wear rate of the carbides. Under high stress abrasion and low hardness abrasives an increase in the carbide volume increases wear resistance, but with harder abrasive particle the opposite effect can occur. It is believed that this phenomenon is related to the harder particles hitting the carbides causing spalling, pitting, or fracturing based on the type of wear test. Anything that increases the depth of cut (ie. harder abrasives, higher loads, angular abrasives) are thought to more likely cause carbide fracture therefore increasing wear rate. The orientation of the carbide is also important; perpendicular to the wear surface is thought to be the best. This is thought to be because this orientation gives greater support to the carbides. The carbide faces have also been reported as being harder than the longitudinal faces. Contrary to what was previously said however for high stress applications Dogan found carbides parallel to the wear surface were better [30].
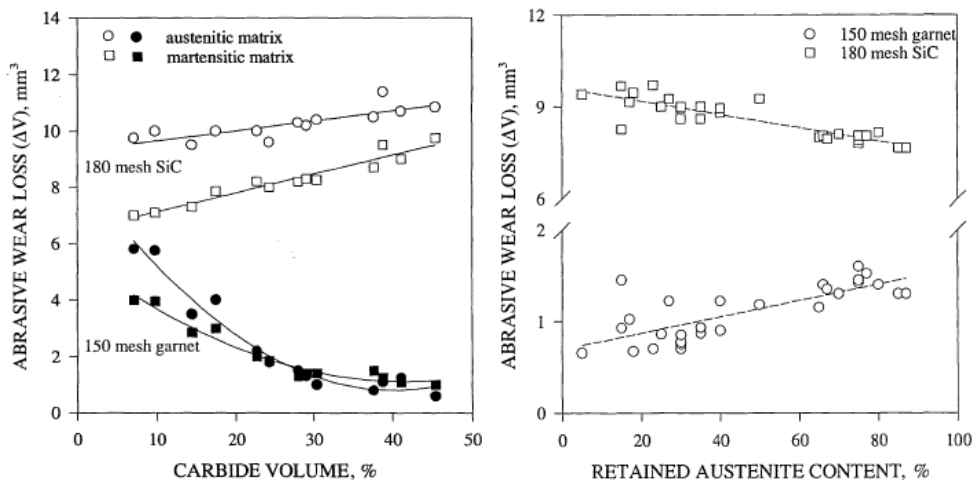
Figure 3-8: Graphs showing effect of microstructure and abrasive particle on wear [30]

We can see a very complicated relationship in Figure 3-8 showing how wear resistance trends can be opposite in the case of different wear particles. Under low stress conditions with soft particles it has been found that increasing carbide volume in hypoeutectic alloys improves abrasion resistance this is because the wear occurs because the particles wear out the softer austenite regions until the carbide (including eutectic) are left unsupported and then break. It has even been found in hypereutectic alloys that increasing CV actually decreases wear resistance. In this case the wear was found to be the spalling of carbides caused by the carbides becoming unsupported by matrix [30].

56

With low stress and harder particles such as SiC and Alumina both the matrix and the carbides are worn down by the particles. The carbides wear out slower because of their higher hardness in these cases the matrix structure has low effect on changing wear resistance. With low stress and harder particles the wear resistance improves as CV increases for hypoeutectic and hypereutectic alloys. Under high stress abrasion the effect of increasing the CV is once again dependent on the type of abrasive. If an abrasive medium such as garnet or silica that are softer than M_7C_3 carbides the wear resistance increases as CV increases. With harder abrasives such as alumina and SiC there is often little improvement gained by increasing CV and in some cases the wear resistance can actually decrease [30].

3.3.2   Corrosion Resistance of CCOs

The corrosion resistance of the chromium carbide overlays is often secondary because the life spans of the overlays are often much shorter than the time frame that corrosion would need to cause failure. However, in certain applications such as hydro transport components in the oil sands it can be very important. Neville et al. studied three alloys with varying chromium and carbon amounts. The results of their studies show that there are two main factors that affect the corrosion rate. They are the primary carbide area fraction, the amount of chromium and other alloying elements in the matrix. The corrosion resistance was found to be strongly dependent on the ratio of chromium content in the M_7C_3 carbide to that in the matrix. It has been noted that in order to achieve corrosion resistance in white cast irons at least 12wt% Cr is needed in the matrix. This amount of Cr means a protective coating of Cr_2O_3 can form on the surface to protect the material from its environment. It was found that corrosion attack is initiated around the primary carbides. This is because of the depleted region around the carbides that is low in Cr [23].

 In chromium carbide overlays corrosion can occur through galvanic coupling between M_7C_3 carbides and the austenitic matrix surrounding the chromium carbides. A schematic of this galvanic cell is shown in Figure 3-9 [5].
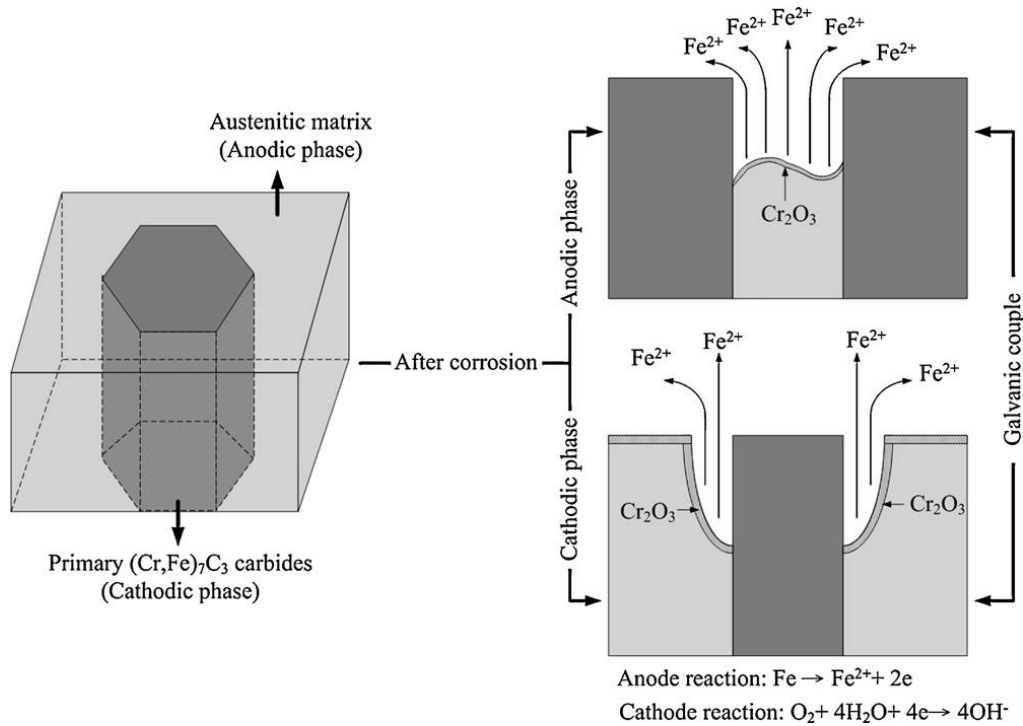
Figure 3-9: Illustration of galvanic corrosion in Hypereutectic Fe-Cr-C Cladding[5]

Chang, Chia-Ming et al. examined the influence of carbon content on the corrosion characteristic of the hypereutectic Fe-Cr-C claddings. The primary carbide surface fraction in the samples varied from 33.81% to 86.14%, as the carbon content increased from 3.73 to 4.85 wt. %. The corrosion resistance of the alloy with 4.85 wt. % C was roughly 20X higher than the alloy only containing 3.73 wt. % C. They suggested that the reason for the change in corrosion resistance is that the dense distribution of primary carbides retards the austenitic matrix from selective corrosion.[5] Menon et al. examined three hypereutectic alloys and one hypoeutectic alloy and found that the wire with the hypoeutectic microstructure had the best corrosion resistance. In this case the cause of the difference in the corrosion resistance was presumable from the fact that in the hypereutectic alloys a large amount of Cr comes out of the matrix in order to form Cr_7C_3. These carbide deposits caused the wt. % of Cr in the matrix to drop below 12% which means no passive layer is formed to provide corrosion resistance. It is the depletion of chromium in the matrix in the higher carbon content wire that leads to the decrease in the corrosion resistance [67].

Jones and Llewellyn examined the erosion corrosion of a number of different alloys using a slurry pot erosion-corrosion tester. They measured values for corrosion and erosion

separately and then both at the same time. They examined three white irons; a hypereutectic alloy, a near eutectic, and a high chrome low carbon alloy with a microstructure of carbides in a duplex austenite/ferrite SS matrix. They found that the hypereutectic alloy had the highest E-C rate of the three as shown in Figure 3-10. This is partially due to the fact the corrosion only value was highest and it had a high synergistic effect with the erosion. The synergistic effect is the cumulating of how much the erosion is enhanced by corrosion and vice versa. Of the other two alloys they had very similar total E-C values with differences being the near eutectic alloy had better erosion resistance but the low carbon high Cr had higher corrosion resistance.[82]
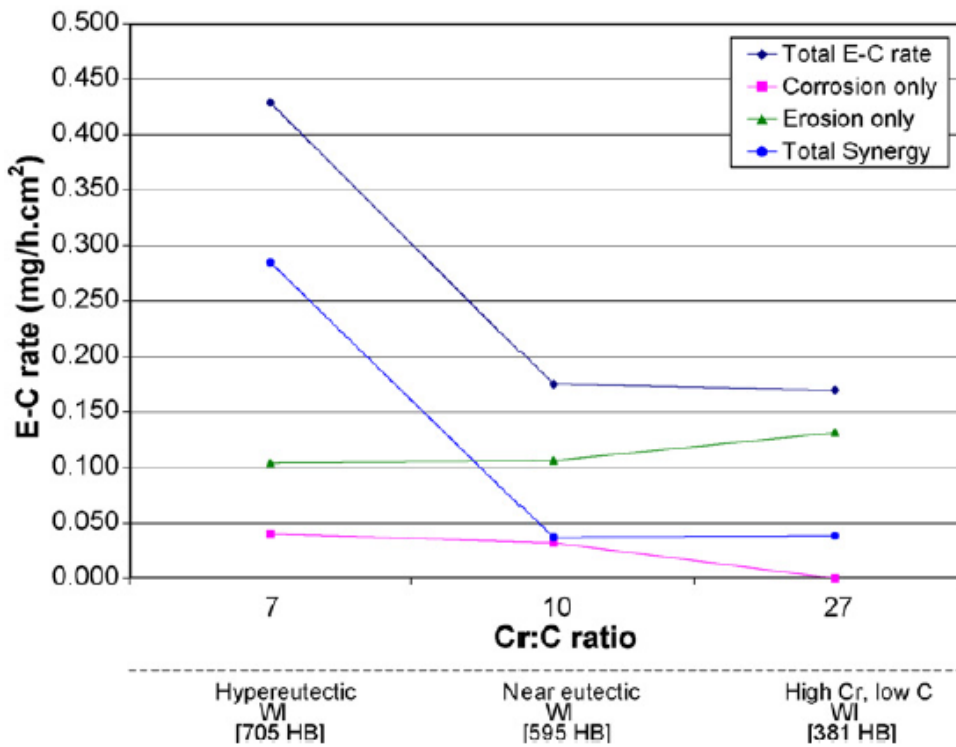
Figure 3-10: Erosion corrosion testing results [82]

Another alloying element that can affect the corrosion properties of Fe-Cr-C overlays is silicon. Three different hypoeutectic compositions of overlays were deposited with the compositions of varying in silicon amounts The silicon amounts were 0, 6 and 10 wt. %. The corrosion rate was 2.9, 1.89, and 7.61 (mpy) respectively. Going from 0wt. % Si to 6wt. % silicon the corrosion resistance increased, but a further increase in the silicon concentration to 10% produced a significantly higher corrosion rate than either of the other two overlays. This is thought to be because the high amounts of Si caused Fe_3Si to

59

form which led to an increase of Cr in austenite which consequently caused a decrease in the amount of M_7C_3 carbides which increases the corrosion rate [4].

3.3.3 Toughness of CCOs

Toughness is another important mechanical measure of CCOs. Often times the greatest difficulty in choosing a wear resistant material that is most suitable for a specific application, is controlling the relationship between good wear resistance and good impact toughness [35]. Fracture occurs by the ductile tearing of matrix through the carbides or the interface between the carbides and matrix [19]. It has been observed that the proportion of eutectic carbides on fractured surface is high [30].The fracture toughness can be hard to control but a few ways to increase fracture toughness are to refine the eutectic carbides or decrease their continuity [35]. Having randomly oriented carbide fibers increases the toughness of the overlays compared to carbides that are lined up perpendicular to each other [32]. Strain induced transformation can also increase toughness. Increasing the carbide volume has been found to decrease toughness. Lower superheats which produced finer dendrites and carbides increase the toughness. Having an austenitic matrix is also better than martensitic for toughness. An increase in the amount of austenite in the matrix has been found to increase the toughness. It is believed that higher energy levels for crack initiation and slower propagation in austenite lead to these relationships. However, some studies have shown that austenite is detrimental to impact resistance under repeated impacts. [30]

Lee et al examined the effect of matrix on the fracture toughness of high chromium white cast irons hardfacing alloys. They accomplished this by changing the matrix type by controlling the Mn/Si ratio to change between pearlite, austenite, and a mixture of pearlite and austenite. They kept the total carbide volume fraction constant. They found the cracks tended to initiate at the large primary carbides and were blocked at the austenite in the matrix which suggested that the fracture toughness may be controlled by the amount of austenite in the matrix.[63]

Pearce believes that fracture toughness data can be used to indicate the severity of pre-existing defects such as shrinkage or hot tears but may not be give a true indication of the performance of white irons under impact fatigue conditions [35]. Critics have argued that using Charpy impact testing to study the fracture mechanics of white irons is inappropriate because Charpy tests measure resistance to crack propagation; on the

contrary it is thought that the fracture resistance of white irons is much more dependent on resistance to crack initiation than resistance crack propagation. The use of instrumented Charpy tests to measure a peak load to fracture during impact to measure the materials dynamic fracture toughness has been used. Without precracking this was a good method for studying crack initiation and propagation. Others have proposed that due to the large inhomogeneity in alloys a drop weight tear tests would be better.[30]

A test rig to examine the Impact resistance of overlay materials has been developed by AITF and Suncor. They examined a number of CCO overlays and found that they tend to fall into two categories, one where the total fraction of carbides is low to moderate which means at the interface between the backing material and the overlay there is either a dendritic hypoeutectic structure or a very low frequency of carbides. The second category is where there was a high frequency of primary carbides throughout the full thickness of the overlay. As shown in Figure 3-11 the alloys that tended to have low to moderate amounts of carbides had markedly better impact resistance than the ones with higher volume fraction of carbides [83].
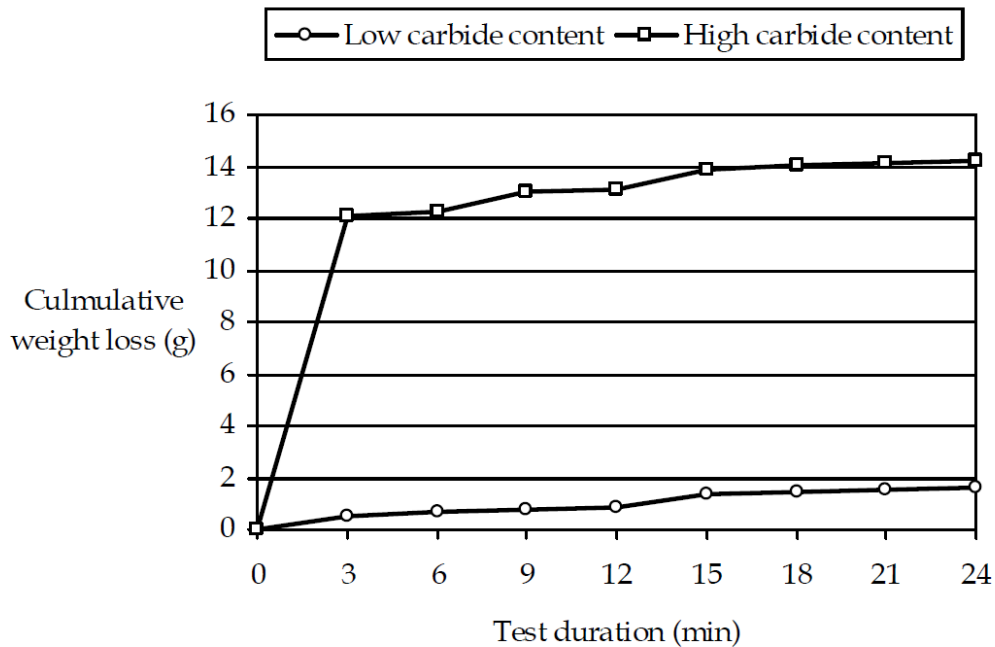
Figure 3-11: A comparison of two types of chromium carbide-based overlays, showing examples of weight loss data for typical systems [83]

61

4. Experimental Production and Characterization of Overlays

The experiments were carried out in an attempt to replicate how industrial CCOs are produced as closely as possible. This entailed the use of the same or as similar as possible parameters, products and measuring techniques between the industrial and the research produced overlays. One of the initial difficulties that were discovered was the lack of homogeneity throughout the welds. This is why where the samples were taken from and how they were analysed is of such importance and is discussed in depth in Section 5. Since one of the major problems with the industrially produced sample was the lack of primary carbides through the height of the welds the microstructural properties that may affect this such as banding, rice crispies, and cooling rates were examined in depth. Possible solutions to this problem through the use of AC welding and adjusting CTWD were also examined. In addition since it may be the large amount of dilution that is inherent in SAW that cause this banding three alternative processes was examined to determine what effect they had on the microstructure.

4.1. Experimental Setup

To produce CCOs using SAW the welding is done in CV to keep the WFS constant. To apply CCOs using SAW a powder that is high in alloying is placed down in front of the welding head. The powder is welded over using a weave technique to produce a pass that is 1 ¾" in width. The next pass is performed right next to the original one with approx. ¼"overlap in order to achieve a uniform height throughout the entire overlay. These passes are continually laid down until the desired width of plate is covered. A common size of the plates produced by our industrial partner is 2.44 m by 6.1 m. A typical example of a finished plate is shown in Figure 4-1.

Figure 4-1: Overlay Plate (Picture Courtesy of Wilkinson Steel and Metals)

The weld beads can vary in height from 3/16 to 3/8" thick. When an extra thick overlay is needed multiple layers of the overlay can be welded on top of one another. The schematic of the setup in the laboratory is shown in Figure 4-2, with the exception that only a single pass was applied in the middle of the base plate.
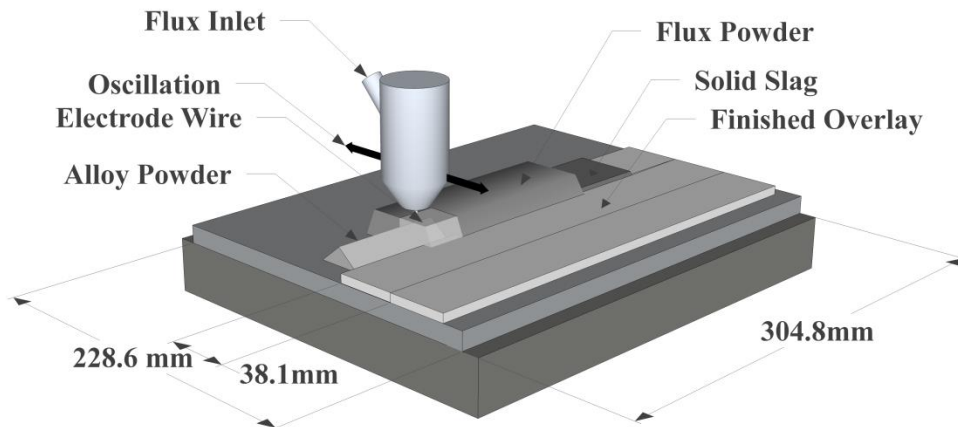
Figure 4-2: Submerged Arc Welding Setup for Chromium Carbide Overlays

Typical operating ranges used during the welding of CCO's using SAW are in the range of 30-40 V and 500-700 A. The wire feed speed and alloy powder amount are varied to control the resulting final composition. Operating parameters are also chosen to ensure complete melting of the powder, a good surface finish, and slag detachability.

The type of flux used during welding was OK Flux 10.71. This flux is an agglomerated basic flux and that can be used for DC and AC current welding. This type of flux is normally produced by mixing finely ground powders and bonding them with a ceramic bonder. The flux is then cured and then broken up and screened. [18] The wire that was used was for welding was a low carbon steel Lincoln L-61with and 3.2 mm diameter.

The power source used was the PowerWave® Lincoln ACDC 1000 SD. This machine allows for the manipulation of AC wave forms along with data acquisition through the built in weld view. The built in data acquisition system was tested against a custom built National Instruments USB-6351X acquisition system. Current and voltage sensing of the SAW process using the custom system was handled by LEM HTA 600S Hall Effect sensors and LEM LV 25-P voltage sensors respectively. The readings from power wave

manager and custom system found to match very well ensuring that the waveforms are accurate and unfiltered. The waveform data that was collected by the machine was then used to determine the heat input (HI) of the welds. Heat input was calculated by multiplying instantaneous voltage and current to get the instantaneous power during welding. The instantaneous power was then averaged out over the duration of the weld. A custom built gantry was used to control the travel speed and oscillation. The setup that all of the research SAW CCOs were produced on is shown in Figure 4-3 and Figure 4-4.
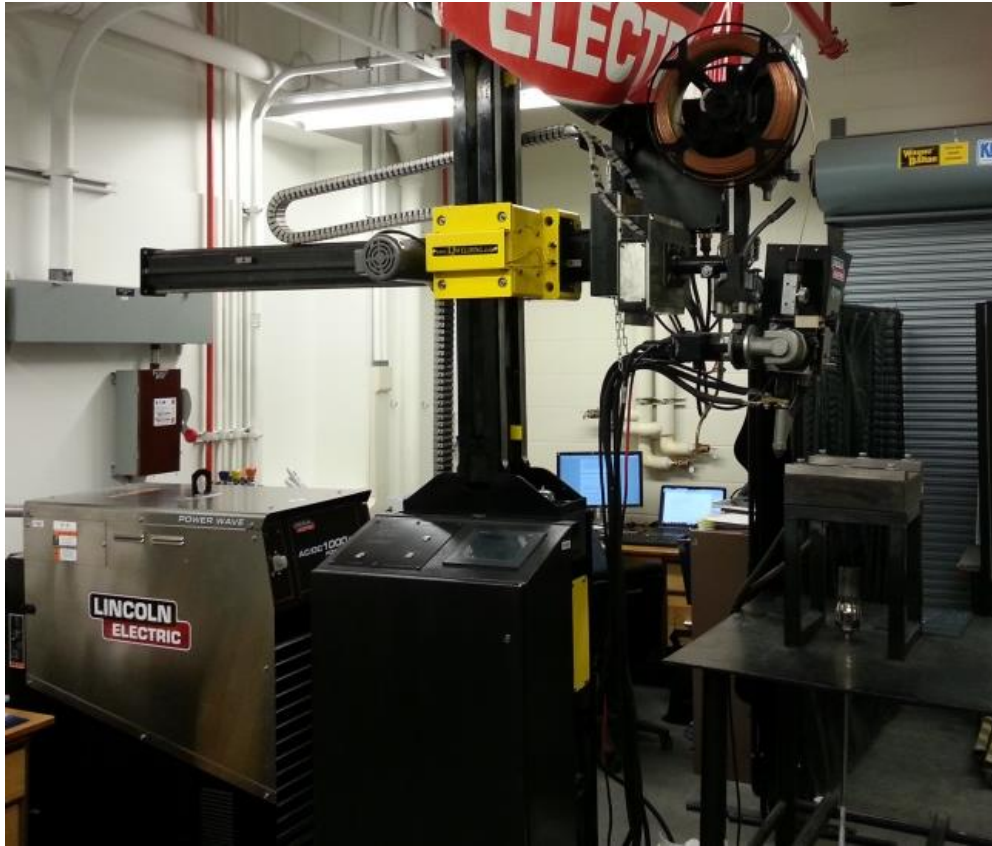
Figure 4-3: Experimental setup side view
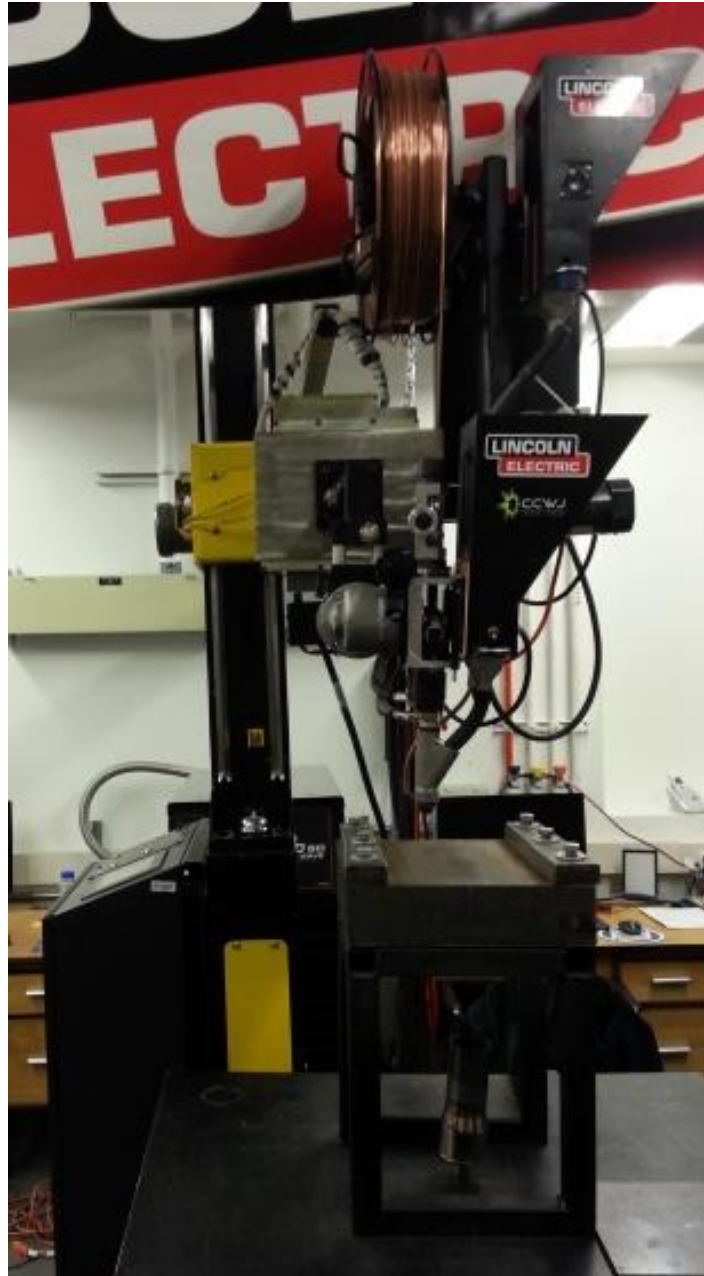
Figure 4-4: Experimental setup front view

4.2. Duplicating Industrial Sample

In order approximate the welding conditions of an industrial setting such as the one shown in Figure 4-5 as much as possible the setup was constructed so that the support plate matched the same thickness as the gantry plate used in industry.
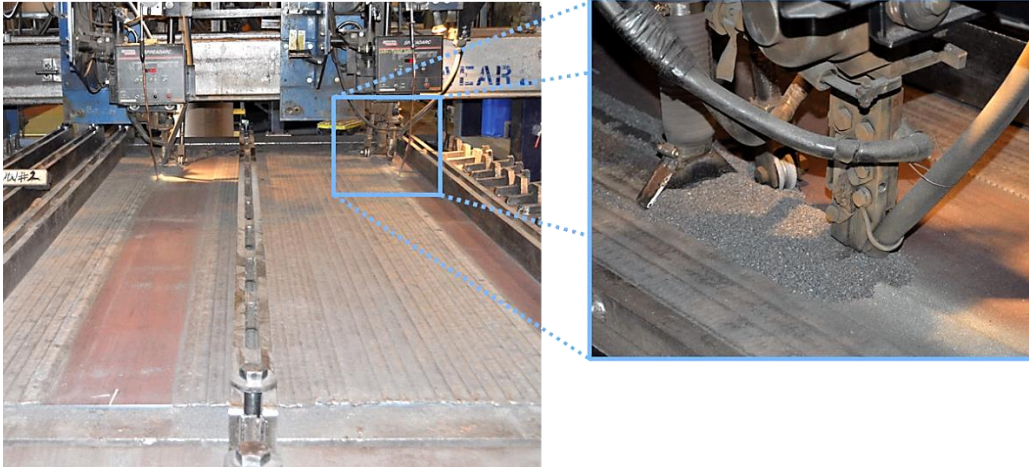
Figure 4-5: Industrial CCO Production (Picture Courtesy of Wilkinson Steel and Metals)

Also, during normal production the support and base plates are heated up by the previous passes so in order to imitate this effect the support plate was raised of the table so that a propane torch could be placed underneath to provide a pre heat. A close up of the welding surface and the torch used for preheating is shown in Figure 4-6.
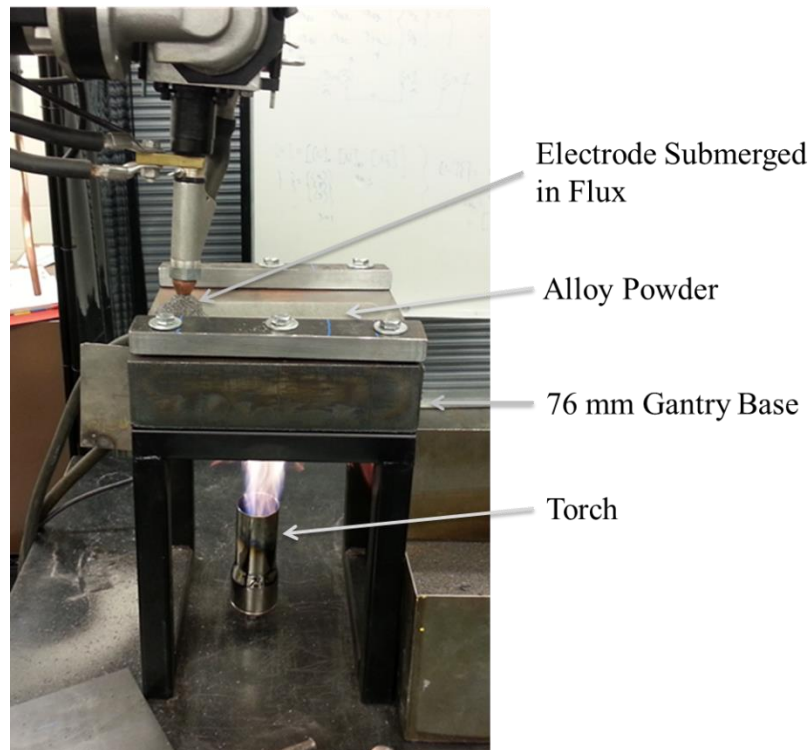
Figure 4-6: Picture of experimental setup showing 3" base plate and torch for preheating base plate

Temperature measurements were carried out of both the weld pool and the baseplate at the industrial facility as measures to use to replicate the industrial setup. The setup that the readings were taken off of a gantry that was used to produce two separate ¼ on ¼ overlay plates at the same time. A pass would be laid down on the first plate and then the power source turned off when the torch reached the end of the first plate. The gantry continued moving at the same speed. As the gantry and the welding torch reached the second plate the power source is then turned on and the pass is then laid down on the second plate. After reaching the end of the second plate the power source is once again switched off and then the whole gantry is moved back to the beginning of the first plate. In order to speed up production there are two welding heads and two power sources that are carrying out the aforementioned technique. The two weld the first plate at the same time but separated by a few feet and then weld the second plate at the same time as well.

The temperature was measured repeatedly at a few different locations of interest on the plate and gantry in order to get an idea of the heat profile in the plate. The temperature was measured ahead of the welding head where it would soon be going over and it was found that the temperature ranged between 319 -350 ^{o}K. This was taken to be a rough indicator of a so called interpass temperature. The gantry under the base plate was measured as well and the temperature was found to fall between 309 and 316 ^{o}K. When the base plate's temperature was measured right next to the weld bead immediately after being laid down the temperatures measured between 408 and 473 ^{o}K

5.   Procedure

5.1.   Sample Selection and Dilution Measurements

In order to examine the quality of the overlays metallographic samples were made of the different samples. In order to ensure that the metallography was not affected by the location where the samples were taken it was determined that samples would always be taken from the same locations based on the schematic shown in Figure 5-1. The dilution measurements were taken for the samples next to the micrograph from within the two inches designated for taking the metallographic sample.
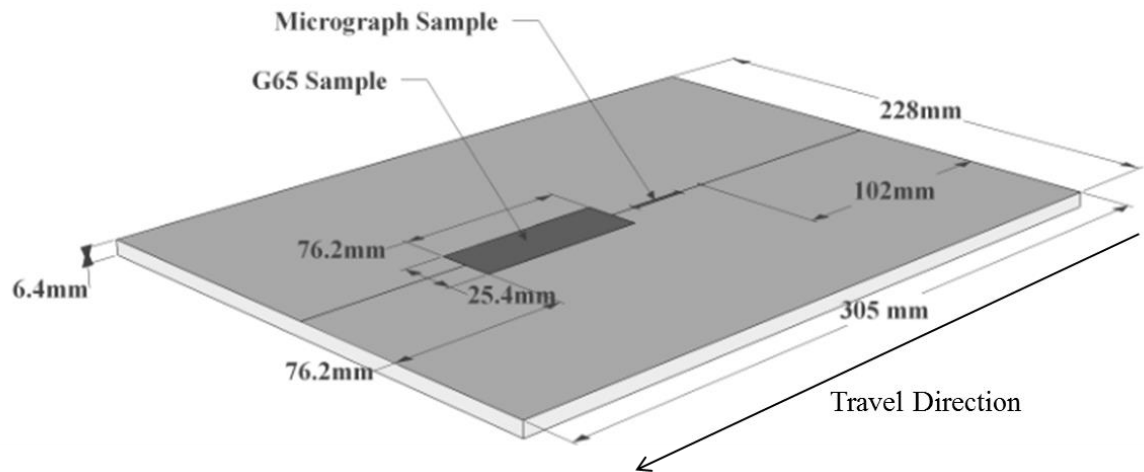
Figure 5-1: Sample locations

In addition to these considerations how the dilution measurements were taken also had to be taken into account. To calculate the dilution measurements were taken one along the longitudinal of the center line. For some of the samples two measurements were taken one at the center and 15mm off the center as shown in Figure 5-2 to account for the un-uniformity of the welds.
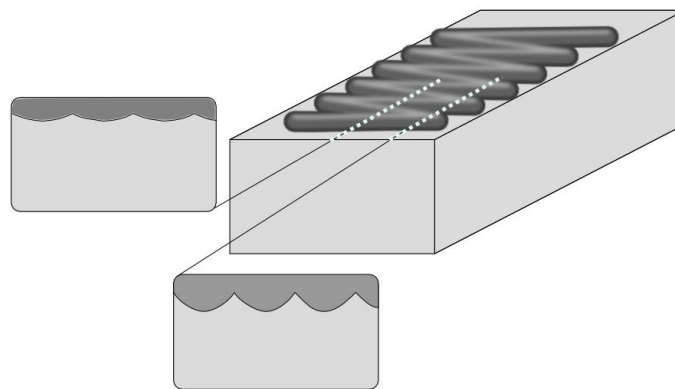
Figure 5-2: Dilution Measurement Locations

The reason that the dilution measurements were not taken from the transverse cross-sections and instead were taken from two different longitudinal sections is that depending

on where you take the sections with respect to the weave, the dilution and the profile of the penetration can change significantly. Figure 5-3 shows how a sample such as the one on the left that would have been cut along the middle of the oscillation would have significantly different shape than one cut at slightly different location as shown on the right of Figure 5-3 that was cut on with the right side of the sample being right on the edge of the oscillation. These differences in profiles are caused because the profile will be deeper if it is cut from the bottom of a weld scallop and because the penetration tends to be higher on the edge of the weld beads. This may because the welding torch spends more time on the edges because of the time for the machine to mechanically switch from travel in one direction to the other.
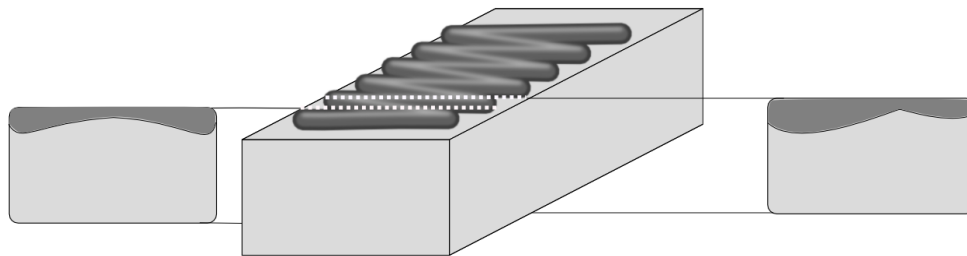
Figure 5-3: Penetration Profile

Dilution of the samples was measured using the formula shown in Equation 5-1 and with the areas described in Figure 5-4 [78]. DA is the area of dilution or the amount of the base plate that was melted, while OA is the area of the overlay that has been added and BM is the base metal.

Equation 5-1: Dilution measurement for welds

$$Dilution(\%) = \frac{DA}{DA + OA} \times 100$$

Overlay Area ▨ **Dilution Area** ■ **Base Metal** ▦
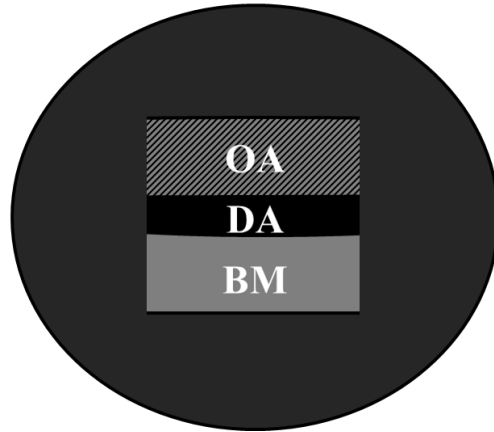
Figure 5-4: Schematic of areas and abbreviations used in dilution calculation shown mounted in Bakelite. Note OA and DA are not distinguishable in actual metallographic samples

The actual dilution measurements areas were taken by measuring the width of the samples in the pucks and then examining a picture of the puck taken in Photoshop. The measurement scale was set using the measured sample width and a line drawn across the width sample on the puck. The starting area of the base metal was then calculated by multiplying the width of the puck sample by the average height of the base plate. The actual area of the base metal left was measured using the selection tool in Photoshop. The area of the base metal left after welding was then subtracted from the original area to get DA. To get the total area of the weld OA + DA the total area of the weld metal was measured using Photoshop. Unless stated this was the technique used to measure any of the dilution measurements in this research.

5.2. Metallography Samples

Metallographic samples were then also made from along the longitudinal center of the welds. The samples were hot mounted in Bakelite and then ground and polished using an automatic polisher with 22.24 N force. For the first step of 60 grit rough grinding was carried out for 5 min; the next step was only carried out if the entire sample was ground entirely flat and even. After this multiple other grinding passes down to 1200 grit were carried out at 3 minutes for each stage. The samples were then polished using a 1um diamond suspension for 5 minutes. Any micrographs taken using a SEM BSD images were taken at this stage before continuing on to the next step. For optical micrographs the

next step was to etch the samples using 20 ml water, 10 ml HCL, 30 ml HNO_3 and 5 g $FeCl_3$ for 30 seconds.

In order to get a good representation of the microstructure a large number of photographs were taken of samples and then they were photo merged together to make large micrographs across a large width and height of the weld. The total volume fraction of carbides was then measured by using the magic wand to select all of the light areas of microstructure in the weld pool. For the samples that the primary carbides volume fraction and size was measured smaller areas were selected to be looked at because measuring the each individual carbide in a large micrograph is unrealistic. The primary carbides in the smaller areas were then selected and the total area of the carbides measured using Photoshop. The average size of primary carbides in the sample was calculated by taking the total number of all the carbides that had been measured throughout the smaller micrographs divided by the total area of all of those carbides that were measured. Because of the way the primary carbide size was measured it was decided to not do statistical analysis on the size distribution of the primary carbides because it would not be meaningful. Figure 5-5 highlights some of the steps that were taken in order to perform the analysis on the microstructure.
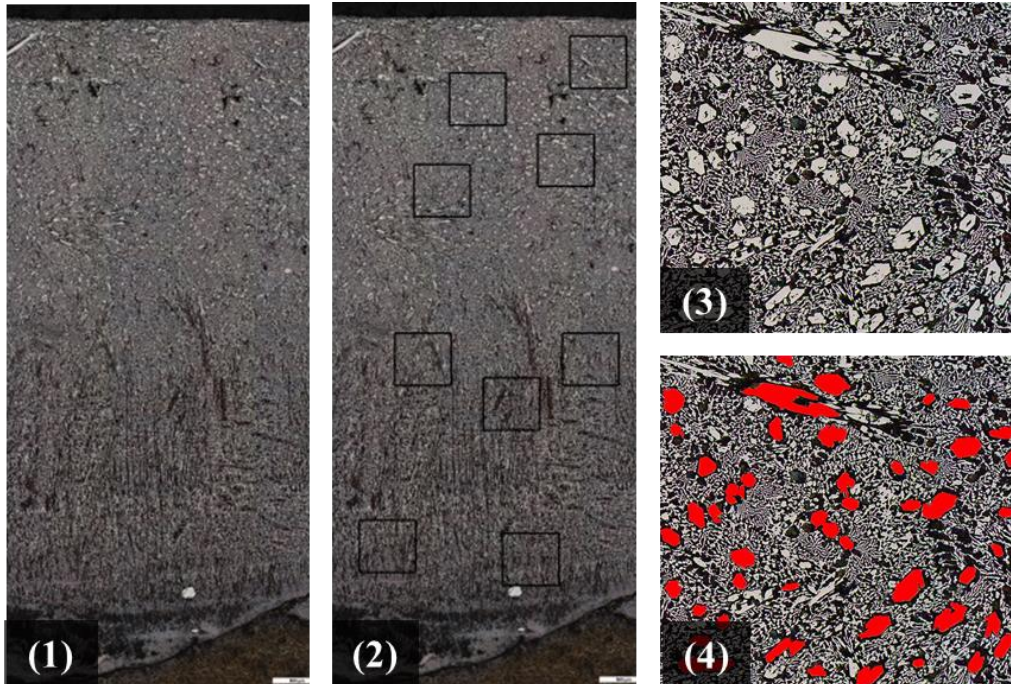
Figure 5-5:Metallographic analysis 1) original micrograph 2) micrograph showing smaller areas selected for primary carbide analysis 3) example of one of the smaller area selected 4) primary carbides selected in the smaller area to calculate carbide VF and size

5.3. Etchant Survey

One of the primary techniques for analyzing CCO's is the volume fraction of carbides. In order to do this there must be some sort of a contrast between the different phases in order to be able to distinguish between them. To achieve this etching the samples where one phase is preferentially attacked is employed. Due to the high amounts of chromium CCO's can be particularly difficult to etch because of the aggressive etchants and extended etching times needed. To overcome this problem and determine the most effective etchant for phase identification a comprehensive etchant survey was carried out. This section highlights some of the advantages and disadvantages of some of the etchants used.

The same sample was used to try each etchant to eliminate any differences in etching that may be caused by differences in composition between samples. In order to ensure repeatability and eliminate effects of previous etchants before the sample was etched it was ground to a flat finish starting with 60 grit, progressively getting smaller until finally ending with 1200 grit sandpaper and then polished using 1 μm Leco diamond suspension before each new etchant was used. After this the sample was etched using one of   the

seven different etchants shown in Table 5-1. The time the sample was etched for was varied based on the etchant used.

Table 5-1: Etchants used in survey with their constituents and amounts

Name	Components	Amount
Marble's Reagent	$CuSO_4$	10 grams
	HCl	50 ml
	H20	50 ml
Nitol	HNO3	10 ml
	Methanol	90ml
Kalling's Reagent	$CuCl_2$	2 g
	HCl	40 ml
	Water	40ml
	Methanol	40ml
Aqua Regia	HNO_3	10 ml
	HCL	30ml (50% HCl)
Diluted Sulfuric Acid	Sulfuric Acid	10 ml
	Dionized Water	90ml
		(heated up)
Murakami's Reagent	Potassium Hydroxide	2.5g
	Deionized Water	
	Potassium Ferro-cyanide	25ml
		2.5g
Unnamed Etchant	Water	20 ml
	HCl	10 ml
	HNO_3	30 ml
	$FeCl_3$	5g

Pictures were then taken using a stereoscope (Figure 5-6) and a microscope (Figure 5-7) to compare their ability as etchants. All of the etchants clearly showed a difference between the base plate and the overlays in the macro (stereoscope) pictures. The large

rice crispies appear in all of the macros with some of the large primary carbides also visible. The primary carbides are most clear in the macro etched with Murakami's. The samples were also examined under dark field to determine if there was any advantage to using dark field with any of the etchants. Dark field was not useful for analysis so the pictures are not included. However, the etchants that worked best in dark field were Kalling's, Nitol, and Aqua Regia since they did not clearly differentiate between the phases but appeared to preferentially etch the boundaries rather than the phases.
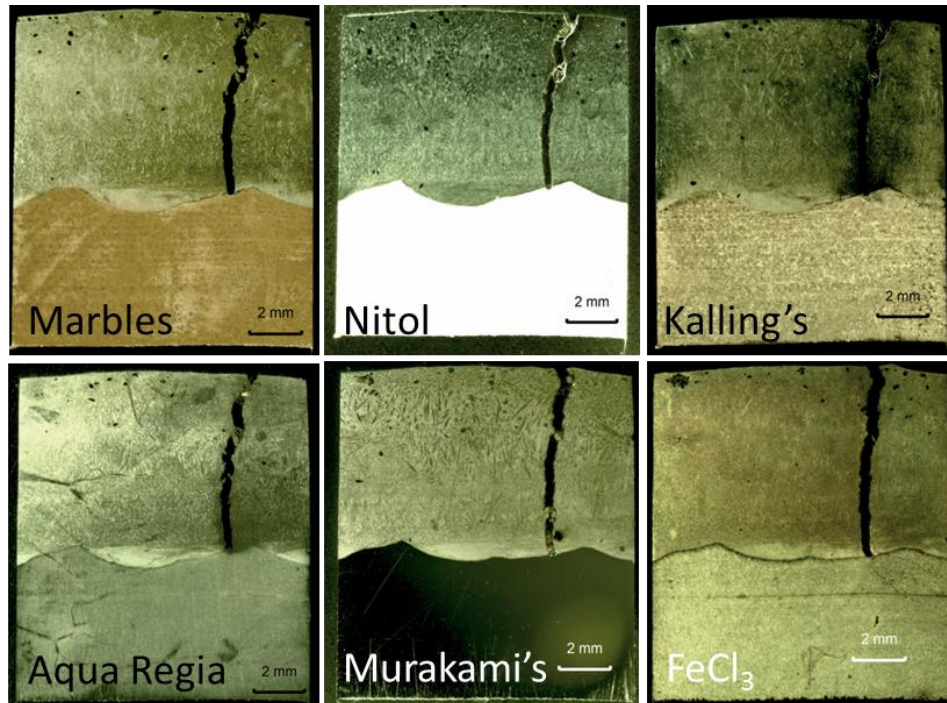
Figure 5-6: Macro's of Etched Sample
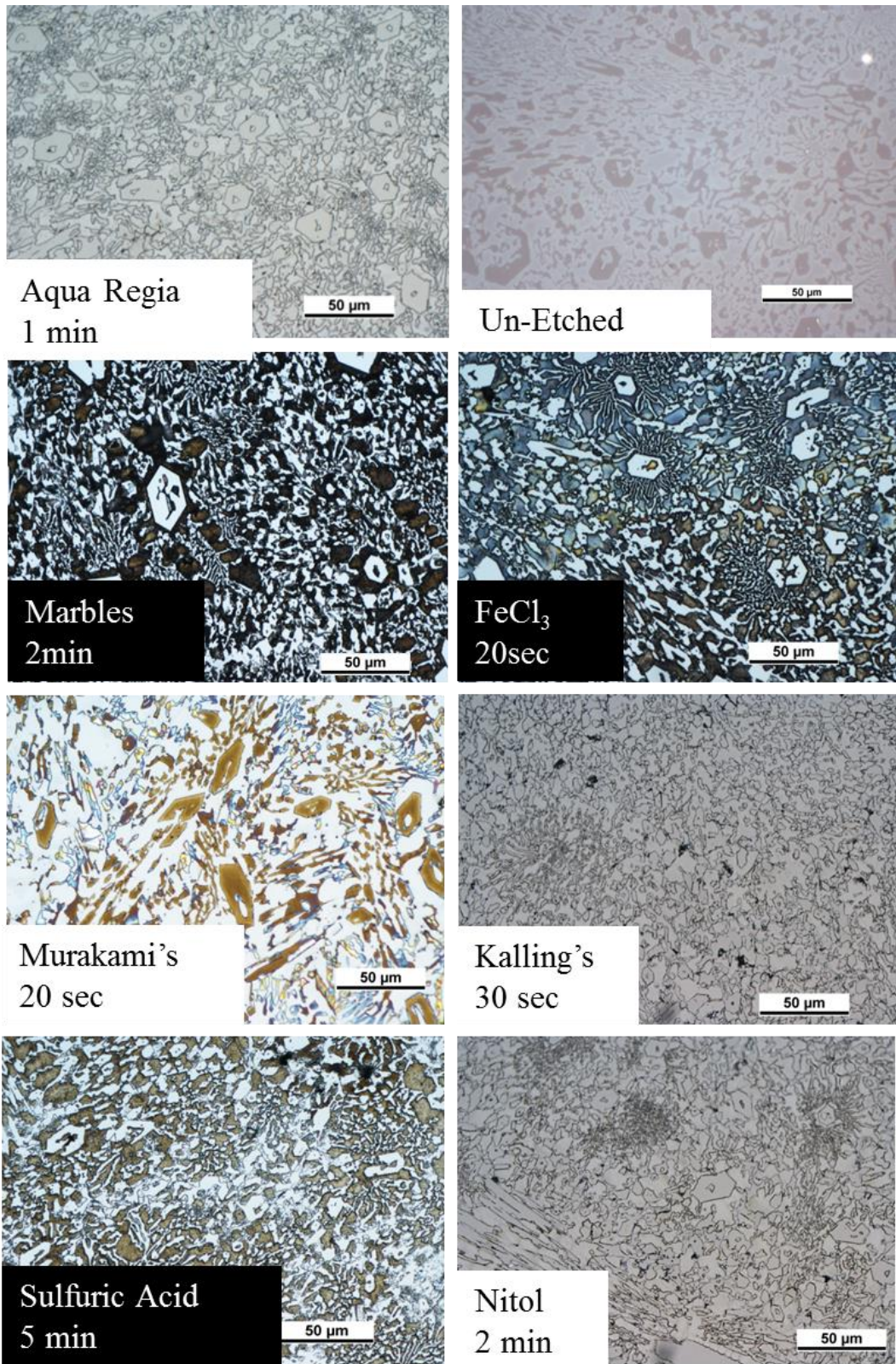
Figure 5-7: Microstructures after etching and time for etching (unnamed etchant indicated as FeCl₃)

75

In some circumstances such as SEM backscatter no etchant is needed because the image contrast is based on compositional differences. When examining the micrograph of a polished sample that has not been etched there is a very faint difference between the carbides and the austenite. The carbides are darker than the austenite. This is caused because the austenite wears down quicker than the carbides when over polished/ground. Dark field is ineffective on unetched samples and only shows imperfections such as porosity and scratches.

The first etchant that was used was Marbles Reagent. A special note should be made that when using Marble's Reagent the sample must be cleaned using isopropanol not methanol. This is because methanol causes a cooper colored film on the surface. The sample was etched with Marbles for 30 seconds and then examined. The sample appeared to be under etched so the sample was re-etched for another 90 sec for a total of two minutes etching time. The micrograph after 2 minutes etching is shown in Figure 5-7. A seen in Figure 5-7 Marble's reagent is an excellent etchant to differentiate between the austenite and M_7C_3 carbides at longer etching times. At the lower etching times the grain boundary is apparent but the coloration of the microstructure is too similar to effectively tell the microstructure apart. The carbides show up as white with the austenite becoming brown or black. Dark field microscopy is effective at short etching times but not at long etching times. At longer etchant times it is not very good for looking at the bottom of the weld overlay

Nitol was also one of the one of the etchants explored. The sample was etched for two minutes after which it was not effective for telling the phases apart because it only slightly darkens the M_7C_3 carbides. The use of Kalling's Reagent was also examined after etching for 30 seconds and much like the nitol it is not very good at telling the two phases apart. Aqua Regia was very good at showing fine details in the phase boundaries but there was little difference between the M_7C_3 and austenite.

The sulfuric acid etchant turned the austenite to a light brown color while leaving the carbides white but the etching was not uniform and small sections where the microstructure becomes finer don't appear to be entirely etched. Another disadvantage of the sulfuric acid etch is that it needs to be heated up which makes it tedious to make and use.

When making Murakami's reagent the potassium hydroxide pellets and deionized water have to be pre-mixed before adding the potassium ferrocyanide. Murakami's was very good at distinguishing between the two phases. The primary M_7C_3 carbides are colored yellow and the eutectic carbides are colored a variety of yellows, blue, white, and pinks. The large amorphous shaped carbides are colored only around their edges. It is unclear if this halo effect is showing the same compositional effect seen in SEM .Using dark field the carbides show up clearly outlined but only slightly colored. They can be green, yellow, red, and orange. One problem with the etchant is the depth of field seems to change especially where there are fine eutectic rosettes.

Using the etchant containing $FeCl_3$ leaves the carbides light and darkens the austenite to either blue or brown blackish. It is very effective and etches the austenite very quickly which makes it ideal to use for deep etching techniques. After the etchant survey was concluded it was decided that this was the etchant to use it for all of the optical microscopy.

5.4. Thermocouple Cooling Measurements

To measure actual cooling rates of the samples thermocouples were plunged into the weld pools before they solidified immediately following the torch. The thermocouples were then solidified into the weld bead and they measured the cooling rates.
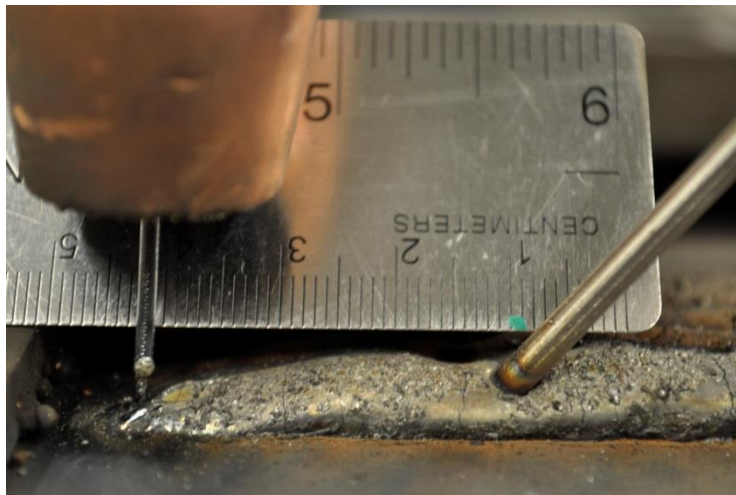
Figure 5-8: thermocouple plunged into the weld pool from GMAW1

5.5. Base Sample

As one of the goals of this research was to attempt to replicate an industrial scale production on an experimental setup, a standard sample made industrialy was needed to

be taken as a benchmark. As there are numerous different products that the industrial partner produces it was decided to focus on one of the product lines that they were having the most difficulty with, as any improvements would be more noticeable and have a larger effect than on other product lines. Therefore the product that was ultimately decided to focus on was a 6.35 mm overlay on 6.35mm base product. One of the reasons that this product line has difficulty is that it is the thinnest overlay they produce this inherently causes it to have high amounts of dilution. The operating settings for the product studied are given in Table 5-2.

Table 5-2: Operating parameters for industrial produced ¼ on ¼

Operating Variables	Values
CTWD	31.75 mm
Travel Speed	245 mm/min
Oscillation Speed	3.175 m/min
WFS	1.63 m/min
Voltage	33 V
Powder to Wire Ratio	1.75

In order to ensure that the experimental setup parameters matched the needed parameters as closely as possible all relevant values were remeasured before experiments were carried out. This means that for settings such as WFS, gantry travel speed, oscillation speed and powder flow rate were all measured prior to experiments being carried out. This is of critical importance because it is often the case that actual programed settings do not actual match true settings. This technique of taking "confirmation readings" is also carried out by the industrial partners to help improve quality control. The micrographs of the overall overlay and the higher magnification of the overlay show that the base sample has a large amount of primary carbides and that the microstructure is almost entirely hypereutectic.
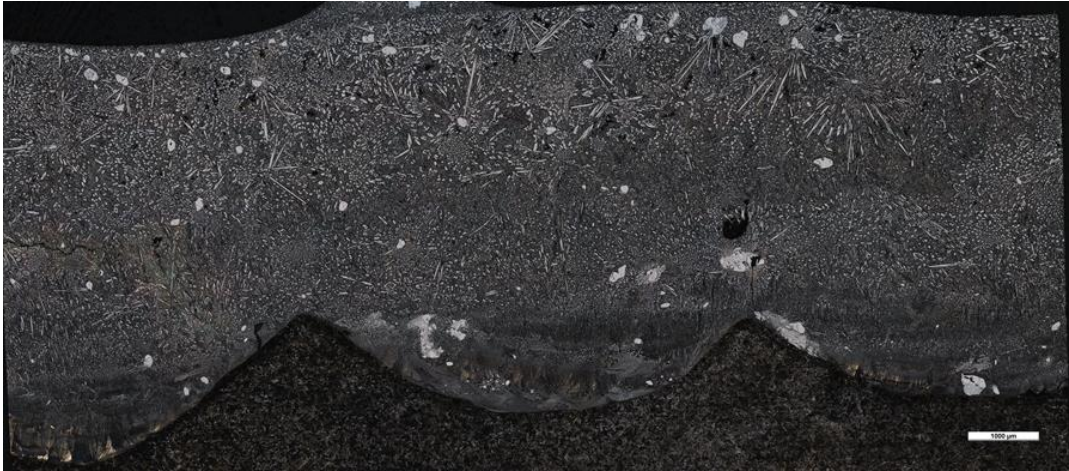
Figure 5-9: Base sample micrograph from industrially produced sample at low magnification
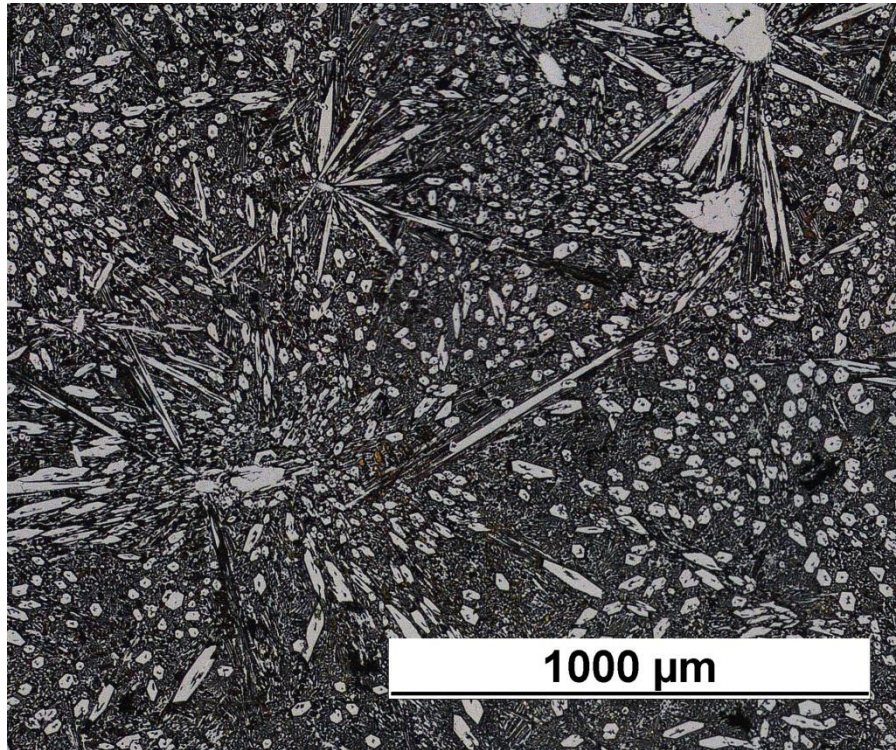
Figure 5-10: Higher magnification of microstructure of base sample

A number of different metrics were taken concerning the base sample so that the other samples could be compared to it. The measurements that were taken included the total volume fraction (VF) carbide, the total VF of hypereutectic microstructure, VF primary M_7C_3, average primary M_7C_3 size, dilution and the sample hardness. These values are tabulated in Table 5-3.

Table 5-3: Base sample microstructure and dilution measurements

Sample	Total VF Carbide	VF Hypereutectic	VF Primary M7C3	Average Primary Size (um)	Dilution	Hardness HV
Base	22.14%	93.26%	11.53%	512	12.68%	608 +/-50

The determination of the success or not of replicating the industrial sample will be discussed in the Effect of Cooling Rate section since the welds that should replicate the industrial sample are covered in that section.

5.6.   Sectioning methodology

To do 3d sectioning a sample was mounted in an epoxy puck with ball bearings. The depth change after polishing and etching was measured by using the change in diameter of the ball bearings and then plotted shown in Figure 5-11 for the polishing steps. This allowed for a procedure to be developed to get approximately 5um spacing between micrographs. 5 um was chosen as an appropriate depth between sectioning because if the blade like ones are at steep angles the 5um polishing depth should ensure that there will be overlap of carbides that are at shallow angles to the surface.

$$y = 0.002057x + 0.236678$$
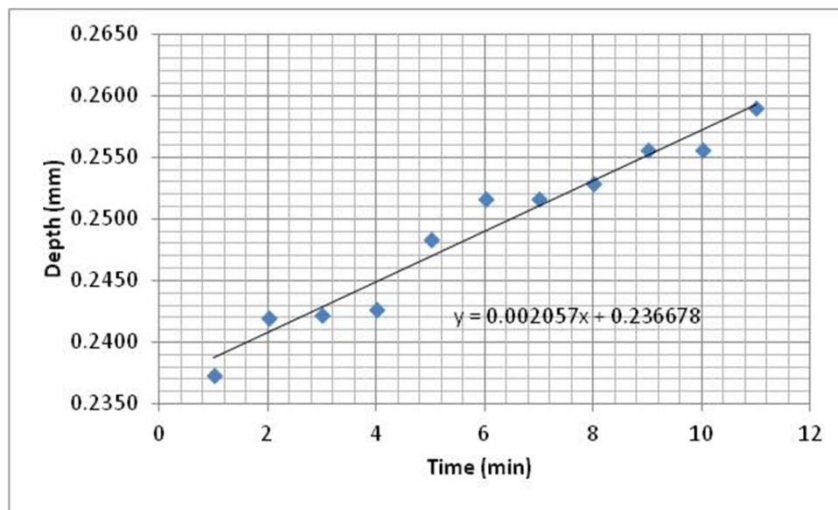
Figure 5-11: Plot of polishing time vs. depth to determine appropriate procedure for 5um sectioning schedule

After determining the appropriate schedule micrographs were taken after polishing and etching to remove 5um of materials.

In order to generate a full 3D visualization of the sectioned micrographs like that shown in Figure 6-17 each micrograph needs to undergo a series of image processing operations to separate the primary carbides from the rest of the image, and then color them appropriately. To streamline this process an in-house semi-automated program was developed in C++ where the user only needs to specify certain limits for the processing operations. Figure 5-12 shows each step of the images analysis process, where first the image is flattened into a grayscale format and the user specifies a pixel range between 0 and 255 where these pixels are copied to another image, and the rest of the image is discarded. To resolve some issues with deep scratches found in some the micrographs, a Gaussian blur operation was performed to blend these artifacts into the rest of the image. The blurring operation appeared not to distort or manipulate the rest of the image, or destroy any of the holes in the primary carbides which can be observed when comparing Figure 5-12 (a) to Figure 5-12 (d). After the image has undergone grayscale thresholding two morphological operations are performed on the image in order to break apart the remaining eutectic microstructure which can then be removed via an area thresholding operation. The first operation is called Opening, where a 3x3 paint kernel is traced around each connected component in the image and then subtracted. This breaks apart any components that are only connected by a few pixels. In order to minimize image degradation, the same kernel is then traced around, and added back to the image. This process can be repeated as necessary. The resulting image was then eroded or subtracted with a 2x2 paint kernel to ensure that all of the eutectic will be removed in the next step. Once the image has been morphologically processed, an area threshold is specified where anything below the specified size is discarded.

a) Original Micrograph   b)Grayscale Threshold + Blurring

c) Morphological Operations   d) Area Threshold + Coloring
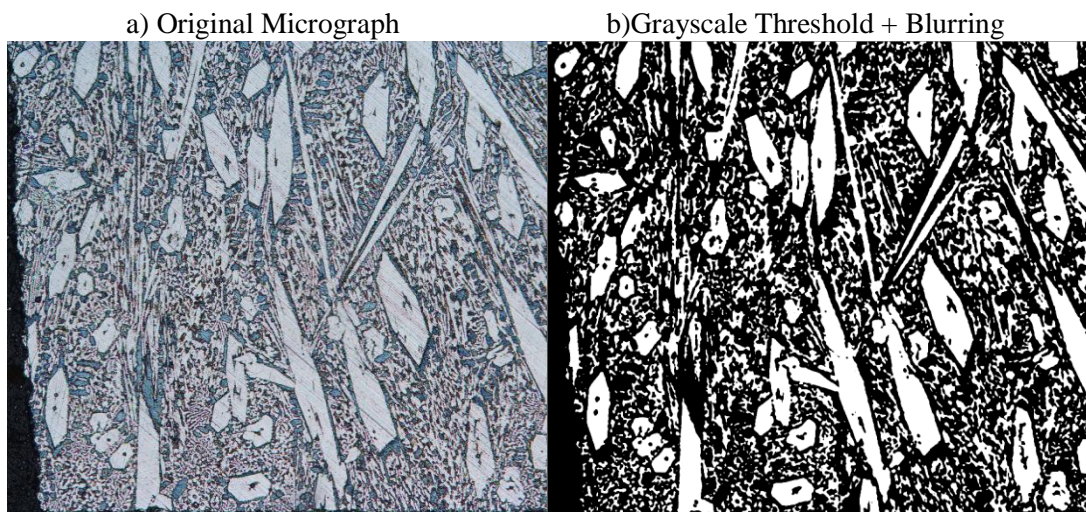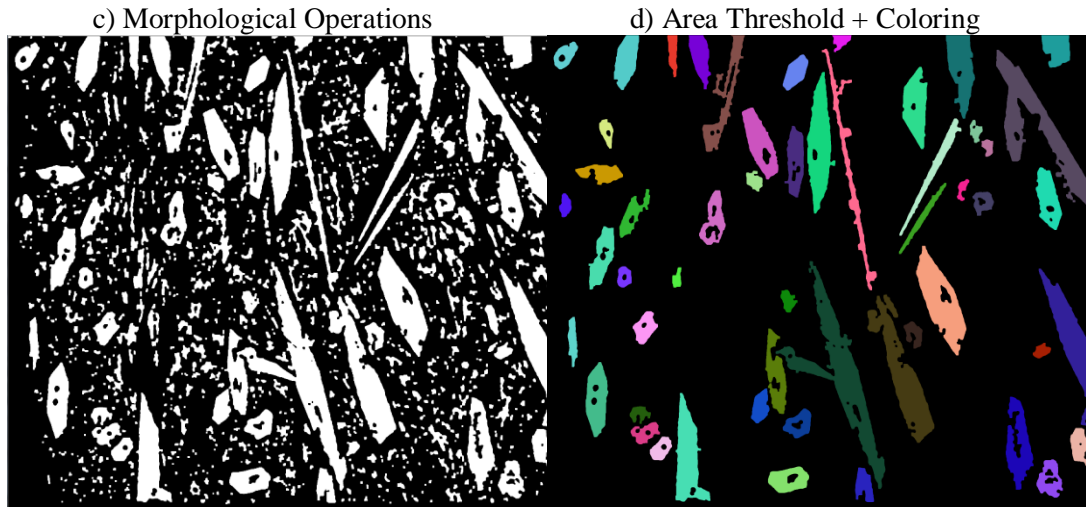
Figure 5-12: Semi-automated image analysis procedure for 3D stacking visualization where the a) original image undergoes b) grayscale thresholding where pixels outside of the specified color range are discarded. Gaussian blurring operations are then performed on the image to get rid of polishing artifacts such as scratches. The image then undergoes c) opening and erosion operations to break apart the eutectic structure. The eutectic is then removed via a d) area thresholding operation, and the remaining primary carbides are individually colored.

Once the primary carbides have been separated from the rest of the image each carbide has to be colored appropriately, so that when the images are stacked one on top of the other, each carbide has a distinct color, and can be visualized appropriately. A simple method was developed for finding the same carbide on a stack of images and coloring it appropriately based on the color of the carbide in the previous image. After randomly coloring each carbide in the first image, the location of their centroids are logged and passed to the next image. In the next image the program goes through each of the centroids logged in the previous image and determines which carbide in the current image is closest to this centroid. This process assumes that there are never two carbides in the current image equidistant to a centroid, or else they are colored the same color. This procedure also fails when two carbides start to overlap where the program considers each of them as a single component. Despite these drawbacks the program does a reasonable job of keeping the continuity of each carbide, where only a few carbides needed to be recolored by hand. After the coloring processes the images can be stacked together in 3-dimensions.

Since each carbide is individually colored it is also easy to separate individual carbides from the 3D section, where the specified color can be separated from the rest of the image. This makes it much easier to observe each type of carbide, and how it changes throughout the depth of the sample. It would also be important to be able to generate a 3D

82

continuous model from the layered image stack. Although it was not done in this study, there are medically imaging programs which can take the coordinates of a specified carbide in each slice and then generate a point cloud in 3D space. A mesh can then be added to the point cloud to generate the model.

6. Results

This section examines the results of the experimental work that has been done on CCOs for this Thesis. Some of the more interesting microstructural features are examined such as the rice crispies and how it was determined that they are unmelted powder particles is explained. The rod vs. blade discussion concerning primary carbides is examined as it can be a point of some confusion. The novel technique of 3D sectioning is employed to show clearly that the primary carbides are long hexagonal rods and that the needle like appearance of some are caused by their orientation to the sample surface. Segregation in SAW CCOs is explored since this feature may cause inferior wear resistance at the bottom of the weld overlays with the hope of better understanding it will lead to the ability to avoid it. The effect of the cooling rate on CCOs is examined to determine how it influences the microstructure. How advances in welding power sources such as AC welding can be applied to help limit dilution and the effect on the microstructure on these overlays is explored. Finally the effects that CTWD has on the resulting mechanical properties are examined.

6.1. "Rice Crispies" (Unmelted Powder)

An interesting aspect of the microstructure of chromium carbide overlays is that there are often large rounded phases in the microstructure. Figure 6-1 shows how these particles appear using EDX in a SEM and Figure 6-2 shows there appearance using optical microscopy. They were unexpected as they do not appear in literature. Upon discussion with our industrial partners it was discovered that they were known as rice crispies. They believed them to be unmelted particles. Their belief was also that they are associated with a poorer product because they rob the melt of the chromium and carbon needed to form M_7C_3 carbides. However, these understandings are based on passed down knowledge and not empirical evidence. This led to the decision to examine them more closely.
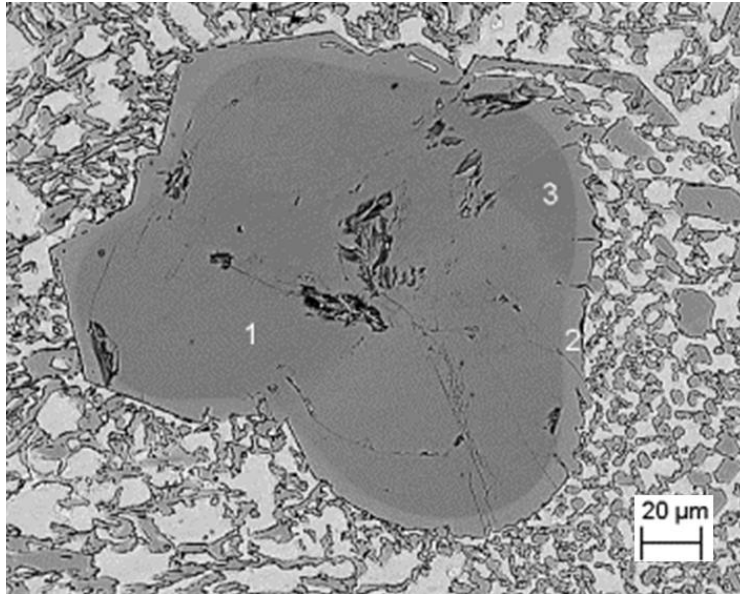
Figure 6-1: SEM backscatter image of rice crispie
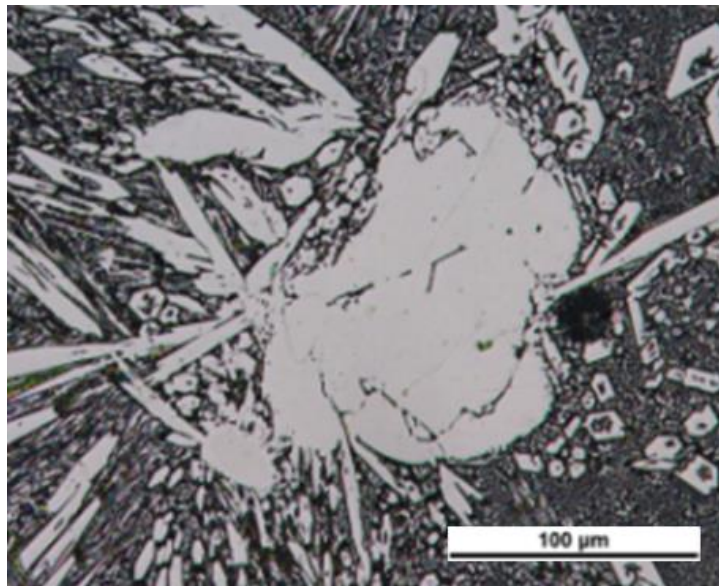
Figure 6-2: Etched micrograph of ricecrispie

To determine if in fact the large rice crispies are unmelted powder particles EDX analysis was carried out on both the powders before they were put into the weld pool and of the rice crispies. Figure 6-3 shows five different rice crispies that EDX was performed on. These rice crispies were representative of the types seen throughout the different samples. Their respective compositions are listed in Table 6-1.
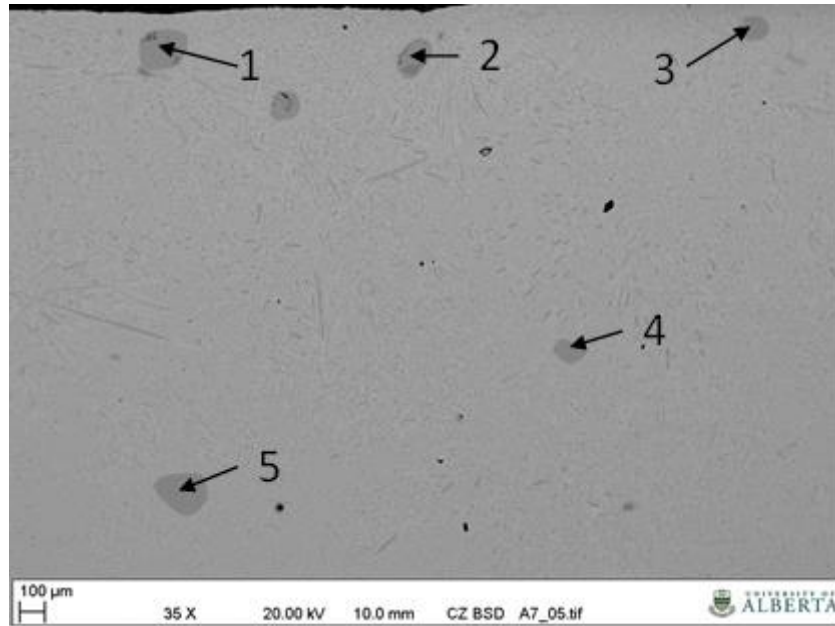
Figure 6-3: Points where EDX was taken

Table 6-1: Composition of Rice Crispies

Sample Point	Cr wt%	C wt%	Fe wt%
1	74.16	8.35	17.49
2	71.54	8.37	20.09
3	76.97	8.15	14.88
4	74.19	8.09	17.72
5	74.26	8.2	17.55
Average	**74.22**	**8.23**	**17.55**

The second step to determine if the rice crispies were unmelted particles was to examine the alloying powders that are added. To do this the powders were dropped over a SEM holder that had a layer of double sided carbon tape across the top. The specimen holder was then turned upside down and loose powder was knocked off. The specimen holder was then placed in the SEM and the five particles labelled in Figure 6-4 were analyzed to get the compositions in Table 6-2.
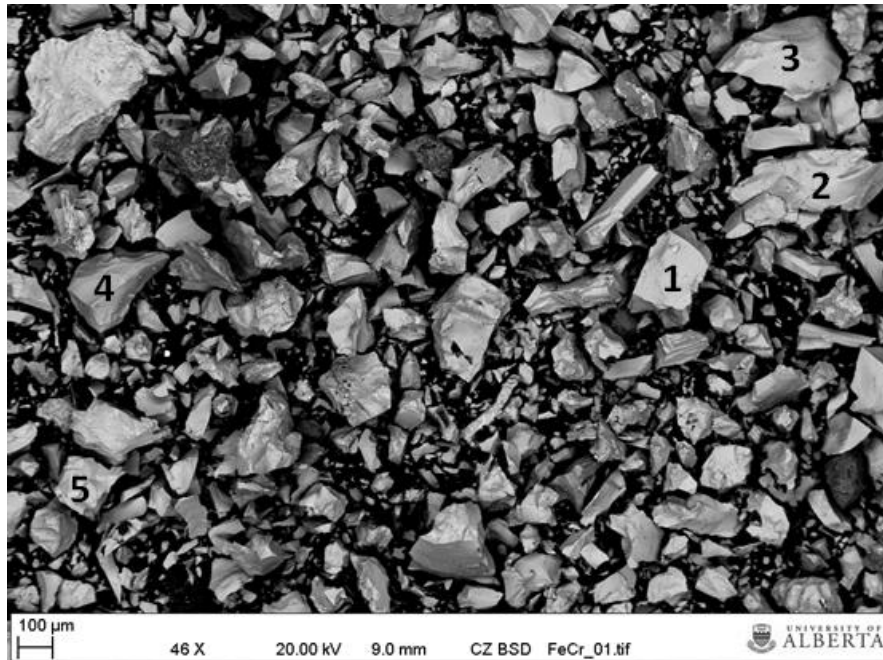
Figure 6-4: Shows five particles that were chosen from ferrochromium powder for EDX analysis

The values in Table 6-2 had much more scatter in the data than the composition of the rice crispies. One possible cause for this variation and differences in the powder composition and the rice crispie composition could be caused by using un-cleaned un-separated powders [84]. The high carbon readings could have also been caused by unintentional pickup off the carbon tape that the particles were mounted on.

Table 6-2: Composition of ferrochromium powder particle

	Cr wt%	C wt%	Fe wt%
Particle 1	77.22	8.78	14
Particle 2	72.28	10.68	17.03
Particle 3	75.85	7.47	16.68
Particle 4	73.59	12.61	13.81
Particle 5	65.44	9.14	25.42
Average	**72.88**	**9.74**	**17.39**

Comparing the two different compositions we find that at a 95% confidence level there is no evidence to support that the means are statistically different. This tells us that there is

a very good chance that the rice crispies are in fact unmelted powders as previously hypothesized.

The next step was to try to determine the effect that these unmelted particles have on the mechanical properties of CCO's. The first step was to determine the hardness of the particles using a micro hardness tester to choose points solely on the rice crispies as shown in Figure 6-5 .
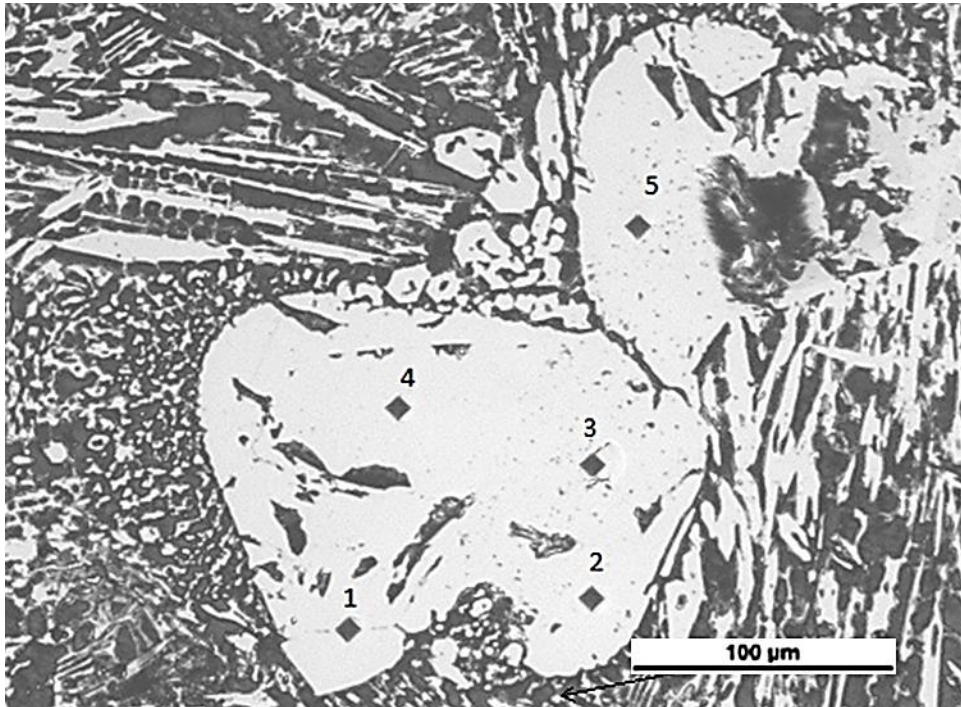
Figure 6-5: Rice crispie hardness testing indents can be seen on the large carbides

Hardness testing on two rice crispies showed the average hardness of them to be 1873 $HV_{.1}$ +/- 55.35. The indenter load had to be at 100 g force in order to minimize the amount of cracking that was occurring next to the indents. Ten points from two different rice crispies were taken to get the average values.

To examine the effect they have on wear resistance the wear surface of a sample that was tested on a G65 machine was examined. A close up of one of the rice crispies is shown in Figure 6-6. The rice crispie appears to be sticking out further than the other carbides and the matrix which would indicate that the rice crispie has better wear resistance.
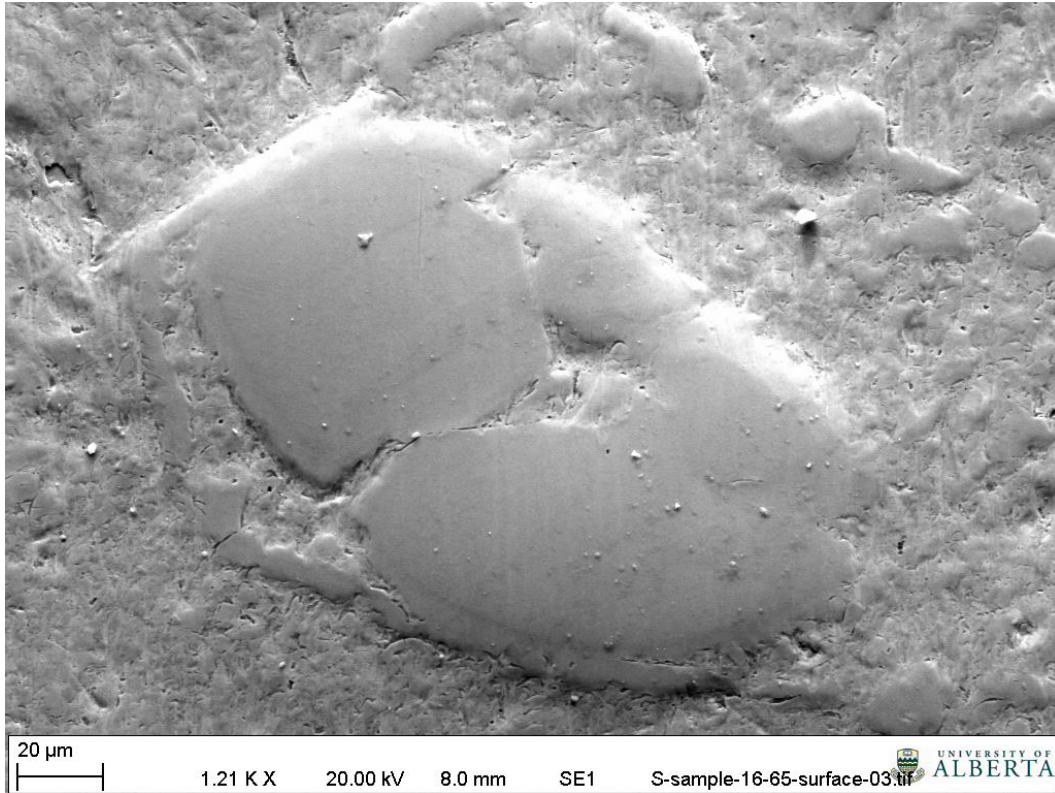
Figure 6-6: SEM SE imaging of large rice crispie in SAW CCO

In the secondary electron imaging of a particle in Figure 6-7 (A) we can see how the matrix and the primary carbides appear to have been worn away more than the unmelted particle. Figure 6-7 (B) and the corresponding EDX analysis in

Table 6-3 of the rice crispie, a primary carbide, and eutectic austenite indicate that the carbide is higher in carbon and chromium.
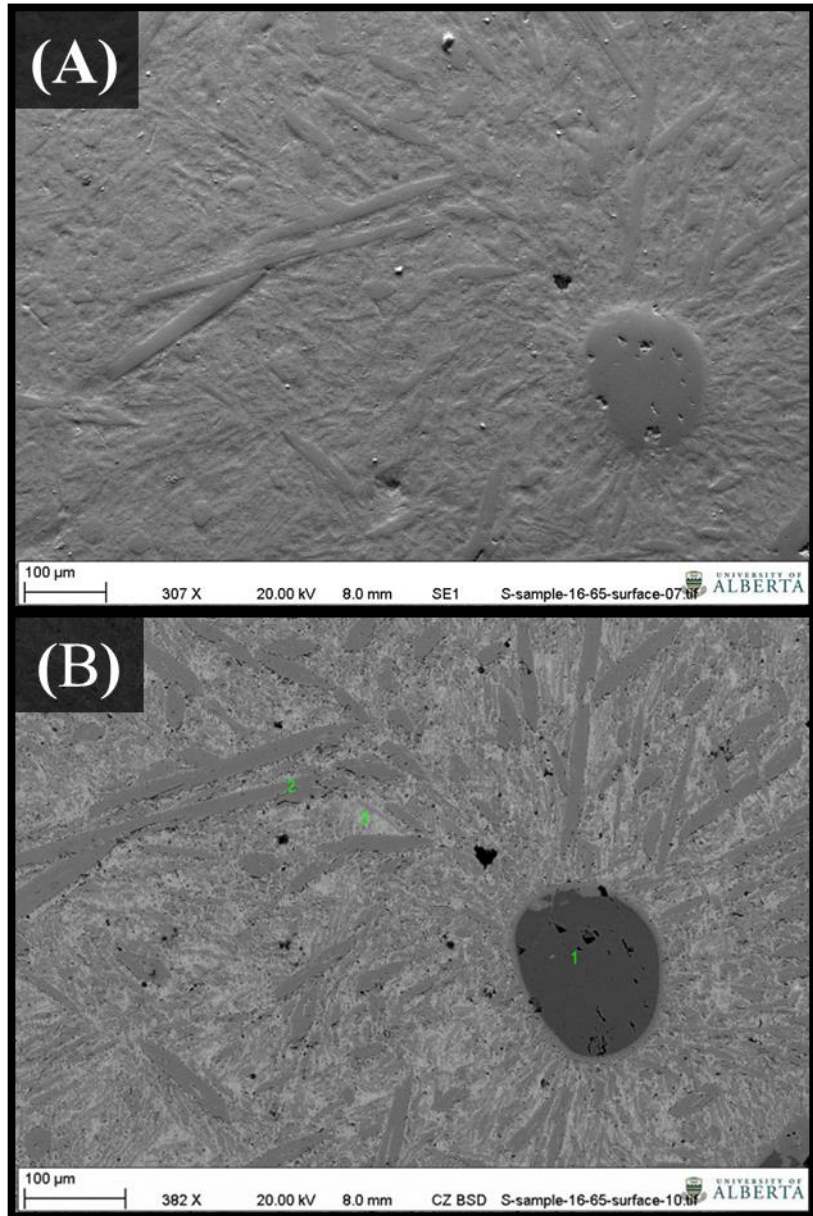
Figure 6-7: Wear surface of G65 sample (A) SE imaging showing topographical contrast (B) BSD imaging showing compositional differences and points where EDX was taken

Table 6-3: Composition of particle on wear surface

Sample Point	Cr at. %	C at. %	Fe at. %
Rice Crispie	58.0	38.36	3.64
Primary M$_7$C$_3$	42.80	28.26	38.66
Eutectic Austenite*	12.72	19.29	63.76

*Balance of Eutectic Austenite is Mo 4.23 at. %

The rice crispies also appear to form a layer of M_7C_3 carbide around the particles that are closer in composition to the primary carbides than the unmelted powder. An example of this is shown in Figure 6-8. The center of the unmelted particle has a ratio the of Cr:Fe that is much higher than the primary carbides as shown in Table 6-4.
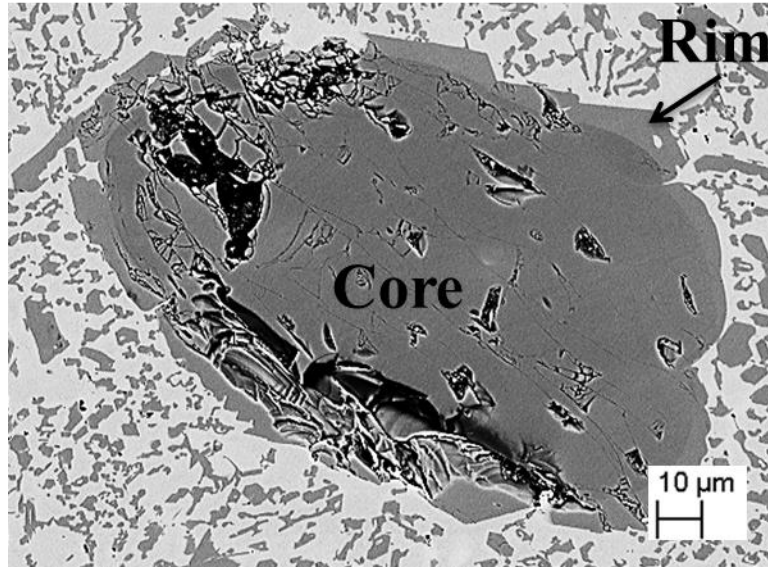
Figure 6-8: SEM BSD imaging showing difference in composition between core and rim

Looking at the mapping of the elements at a rim in Figure 6-9 there is a clear change in the Cr and Fe amounts.
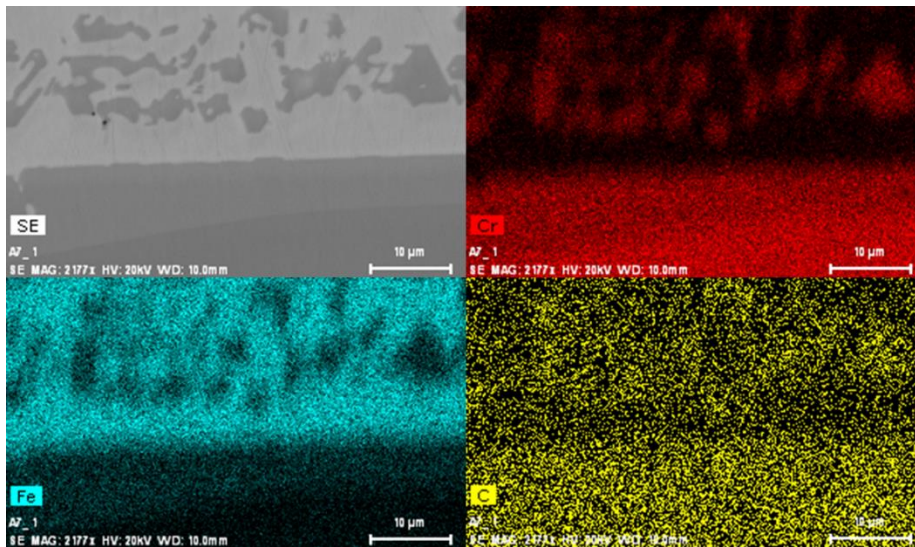
Figure 6-9: EDS mapping of rim

It appears that these particles may also act as heterogeneous nucleation points. The evidence of this is that the rim appears to be nucleated on the surface of the unmelted particles because they are the same composition as the primary carbides. Another indicator that they may be working as heterogeneous nucleation points is the starburst that radiate from the some of the rice crispies as seen in Figure 6-10.
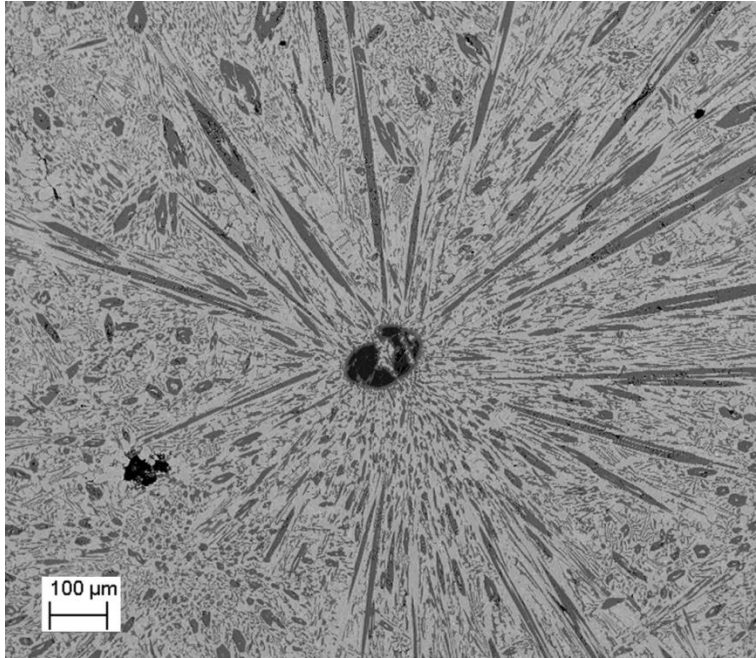
Figure 6-10: Star burst radiating out from rice crispie

A review was done looking at eleven different rice crispies to determine if any pattern could be developed to differentiate when a star burst would form and when one will not. This was done by getting a composition of a large area of the overlay close to the rice crispies, the core of the rice crispies, the rim of the rice crispies and primary carbide close to the rice crispie and finally a small area of eutectic close to the rice crispies. An example of the values of one of the rice crispies and the corresponding areas around it is given in Table 6-4. The rest of the data can be found in appendix A.

Table 6-4: Compositions around rice crispies

Wt%	C	Si	Cr	Mn	Fe	Mo
Rice Crispie	8.01	0.02	71.65	0	20.33	0
Rim	7.20	0.04	55.12	1.17	35.93	0.55
Eutectic	3.61	0.33	23.55	2.02	69.98	0.51
Carbide	7.47	0.04	52.74	1.14	37.86	0.74
Overall	3.96	0.32	20.66	2.32	71.94	0.79

Examining the data a few trends appeared. Rice crispies with stars radiating out from them tend to have higher carbon amounts greater than 11 wt. % in the core of the rice crispies compared to 8-9 wt. % when no star burst is present. They also have upwards of 10 percent more chromium in the core. Rice crispies that have primary carbides radiating from them have rims that also appear to have higher amounts of Cr and C.

Another thing that may be related to the rice crispies and carbides radiating out from them was that after performing a deep etch for over 12 hours and examining crack surface in the SEM there were circular areas that appeared to have carbides radiating out from them.
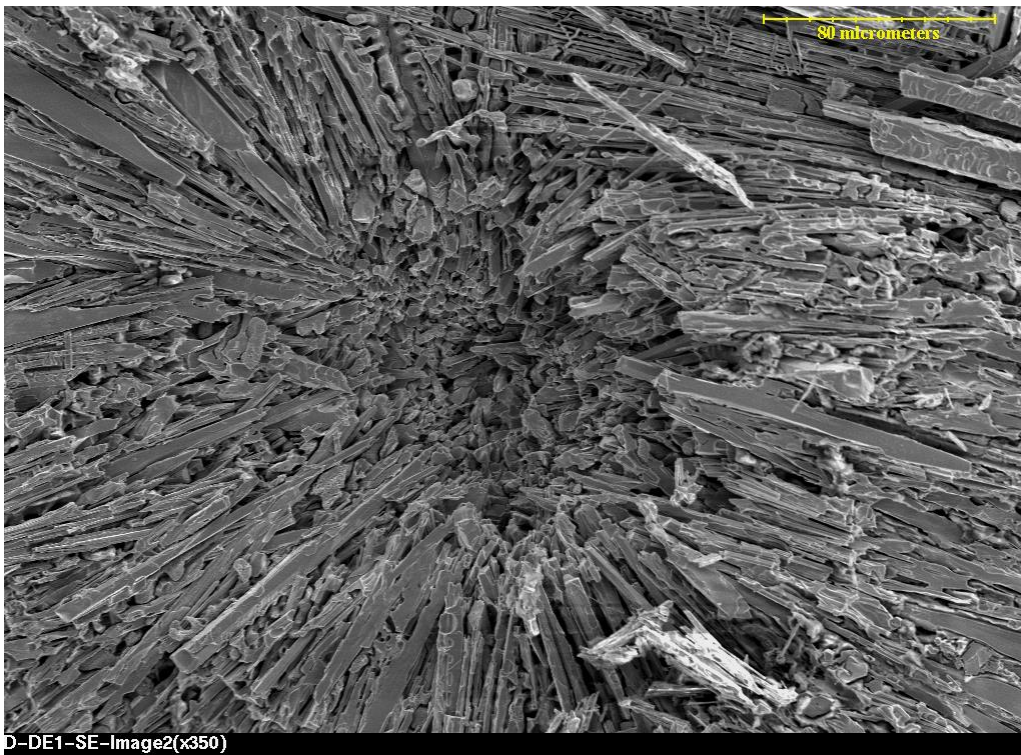
Figure 6-11: Rods radiating out from where a carbide may have been

6.1.1   Discussion

The examination of the chemical analysis of the rice crispies and the ferrochromium powders showed conclusively that the rice crispies are in fact just unmelted powders. Their effect on the mechanical properties of the overlays is promising. As shown their average hardness of 1873Hv is higher than the range of 1200 to 1800Hv expected for primary carbides. This higher hardness could possibly be explained by the larger amounts

of Cr in the rice crispies [30]. The high hardness of them could help improve the overall wear resistance of the overlay and examining the wear scar of a G65 sample it appears that they do wear out slower than the matrix and the primary carbides. The one counter claim that can be made is that they may be depriving the rest of the microstructure from additional chromium and carbon that would increase the volume fraction of M_7C_3 carbides [43, 59].

The examination of the rice crispies also showed that they often had rims of carbide along their peripheral that had compositions closer to the primary carbides than the unmelted particles. This means that any unmelted powder could possibly act as heterogeneous nucleation points for the primary carbides [33]. How the carbide rods appear to radiate outwards from the carbides may also indicate this is the case. This is not clear though as there could also be other factors at play such as constitutional undercooling and temperature gradients around the large carbides.

6.2.   Rod vs. Blade

Many people discuss the blade and rod like morphology of the primary carbides and use singular examples as explanation for the different appearances in morphology   [21, 55, 56]. This section attempts to unite the different reasoning's and show them more clearly and well defined then has been done before.

The first step was to examine how the orientation of sectioning can affect the morphology of the carbides we examined the surface of GMAW taken along the transverse in Figure 6-12 and from the top of the weld in plane with the base plate as shown in Figure 6-13. These figures show that in one sectioning plane the morphology is very different from when the morphology in a different sectioning plane implying that the morphology is based on sectioning angles to the growth of the carbides [48]. Interestingly the eutectic microstructure also takes on a very different appearance.
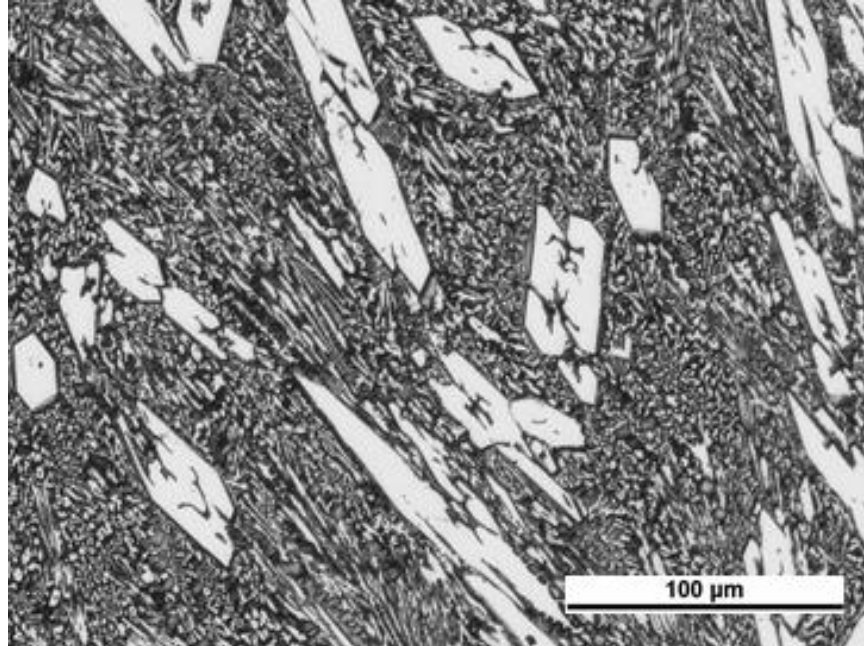
Figure 6-12: Transverse of GMAW
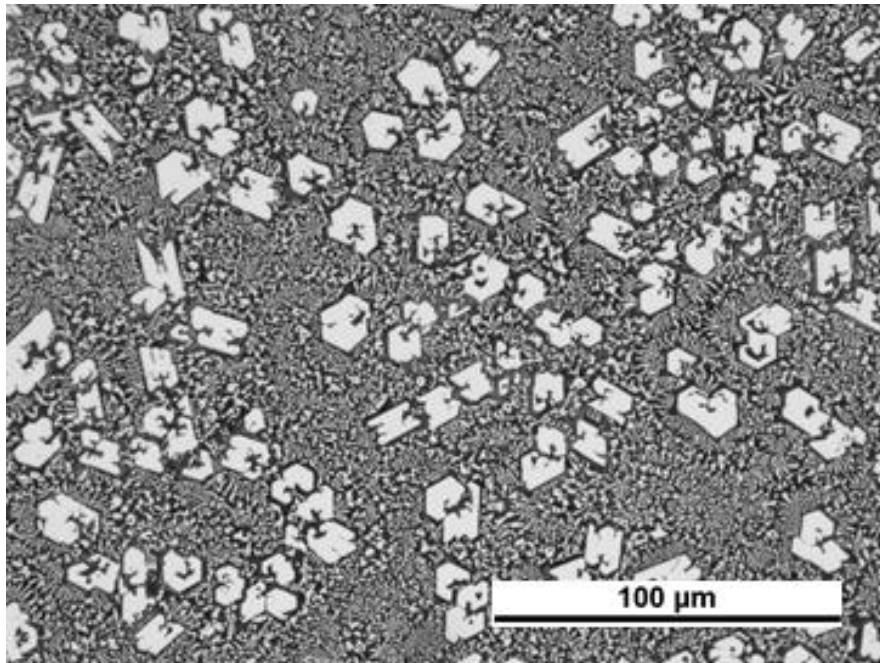
Figure 6-13: Top down view in plane with base plate

The deep etch technique was then used to examine the 3 dimensionality of the carbides. To do this the samples were etched in the same acid to etch for optical microscopy but left in the solution for 24hrs. The samples were then cleaned in isopropanol and the cut

edge was examined using secondary electron imaging in a SEM. Figure 6-14 shows what the surface looked like after the deep etching. The smeared edges of the carbides are from the cutting tool. The outline of the hexagons has been drawn in to represent the hexagonal faces as they would appear in a normal metallographic sample. The image shows that the carbides that are less perpendicular to the cut surface appear more elongated than ones more perpendicular to the surface.
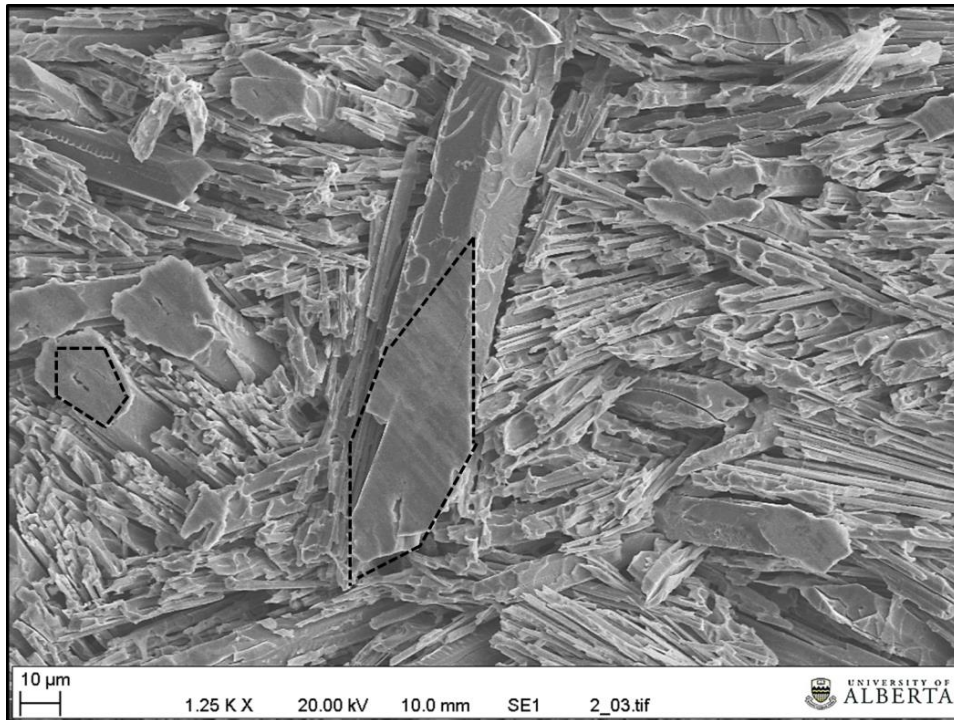
Figure 6-14: Deep etch secondary electron imaging showing hexagonal faces and the length of the carbides and differences in orientation to the surface

Looking at a relief crack surface in that was also deep etched it can be seen that the primary carbides are much longer in length than in width. The morphology of the fibrous eutectic carbide is also apparent in Figure 6-15.
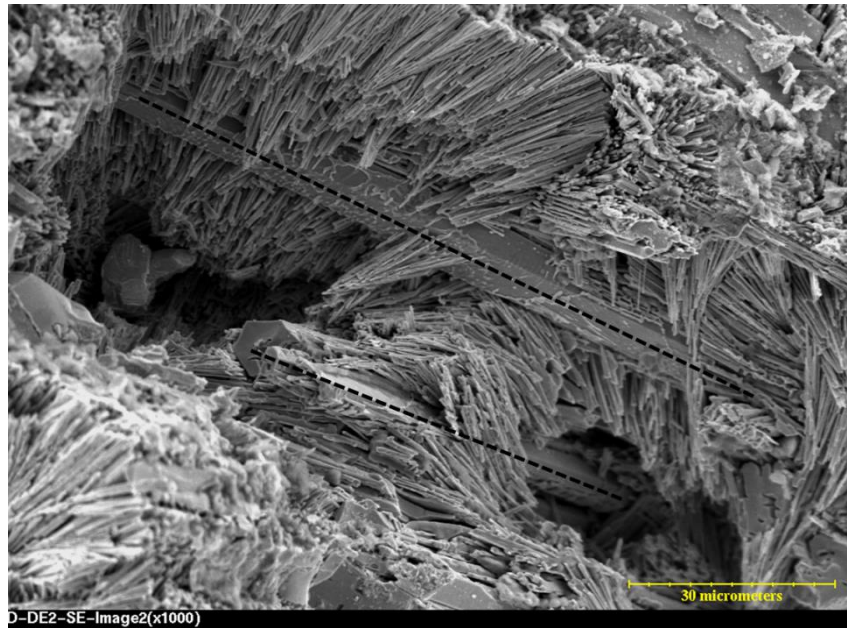
Figure 6-15: Deep etch surface of relief crack using SE imaging highlighting length of primary carbides and morphology of eutectic carbides

6.2.1   3D Sectioning

The previous results are good indicators that the rod and blade like morphologies come down to sectioning planes, however in order to conclusively prove the technique of 3D sectioning was employed. This has the added bonus that the actual structure and growth of the rods is not well understood and the sectioning technique may help better understand this.

Figure 6-16 shows six of the 62 photos taken that were used in the sectioning program. They were taken in progression starting at micrograph one and working downwards into the sample consecutively. Examining the micrographs it can be seen that the blade like ones move across the width of the sample quickly while the smaller hexagonal ones stay relatively stationary.
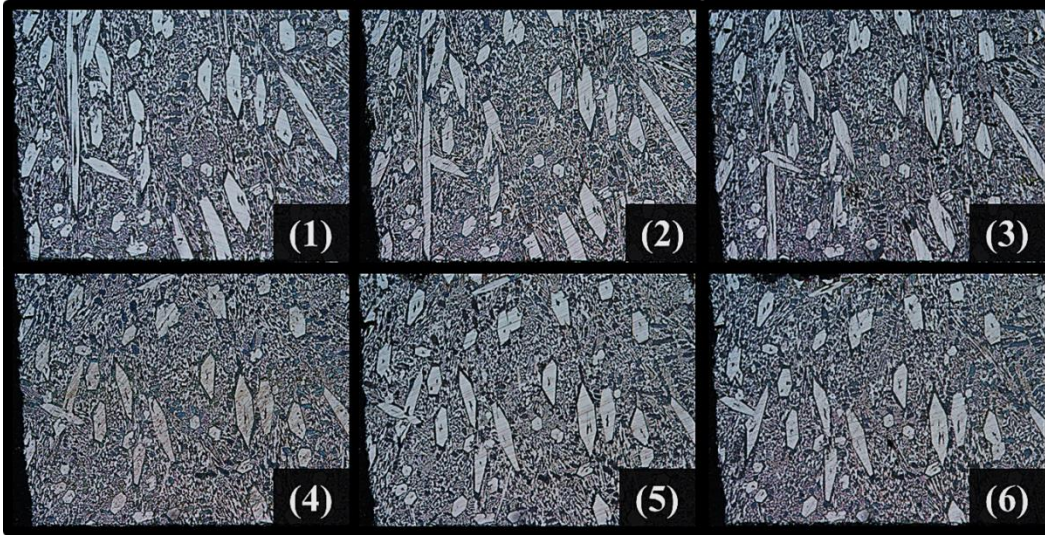
Figure 6-16: Example of raw photographs used for 3d sectioning. Photos were taken in order 1 through 6

After this a program was developed to stack the different layers. The total cell that was examined was 300um by 600um by 600um and is shown in Figure 6-17.
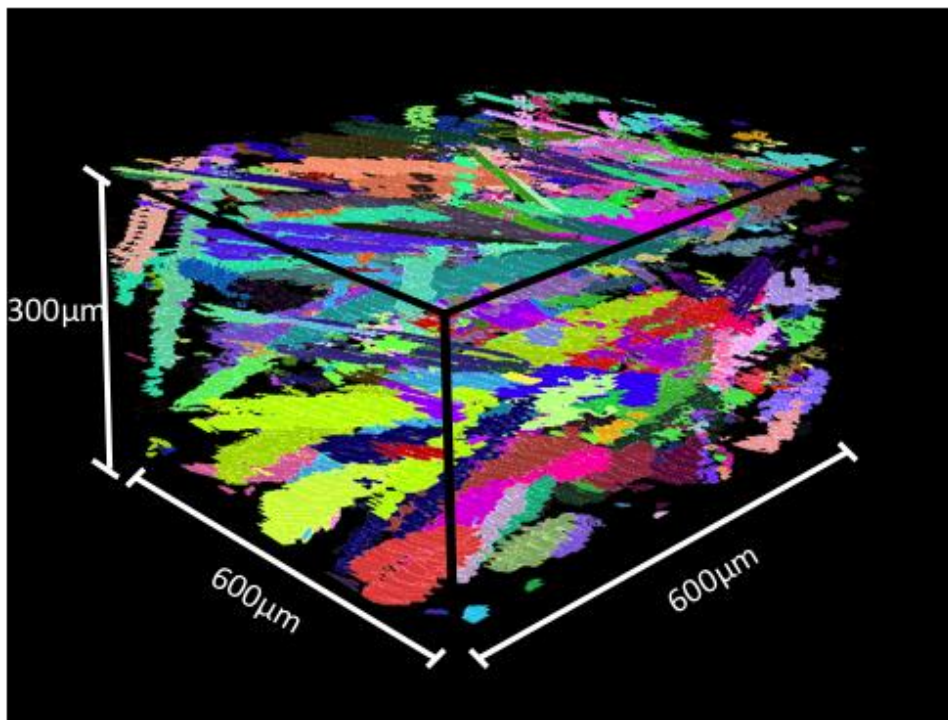
Figure 6-17: Complete area of sample sectioned with the rendered 3dimensional cell

The program written allows controlling of the number of layers visible along with their stacking distances and opacity in order to better analyze the microstructure. In Figure 6-18 we can see how the rods that are growing in the direction of the sectioning vary in position very little and the sides are close to the same size as highlighted by the two on the right that are circled, while the ones that are not orientated perpendicular to the sectioning surface seem larger and elongated such as the two ones on the left that are circled.

Figure 6-18: Sectioned layers illustrating the movement of more blade like compared to rod like in the width of sample

6.2.2   Cored structure of the hexagonal carbides

Of particular interest is the cored structure of the primary carbides; as little work has been done to examine it. The center of the carbides was examined in depth in hope to better understand why they form. The cores of some of the primary carbides of deep etched samples were examined in Figure 6-19 and at higher magnification in Figure 6-20.
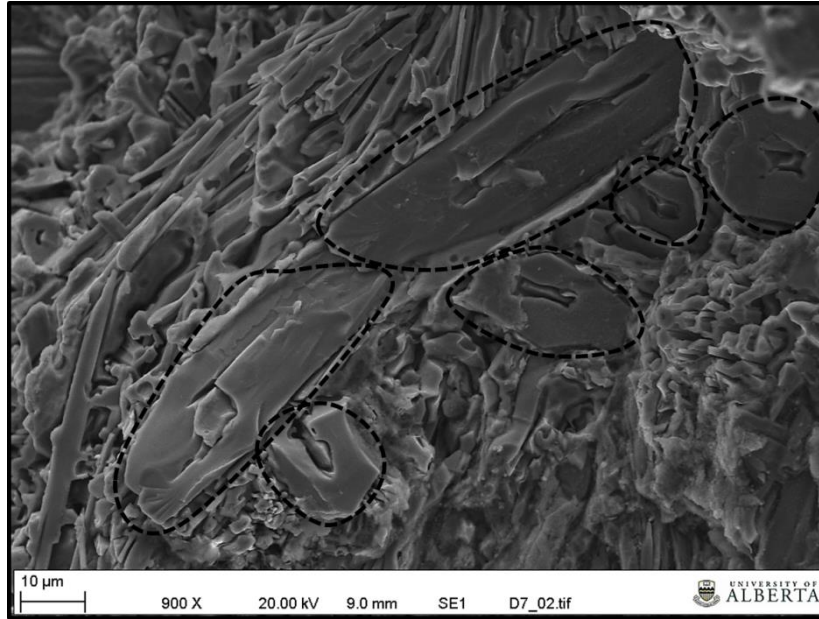
Figure 6-19: Examination of core of primary M₇C₃ in deep etched sample

Examining the samples it appears that the cores may not continue through the entire length of the primary carbides and may be pockets of austenite rather than uninterrupted austenite cores.
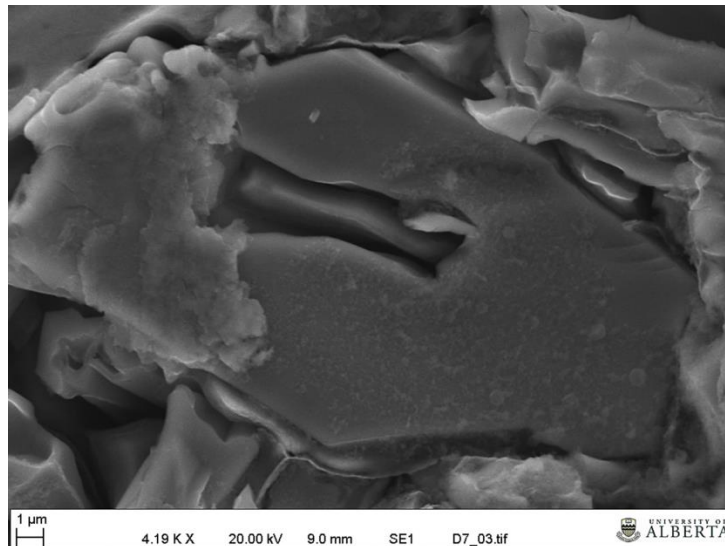
Figure 6-20: High magnification of core of primary M₇C₃

The cores were also examined using a SEM line scan method to look at the composition of the cores to determine if there is any significant difference between the austenite in the cores and the surrounding austenite and to see if there is any fluctuation in the

composition across the width of the primary carbides. Figure 6-21 and Figure 6-22 show an example of one of the line scans taken across primary carbides.
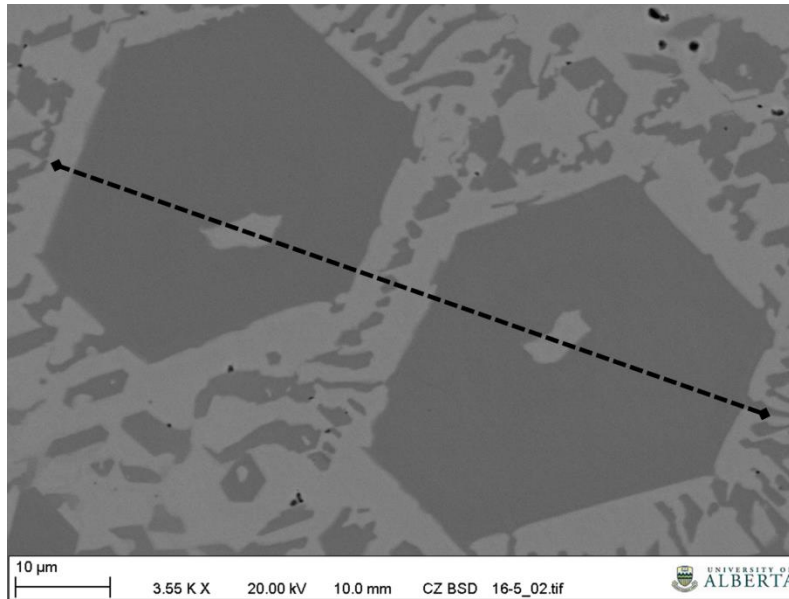
Figure 6-21: Schematic of where line scan was taken across to primary carbides and crossing cores

The drop in Cr and C can be seen as the line moves from carbide to austenite. There does not appear to be a significant difference in the composition of the austenite in the core and the austenite in the matrix.
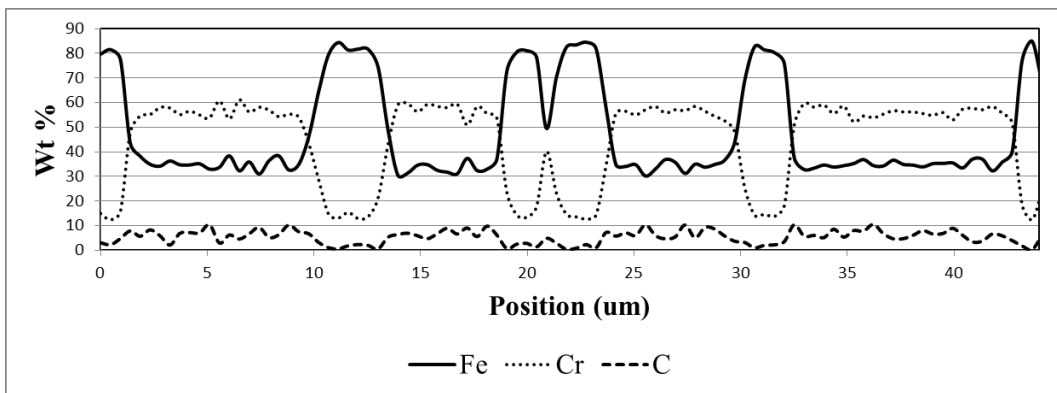
Figure 6-22: Compositions corresponding to line scan across Figure 6-21

Next the cores in the micrographs that were stacked together were examined. When flipping through them it is apparent that the areas of austenite contained in the primary carbides stay fairly constant throughout the length of the carbide as seen in Figure 6-23.
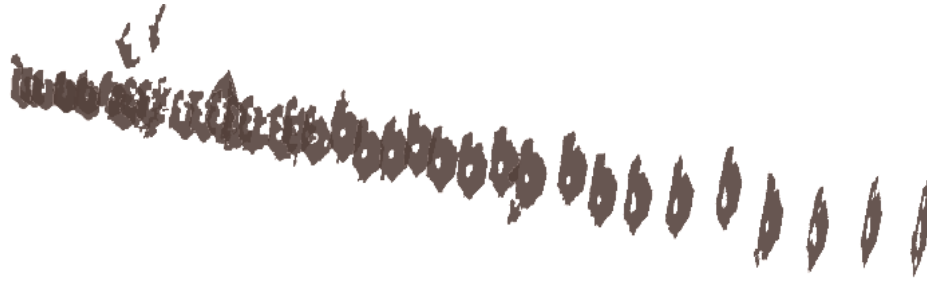
Figure 6-23: Sectioning to examine morphology of the center of the carbides

6.2.3   Discussion

After examining the effect of changing the plane of sectioning, seeing the orientation dependence in the SEM deep etch and the 3D sectioning technique it becomes clear that the so called blade and rod like morphologies are in fact just based on differences in sectioning. The two are in fact long hexagonal rods that have been sectioned differently as previously hypothesised [21, 55-57].

The cored structure of the carbides is not as clear, when examining them in deep etched samples they appear as though the centers do not continue through the length of the carbides. However, inspecting the layered sections the inner cores do appear to be constant throughout the length of the vast majority of the carbides. The analysis of the composition of the cores showed that there is not a significant difference between them and the austenite surrounding the carbides. Since the composition of these two are the same it may be possible that the cores are forming in a similar manner to the halos. If this is the case it would indicate that the austenite may be solidifying last as the carbides are growing inwards.

6.3.   Banded Structure of SAW CCOs

To properly engineer a solution to the issue of overlays containing more than just a hypereutectic microstructure a reason for the banding must be determined. The compositional and microstructural changes across the height of the overlays are examined using a variety of techniques. The hardness and the microstructure across the width of the weld were examined to determine if segregation occurs along the height and width of the welds.

6.3.1 *Segregation in samples along the height*

To examine the change in composition from the top to the bottom two different samples were examined using a variety of techniques in order to ensure accurate readings. Firstly an old 6.35mm on 6.35mm sample was examined which was created with identical settings to the base sample with the exception of a decreased CTWD of 19.05 mm. It was chosen because it clearly portrays three distinct microstructures. The second sample examined was the base sample which was has an almost entirely hypereutectic microstructure other than immediately adjacent to the fusion line. This was chosen as the second sample in order to see if even when there is predominately one type of microstructure present if there are differences found through the height of the welds.

 The methodology to determine the composition differences was refined throughout the research. The first attempt to look at the role of changing composition was done using SEM EDX looking at the old 6.35mm on 6.35mm and choosing 5 small points where the microstructure was different to see if the microstructural changes were based on composition. The large rice crispies were avoided to avoid skewing the results; the results are shown in the Appendix B. It is clear there is a difference between the composition where hypereutectic microstructure is present and hypoeutectic microstructure is present. There was no clear reason for a difference in composition found between a few of the points in the hypereutectic microstructure. It was then decided to look at more areas from top to bottom to get an idea of how the composition was changing in an attempt to determine if it was abrupt, linear, or exponential etc. The areas where the composition was taken from are marked out with the blocks in Figure 6-24.
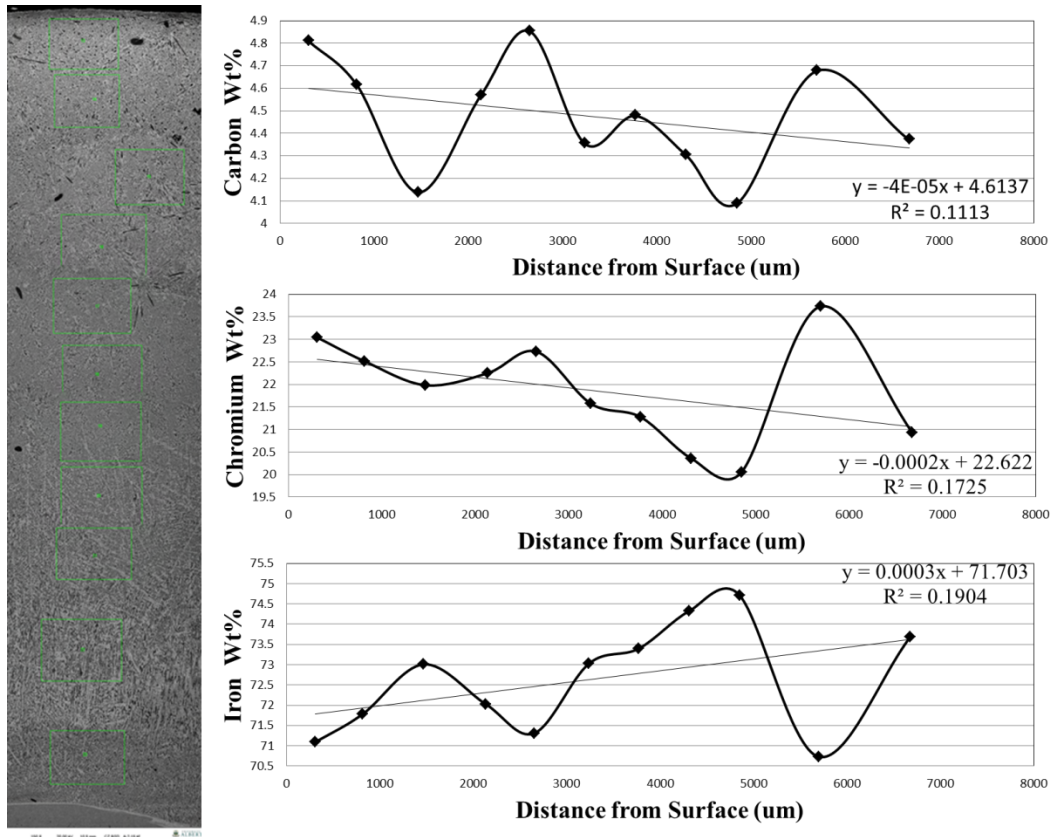
Figure 6-24: EDX results from 11 points taken across old 6.35 mm on 6.35 mm

There appeared to be trends that carbon and chromium were decreasing and iron increasing towards the bottom. This is what would be expected since the microstructure does change from hypereutectic at the top to hypoeutectic at the bottom [59]. There was a lot of scatter in the data with sudden drops and increases in the data. Numerous things could have been caused the spikes, but the correspondence of changes of chromium and carbon changing at one point with iron changing in the opposite direction should indicate that these areas do have more or less carbides than corresponding areas around them. There is still not a huge amount of change throughout the samples as the range of carbon, chromium and iron vary from 4.09 to 4.85, 20.36 to 23.7, and 70.73 to 74.71 respectively. The R^2 values are for the lines of best fit in the same order were 0.1113, 0.1725, and 0.1904.

Since the trends were still not clear, composition differences were measured along another old 6.35mm on 6.35mm sample to see if the trends are scatter or real. This time the areas where EDX analysis was performed were slightly overlapped with the results shown in Figure 6-25. The trend was again that chromium and carbon decrease from the

103

top surface while iron increases towards the bottom of the welds. This time the lines of best fit matched much better for Cr and Fe with R^2 values of 0.8798 and 0.8808 respectively. The R^2 value for carbon was still very low at 0.3201. Figure 6-25 once again shows the microstructure with the points labeled on it to the far left of the figure. A larger version of the picture can be seen in the appendix C. Figure 6-25 also shows enlarged areas of the microstructure showing a hypereutectic microstructure at the top, eutectic at the middle and hypoeutectic at the bottom of the weld.
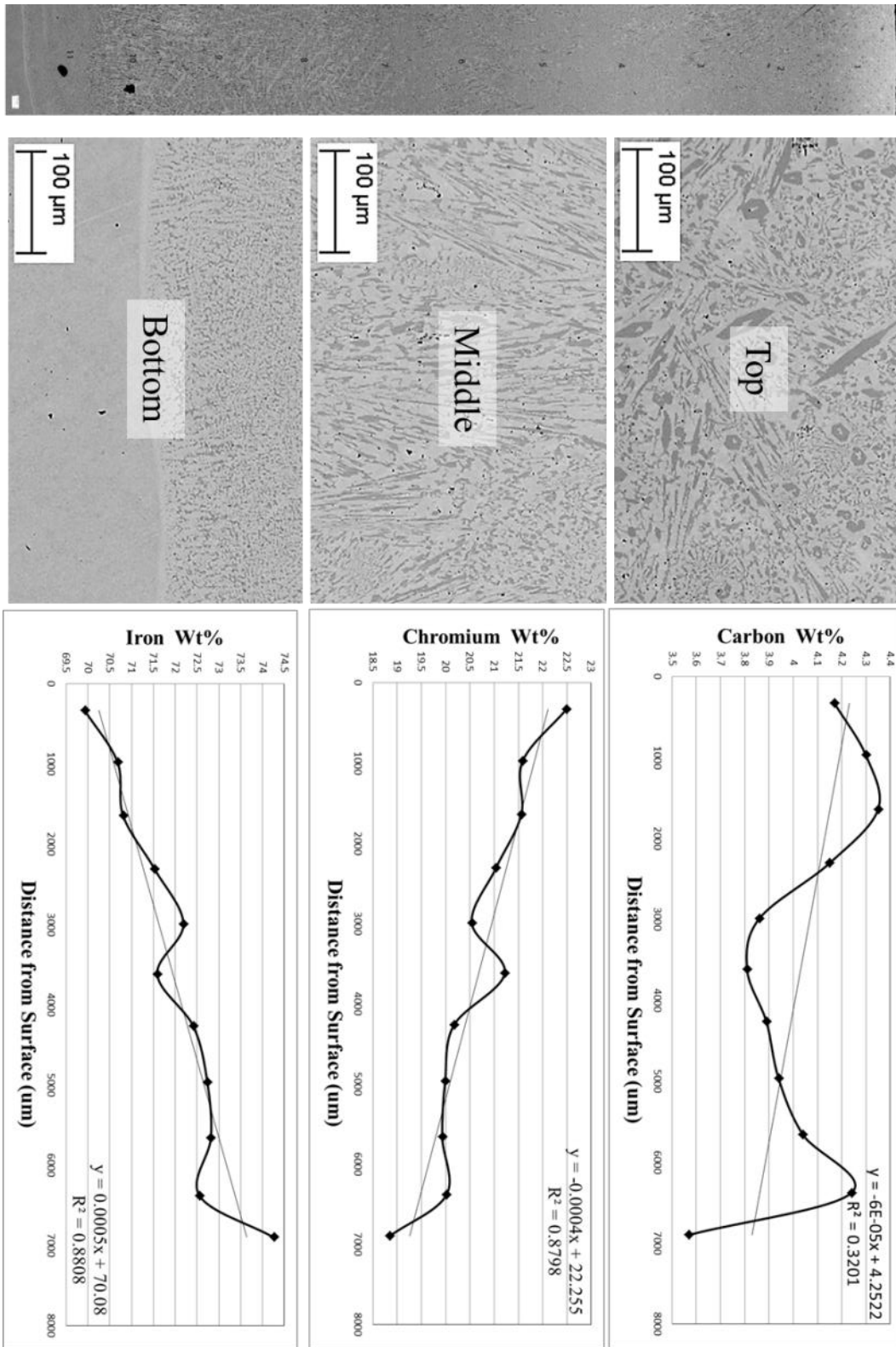
Figure 6-25: EDX results from 11 points taken across old 6.35mm on 6.35mm with overlap of areas along with overall microstructure top to bottom and enlargements of top, middle and bottom of microstructure

105

SEM line scans were also employed in case using more sampling points would indicate something that does not show up with bulk areas. The line scans showed a lot of scatter because its resolution is approx. 1 um so it can pick up individual phases leading to a lot of high readings for C and Cr where there were carbides and low Cr and C readings where there was austenite as seen in Figure 6-26. Because of the large scatter in the line scans they did not shed any more light on the cause of the composition gradient.
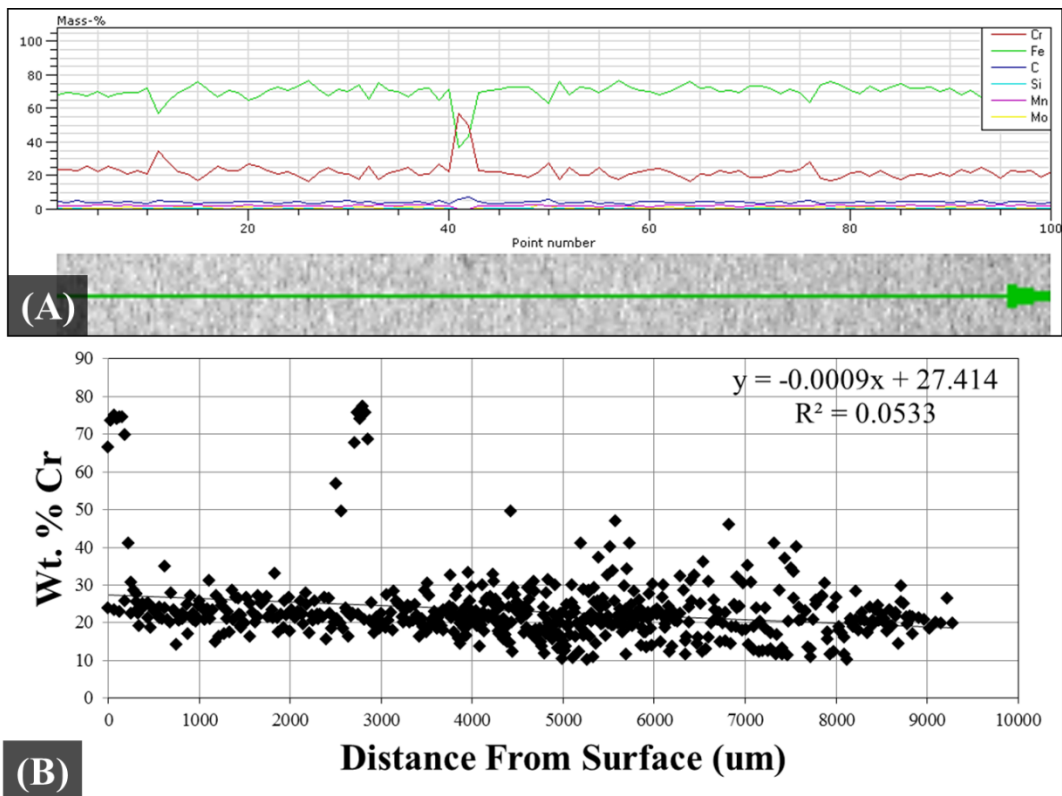
Figure 6-26: Line scan of sample to determine composition gradient (A) SEM BSD and graph of composition of different particles of first half of data plotted (B) Raw composition values plotted

One of the problems with the previous techniques used to measure composition is that the areas they are measure are rather small in comparison to the actual size of a weld. Another problem with SEM analysis is difficulties with picking up correct compositions for light elements such as carbon. In order to get a more representative composition ICP OES analysis for Cr, Fe, Mn, Mo, B, P, and Si was used on samples of approximately 2 grams in size and Leco analysis for carbon and sulphur. Both the old 6.35mm on 6.35mm and the base sample were examined and compared to SEM results for the actual

pieces that were analysed. Each was then cut into small square pieces which were then sectioned from the top to the bottom into three pieces. The distance from the surface of the different samples was measured using calipers and acounting for the blade width as shown in the schematic in Figure 6-27.
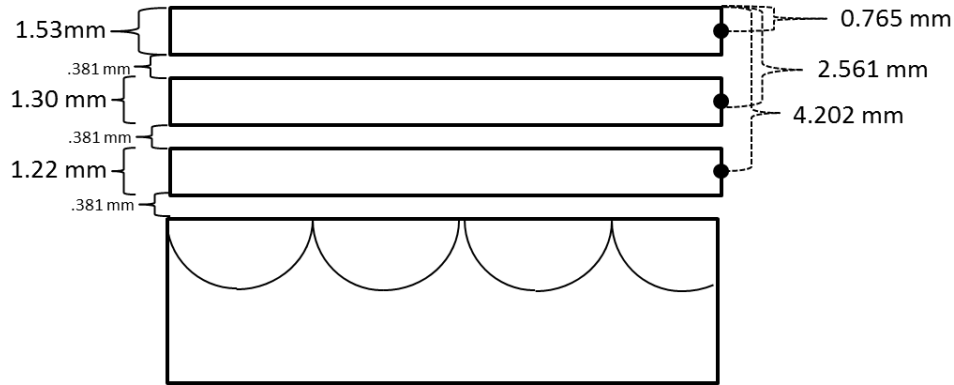
Figure 6-27: Sectioning and measuring schematic for samples that ICP was performed on. Measurements correspond to those taken for the old 6.35mm on 6.35mm sample.

These three pieces were then mounted into epoxy and polished to one micron. They were then taken to the SEM and BSD imaging and EDX analysis were performed on the side of the sections so that the microstructure through the thickness of each cut could be examined.

The samples were then taken out of the epoxy puck and broken up using a sharp punch and a hammer. The samples and the baggies were cleaned with isopropanol in order to remove any contamination. The composition measured using EDX was then compared to composition using ICP and LECO. Table 6-5 shows the difference in readings between the measuring techniques for the old 6.35mm on 6.35mm sample. The data for the base sample is given in appendix D.

Table 6-5: Comparison of SEM values to ICP and LECO for old 6.35mm on 6.35mm

	ICP (Wt. %)			SEM (Wt. %)		
Element	*Top*	*Middle*	*Bottom*	*Top*	*Middle*	*Bottom*
Chromium	26.2	23.7	22.8	23.18	22.77	22.35
Iron	69.3	74	74.1	70.42	70.90	71.10
Manganese	1.95	1.9	1.85			
Molybdenum	0.819	0.794	0.801	0.79	0.73	0.82
Boron	0.21	0.21	0.21			
Phosphorous	0.01	0.01	0.01			

Silicon	0.388	0.366	0.396	0.27	0.22	0.24
Carbon	3.17	3.02	2.82	5.34	5.38	5.48
Sulphur	<0.05	<0.05	<0.05			
Distance from surface (um)	765	2561	4202	765	2561	4202

The samples that ICP testing was performed on show that the composition analysis of SEM is not as sensitive enough to pick up elements such as manganese, boron, and phosphorous. It also showed that there was a much larger variation in chromium from top to bottom than was picked up using the SEM, and conversely much less variation in carbon than indicated using EDX analysis. Figure 6-28 shows how both the chromium and the carbon decrease towards the bottom of the weld and the microstructure decreases in primary carbides until the microstructure is eutectic in the bottom sample.
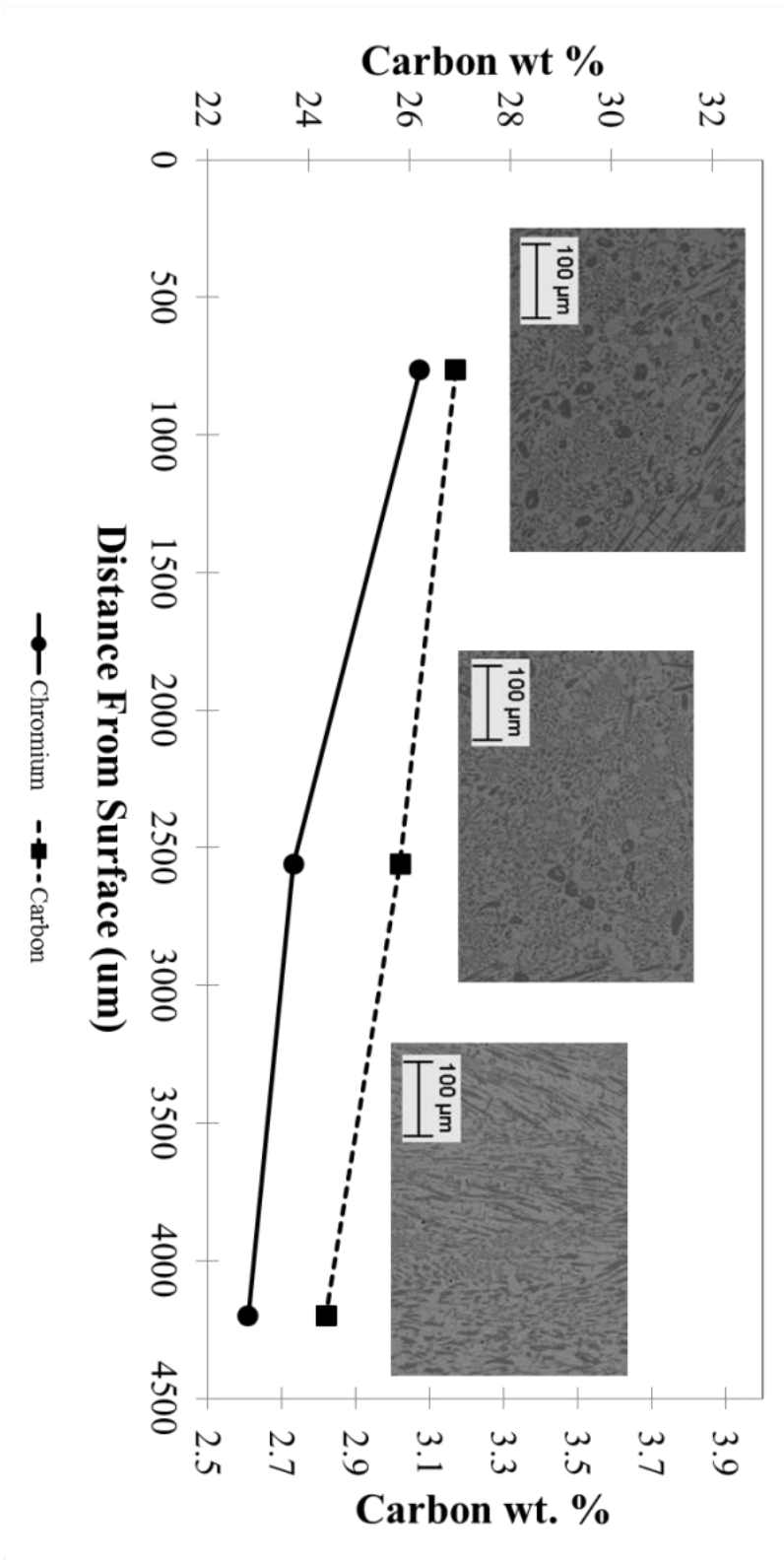
Figure 6-28: ICP results for old 6.35mm on 6.35mm with micrographs above corresponding locations

The ICP results once again indicated that there is a trend that carbon and chromium decreases and iron increases towards the bottom for both samples. The most noticeable differences in the compositions between the old and the new 6.35mm on 6.35mm are that the new sample is higher in carbon, silicon and manganese. The base sample still has a concentration difference along the height of the weld even though the microstructure is much more uniform.

6.3.2   Segregation along the width

The width of the weld beads is relatively large at 44.5mm and it has been noted that the penetration through a sample width can vary. Due to these facts the segregation along the width of the welds was also examined. The base sample was the one that was examined. Numerous longitudinal metallographic samples were made starting in the centre with spacing of 6.35mm with an extra sample taken in the middle of the overlap of two passes as shown in Figure 6-29. The sample names correspond to their distance away from the center line with samples to the left denoted by a negative distance and ones to the right a positive distance.
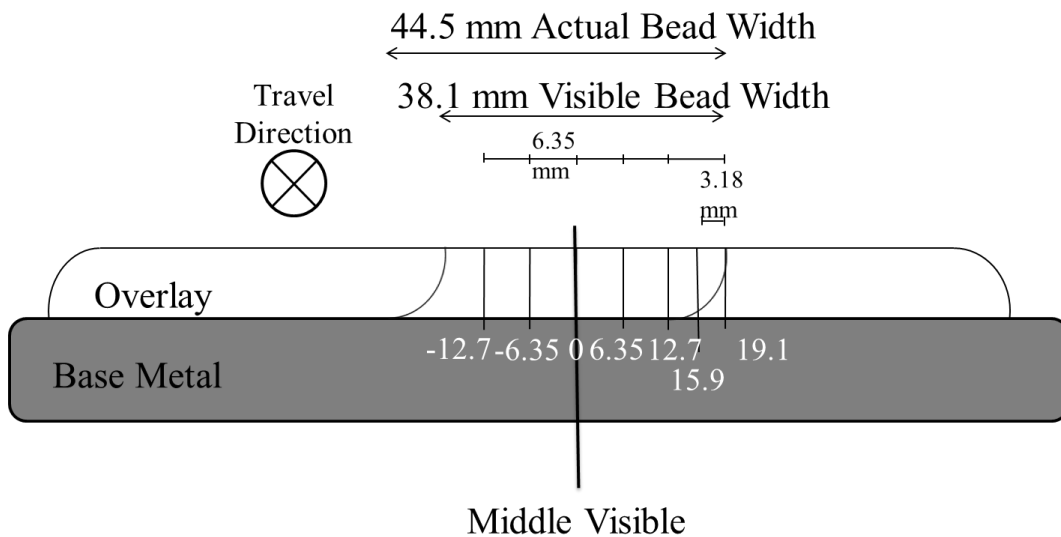
Figure 6-29: Sectioning positions for samples looking at segregation along width of overlay

The first thing examined was the microstructure along the width. It becomes apparent that the microstructure is not consistent throughout the width of the welds when examining there micrographs in Figure 6-30. There is a very hypereutectic microstructure in sample

110

taken at 0, 6.35, and 12.7 mm while the samples at -6.35 and 15.9 mm have a hypereutectic microstructure through about half of them. Lastly, the samples at -12.7 and 19.1 mm have very little primary carbides.
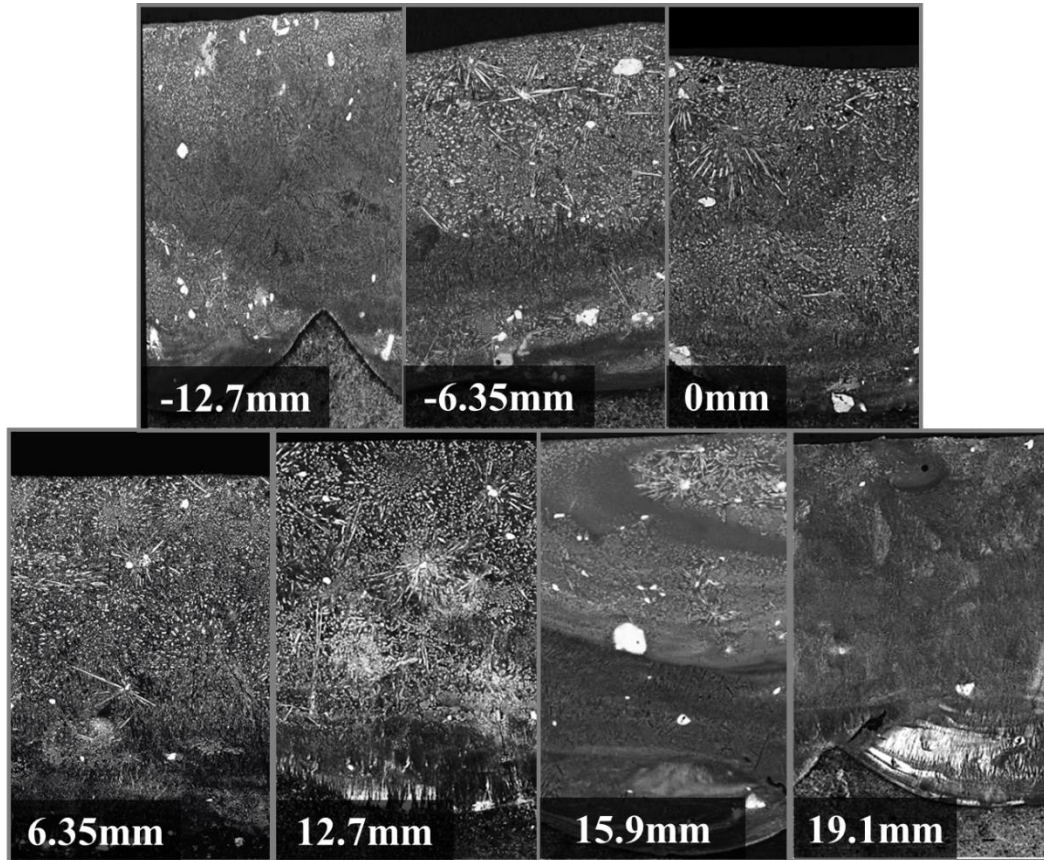
Figure 6-30: Micrographs taken from along the width of the weld with numbers corresponding to distance away from visible centre of weld bead

Hardness mapping as shown in Figure 6-31 was then done on all of the samples in order to see the effect that the changes in microstructure may have on the mechanical properties of the overlays. Figure 6-32 shows a 3d plot of the hardness across the sample that was taken at 0.25 inches from the visible centre.
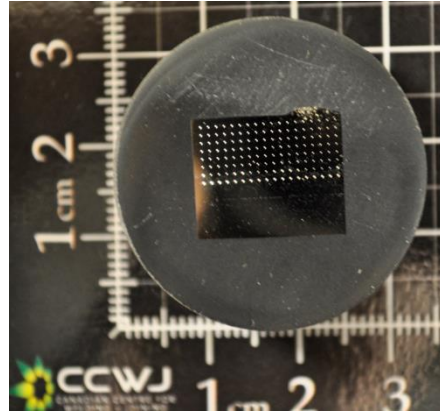
Figure 6-31: Grid of hardness measuring points on sample
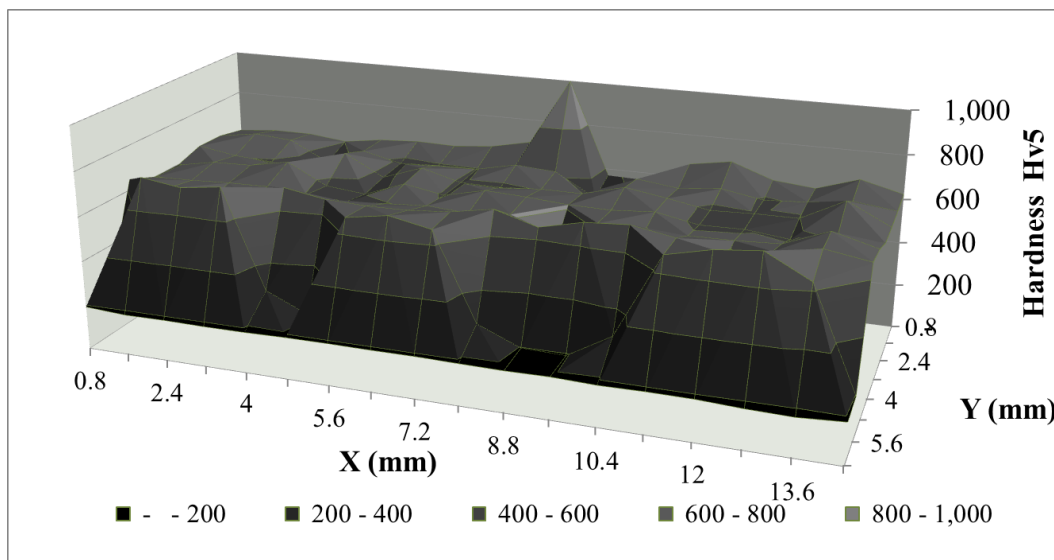
Figure 6-32: 3d hardness mapping of sample at 0.25 inches

The data can also be plotted in a more conventional method where we can compare the hardness of the alloys along the height of a sample as shown in Figure 6-33. This is fairly representative of what we see, the hardness across the different heights is more or less within a standard deviation of each other with large spread in the data around the second furthest line from the surface because some points are in the overlay and other points are in the base metal as this is approximately where the fusion line is.
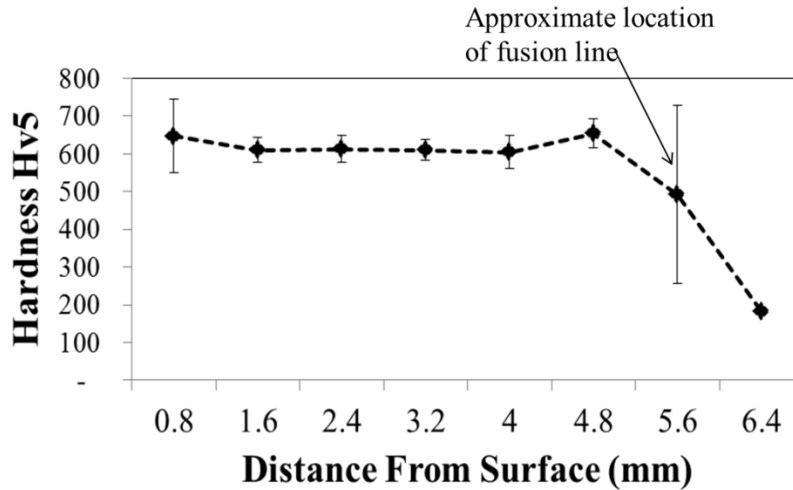
Figure 6-33: Plot of hardness at different heights in sample taken at 6.35mm

The average hardness values of the overlays were then plotted along with the micrographs and there location as shown in Figure 6-34. Any points that were fully on or partially on the large unmelted particles or the base metal were removed from the data sets. Comparing the hardness values of the sample at 12.7mm and -6.35mm which have significantly different microstructures we found no evidence to support that the means are statistically different with a 95% level of confidence. This tells us that the average hardness of the overlays does not vary through the width of the welds.
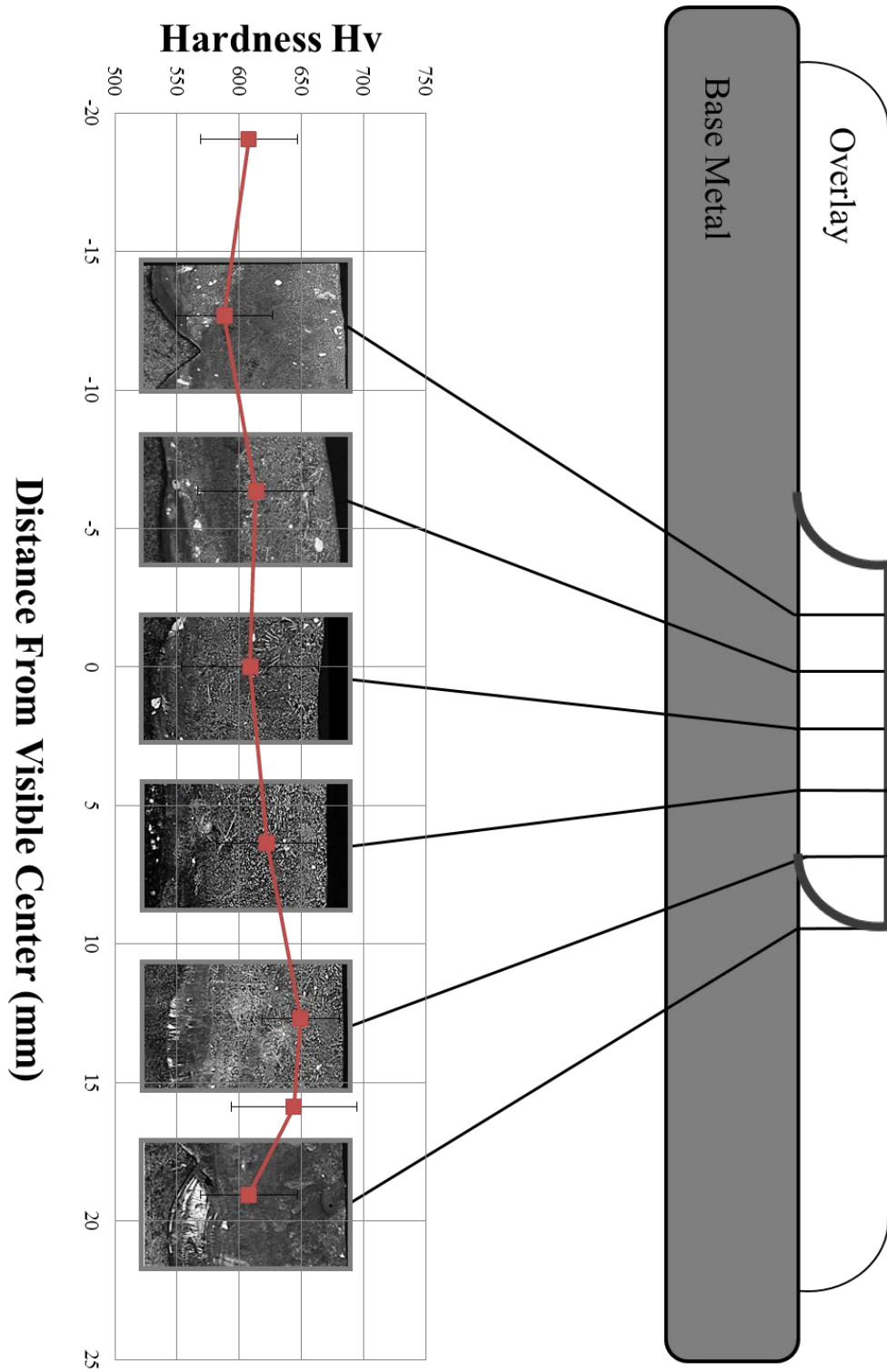
Figure 6-34: Plot of average hardness across the width of the weld superimposed with their locations and micrographs

This lack of clear differences in the hardness could be attributed to the fact that there is such a wide range of microstructure throughout the individual overlays causing large spreads in the hardness data. To look at this possibility the hardness across two samples with very different amounts of primary carbides were compared. The height at which the hardness testing was done at was 4 mm down from the surface and the results are shown in Figure 6-35. Once again no evidence was found to support that the means are statistically different with a 95% level of confidence.
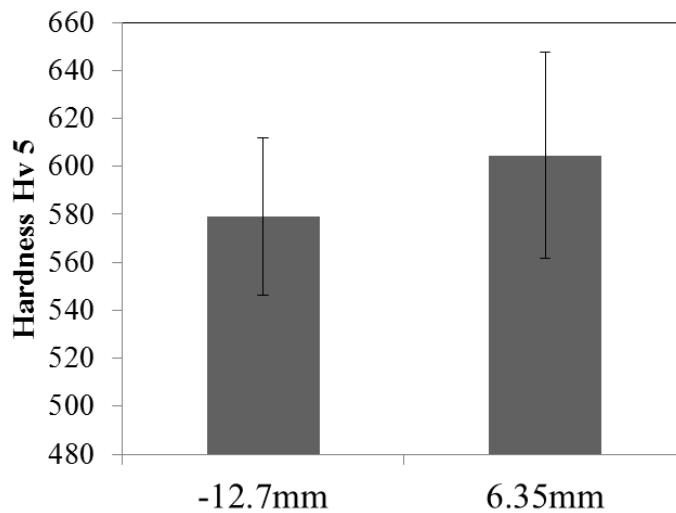
Figure 6-35: Comparison of hardness along two samples 4mm from top surface

6.3.3   Discussion

Examining the composition along the height of the weld using the SEM EDX analysis of bulk points, SEM EDX line scanning, and ICP analysis a few conclusions can be made. The ICP analysis showed that while the trends are mostly correct for the SEM samples, care must be taken if EDX analysis is the main measurement technique because of lack of sensitivity picking up elements such as Mn, B, and P. The fact that the area of analysis for EDX is much smaller than ICP and LECO is another concern when relying on the SEM data. Both analysis methods showed that the difference in microstructure that can occur throughout the height of the weld pool is in fact caused by differences in the composition. They also both showed that the trends are for chromium and carbon to decrease towards the bottom of weld pool while Fe increases. The changes in composition for Fe and Cr were much more significant than the differences in carbon which could possibly be because C is a fast diffuser. The differences in composition may

be caused by dilution amounts varying through the height of the weld bead because the base plate is where the excess Fe is coming from. However Mo, Mn, Bo, and Si do not appear to follow any particular pattern in their distribution through the height of the weld pool. While this does not conclusively rule out that dilution or mixing is not the cause the fact that they are fairly uniform throughout indicates that the weld pool may start out at a uniform composition. It is possible that through either diffusion or segregation during solidification the other elements are segregated. The other side could be argued that these atoms are ones diffusing after solidification [63]. Taking this all into consideration it is not clear what causes the segregation of the elements along the height of the bead but it is conclusive that it does occur and that in order to avoid a bottom weld that is hypoeutectic the segregation should be kept to a minimum or an overall increase in the amount of C and Cr in the alloy can help ensure that the microstructure is hypereutectic throughout.

The experiments examining the width of the welds showed that segregation is also occurring throughout the width. The fact that the volume fraction of hypereutectic microstructure is decreasing at the sides of the welds may indicate that these areas will not have as good wear resistance as in the center [59]. Interestingly though no statistical difference was found in the hardness across the profile and while, volume fraction primary carbides is normally a better predictor of wear resistance it cannot be dismissed that hardness can also correlate to wear resistance.

6.4.   Effect of Cooling Rate

Previous work has shown in that the cooling rates (CR) of CCOs have an effect on the microstructure of overlays applied using shielded metal arc welding [39]. This work will look at how the cooling rates affect the welds that are made using SAW technique and its effects on the volume fraction of carbides, size of carbides, and dilution amounts.

6.4.1   Effect of preheats

There are a number of ways to change the CR in welding such as, changing the heat input, preheats, and joint configuration. For the research carried out it was decided that the easiest way to change the heat input was through the use of pre-heats. The test rig as seen previously was made so that a torch could be used to preheat the "gantry plate" and the baseplate that was being welded. For all the experiments the gantry plate and the base plate were preheated to above the desired temperature and then left to cool to the desired

pre-heat. This allowed for the temperature to become homogenous throughout the gantry and base plates.

The results of changing preheat on the microstructure is shown in Table 6-6. Interestingly the amount of dilution did not appear to change significantly thorough the different preheats. This is advantageous because it should mean that the dilution effect on composition will play a minor role in the results of the experiments.

Table 6-6: Microstructural and dilution measurements showing effect of preheat

Preheat	Total VF Carbide	VF Hypereutectic	VF Primary M7C3	Average Primary Size (um)	Dilution
298^0 K	26.99%	30.40%	1.69%	389	27%
323^0 K	23.59%	31.24%	1.84%	427	25%
373^0 K	25.35%	46.12%	5.02%	542	26%
423^0 K	24.54%	19.89%	0.66%	252	25%

The total VF of the carbides remained relatively constant through the samples but there was a large range in the amount of hypereutectic microstructure, VF M_7C_3, and Primary M_7C_3 size.

In order to ensure that the preheats were changing the cooling rates of the alloys the welds were harpooned with thermocouples to get cooling measurements. This gave us the curves shown in Figure 6-36. The temperature measurements are for the samples that are discussed in section 6.4.1 with the exception of the 373^0K, 298^0K (2), and 253^0K that were made during other attempts looking at the effect of preheat where the composition was not high enough in Cr and C to produce a hypereutectic microstructure. The curve for the 323^0 K is not complete because of the thermocouple failed to continue to take measurements after a certain time period.
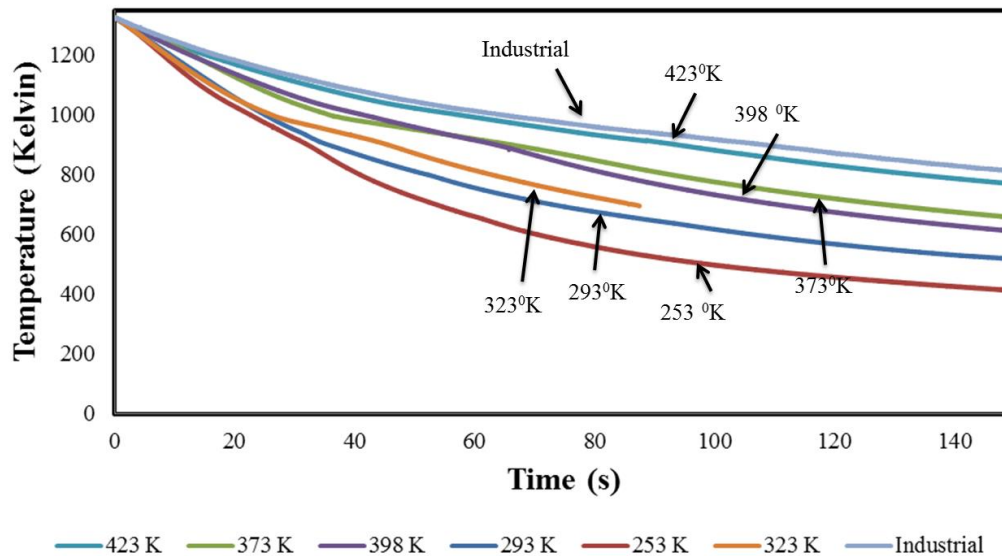
Figure 6-36: cooling curves from plunged thermocouples

The curves show that preheats have an effect on the cooling rate of the overlays. There is a fairly clear trend that the cooling rates increase as the preheat decreases with the exception of the 398 ^{0}K preheat cooling curve falls lower than the 373 ^{0}K cooling curve.

6.4.2   Base Sample Replication

In the preheat group of welds the 323^{0}K   weld should match the industrial sample, because it was run at all the same settings as the base sample and the preheat falls in the range of the interpass temperatures of the industrial produced sample. When comparing the properties for the two samples in Table 6-7 they are not close to being comparable. The VF of hypereutectic is 93% for the base sample yet only 31% for the 323^{0}K sample. The VF primaries are also very different at 11.53% and 1.84 % respectively. One factor may be that when you examine the cooling rate curves for the two samples you find that the two are in fact very different. The cooling rate of the industrially produced sample is slower than even the sample with the 423 ^{0}K   preheat as shown in Figure 6-36. Examining the values for in Table 6-7 the most telling difference between the samples is the dilution amounts. The dilution is about half as much for the base sample as it is for the other samples made during the cooling rate experiments. This difference explains

why there the VF of hypereutectic microstructure and VF primary M_7C_3 carbides because the composition of C and Cr will be much higher in the base sample.

Table 6-7: Comparison of samples to base sample

Sample	Total VF Carbide	VF Hypereutectic	VF Primary M_7C_3	Average Primary Size (um)	Dilution
323 ^{0}K	23.59%	31.24%	1.84%	427	25%
Base	22.14%	93.26%	11.53%	512	12.68%
373^{0}K	25.35%	46.12%	5.02%	542	26%

6.4.3   Discussion

The effect of preheats and cooling rates on CCOs was inconclusive. The one thing that it did show was that preheat does not have a huge effect on the dilution. Examining the three lowest preheats there was a small indication that the VF of hyper eutectic and VF of primary carbides may increase with slower cooling rates. The size of the carbides also appeared to increase with slower cooling rates but when you compare the 423^0 K sample we find that the trends are reversed. This may be caused by a difference in the composition of the 423^0 K sample. The sample should have been roughly the same compositions the others but unlike the other samples that were majority eutectic microstructure with most the remaining being a hypereutectic microstructure, the 423^0 K sample had majority hypoeutectic with a small amount of eutectic and hypereutectic. The cause of this is unclear; there could have been a problem with the powder feeder or numerous other factors. The differences in the cooling rates between the two different samples measured at 298^0 K are similarly unclear and could have been caused by numerous factors. To solve this problem more weld pool temperature measurements should be taken. The problem with this is that the success rate of the harpoons is probably less than 20% which makes the number of samples needed to get reliable results huge and unpractical. One solution to this may be to design a rig attached to the welding head that mechanical spears the weld pool at a set distance back from the welding head. This would give the operator more precise control of the harpoons and solve the problems that cause the thermocouples to fail when they are either speared to far back from the welding torch so they don't come in touch with the molten pool or too close to the welding torch where they melt too much and fail to get readings.

Another thing that the cooling rate experiments were able to show conclusively is that the samples made in the lab were not effective at replicating the industrial sample. Not only was the measured cooling rate of the industrial sample slower than all of the preheats, but the microstructural measurements were also significantly different. The reason for the difference in cooling rate can most likely be explained by the scale difference between the two setups and single pass welding vs. multipass welding effects. While the preheats of the base plates were the same the passes that had been welded previously in the industrial sample may affect the cooling rate significantly, by changing the size of the plate immediately next to the weld bead and It could also possibly be much hotter than the temperature of the base metal which would decrease the cooling rate. However, the difference in the cooling rate does not explain the huge differences in dilution and microstructure between the lab and industrially samples. The most likely explanation is that there was a break down in control at one of the setups. To solve this dilemma more samples should be compared that were made using the base sample settings in the lab and industrially but at different times and locations to determine if these results of either the lab or the industrial samples do not match what is representative.

6.5.   Effect of SAW Processes Parameters

The following section looks at process parameters of SAW and their effect on the microstructure and properties of CCOs. Specifically the effects of balance in AC welding and contact tip to work piece distance on CV welding are examined. The effect of these variables is fairly well known but no research has been done concerning their effect on SAW CCOs that are produced using a weaving technique [62, 85, 86]. For the large majority of applications of the SAW process has remained relatively unchanged since the original implementation of the process. Meaning direct current electrode positive (DC+) is still one of the most commonly used settings for SAW. In direct current (DC) welding the flow of electrons only travels in one direction, in the case of DC+ the electrons flow from the work piece to the electrode consumable while in DC- electrons flow from the electrode to the work piece. The properties of the welds produced using the two methods differ greatly. DC+ polarity produces a higher level of penetration for a given wire feed speed (WFS) in comparison to direct current electrode negative (DC-) when welding in constant voltage (CV). On the other hand DC- has a higher deposition rate than DC+ for a constant current (CC) and a given electrode diameter it. In recent years there have been a number of advancements to the SAW process with the advent of inverter based

hardware and software control that has increased the versatility of SAW. These technologies have allowed for the ability to weld using variable wave shapes with alternating current (AC) [86].

In AC welding it is possible to use a combination of the DC- and DC + where the machine switches between the two polarities. This gives the advantage of the higher deposition rate during DC- and the increased stability of DC+. AC welding can be performed using either CC or CV. During CC welding voltage and current are kept constant while the WFS varies in order to maintain the other welding parameters. When using CV the WFS and the voltage are set, this means that in order to keep these operating variables constant the machine varies the current. [85]. When using AC welding in addition to the traditional parameters such as voltage and WFS, other variables that relate to the shape of the waveform can also be controlled.

The parameters related to the shape of AC waves that can be controlled are the balance, offset and frequency. This research looks solely at the effect of controlling the balance. The balance is typically given as a percent (%), where the % balance is the percent of time the arc spends in DC+. Figure 6-37 shows how changing the balance effects penetration. [86]
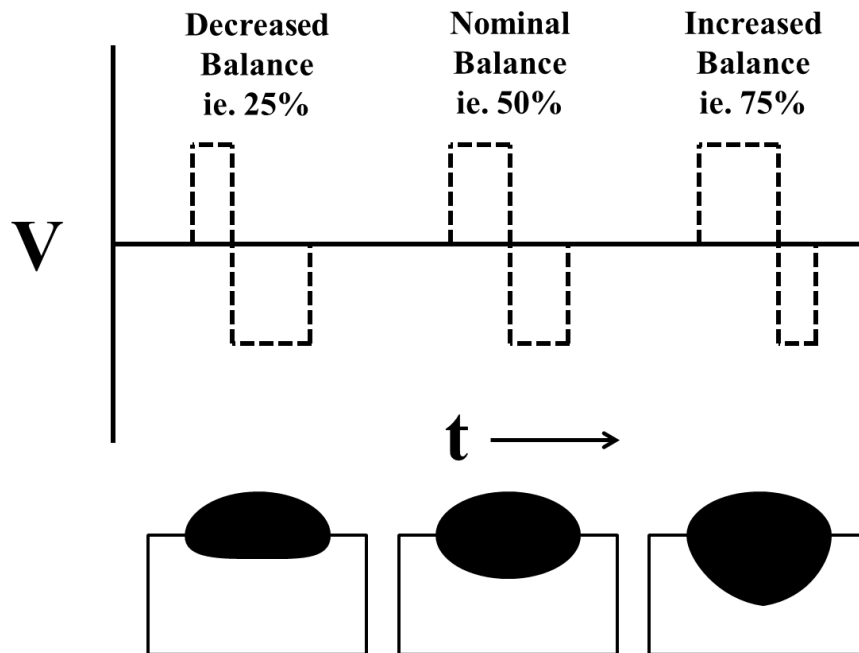
Figure 6-37: Effect of balance on weld profiles

121

6.5.1   Constant Voltage Alternating Current Welding

When examining the effect of balance on the production of CCOs the welding was done in CV in order to control the WFS and keep the ratio of wire to powder constant through all the welds. The offset was not adjusted and the frequency was kept constant at 45 Hz. six samples were produced keeping all of the settings the same with the exception of the balance. The respective balance setting of the samples is listed in Table 6-8.

Table 6-8: Balance settings of AC weld samples

Sample	Balance
A	50
B	55
C	60
D	65
E	70
F	75

By keeping all of the settings the same we should be able to eliminate their influence on the resulting microstructure in order to determine the effect of balance.

Figure 6-38 is a good example of how the profiles vary when cut transversely across the samples. These cross sections show that the penetration is increasing throughout the samples as the balance increases. The actual dilution measurements were taken from the longitudinal sections and are tabulated in Table 6-9 along with the heat input calculations.
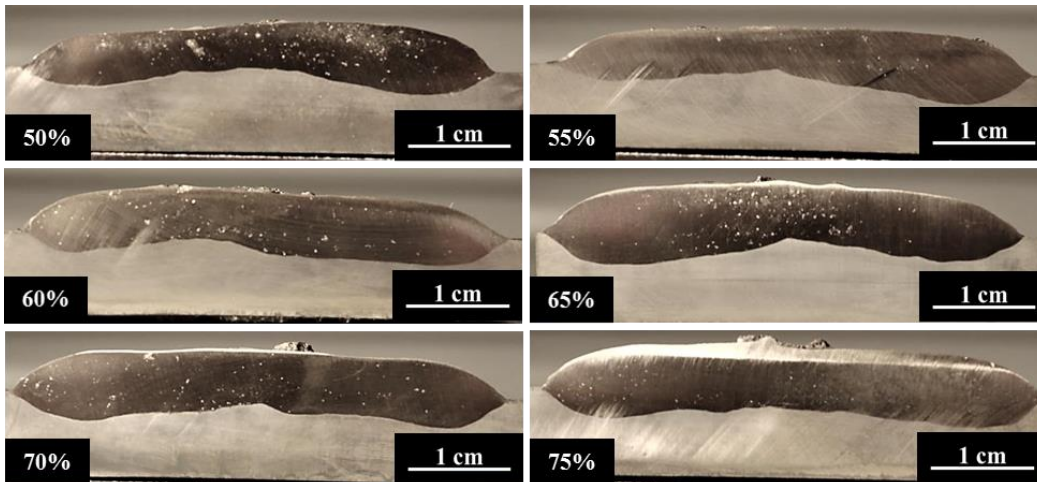
Figure 6-38: Weld bead profile along the transverse of the weld bead

Table 6-9: Heat input and dilution of balance samples

Sample	Balance (%)	Dilution center (%)	Dilution side (%)	Heat Input (kJ/mm)
A	50	3.7	34.0	3.82
B	55	4.8	32.8	3.96
C	60	19.7	47.5	4.00
D	65	18.7	38.6	4.06
E	70	25.7	41.3	4.23
F	75	31.1	41.4	4.30

Figure 6-39 shows that the trend is for the heat input and dilution to increase as the balance increases. The exception is at 60% balance which has high dilution amounts.
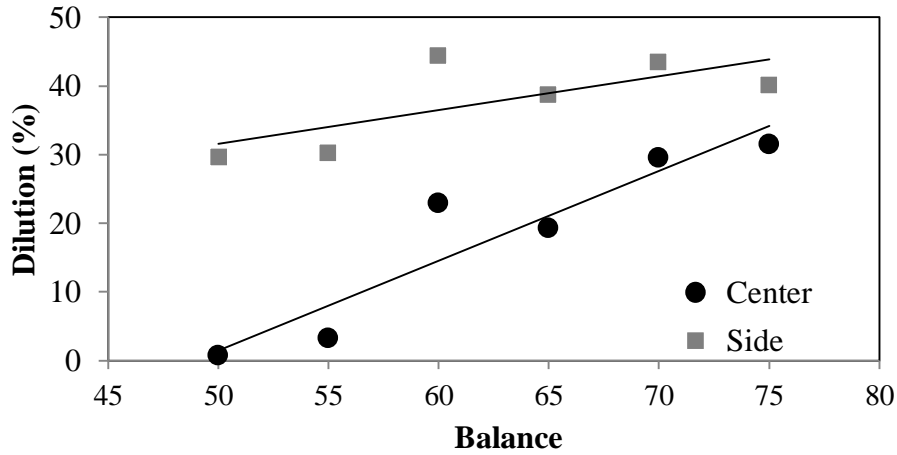
Figure 6-39: Dilution Graph

Figure 6-40 shows how the microstructure changes throughout the height of the samples. We can see how the amount of hypereutectic microstructure increases as the balance decreases.
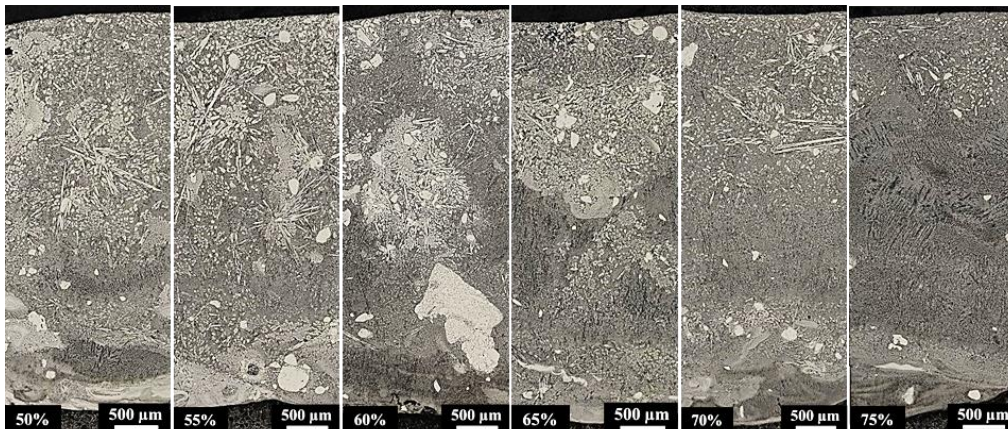
Figure 6-40: Overview micrographs of the full height of AC welds

The overview micrographs are a good indication to see how the overall microstructure is changing but in order to get a better idea of how the hypereutectic microstructure is changing we the microstructure was examined at higher magnifications such as in Figure 6-41.
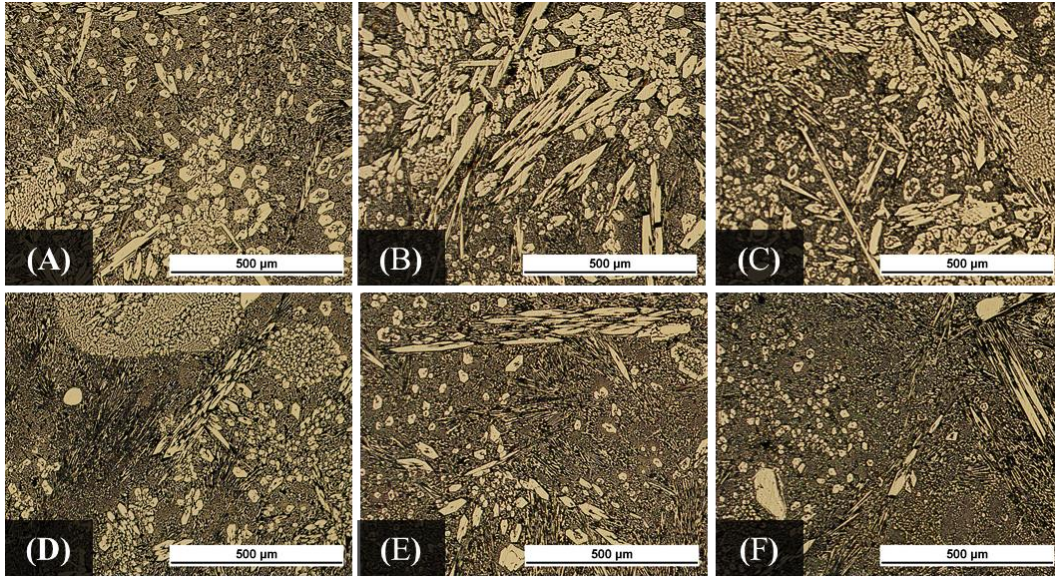
Figure 6-41: High magnification of hypereutectic microstructure of AC welding samples (A) 50% balance (B) 55% balance (C) 60% balance (D) 65% balance (E) 70% balance (F) 75% balance

The measured volume fraction (VF) of hypereutectic microstructure, total carbide VF, VF of primary M_7C_3 carbide and the average primary M_7C_3 size are given in Table 6-10 and Figure 6-42.

Table 6-10: Microstructural characterization measurements of carbides

Balance	Total VF Carbide	VF Hypereutectic	VF Primary M7C3	Average Primary Size (um^2)
50%	45.81%	100.00%	21%	796
55%	42.65%	100.00%	20%	616
60%	32.76%	100.00%	18%	538
65%	37.81%	84.76%	14%	460
70%	31.44%	75.64%	9%	446
75%	21.01%	40.33%	3%	413

There are some trends that develop when examining the carbide measurements. The amount of microstructure that is hypereutectic goes from under half to a 100% as the

balance reaches 50%. The volume fraction and average primary carbide size also increases as the balance decreases.
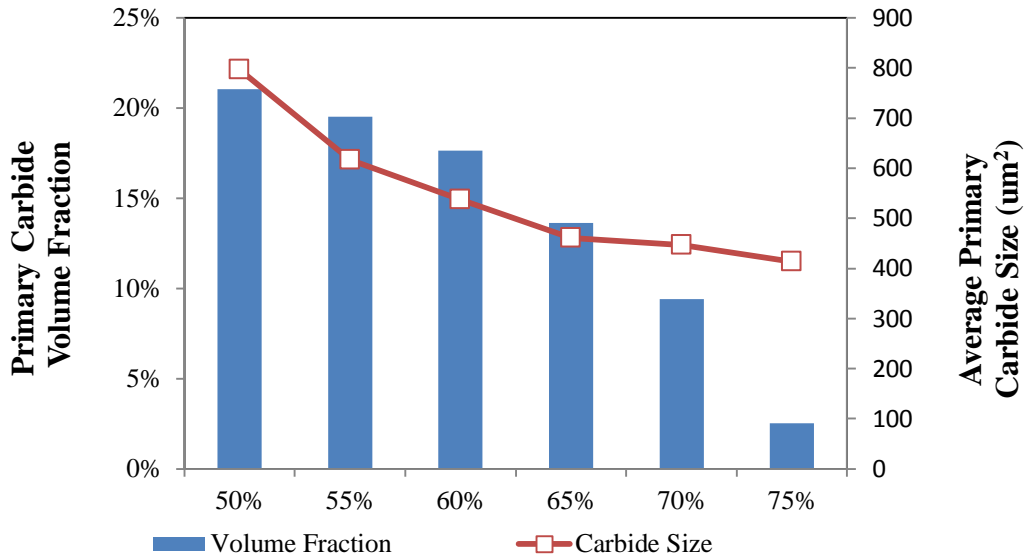
Figure 6-42: Primary carbide volume fraction and average primary carbide size

6.5.2 Effect of Contact Tip to Work piece Distance

Another welding parameter that was examined was the effect of contact tip to work piece distance. Four different CTWDs were examined starting at 25.4mm and increasing by 3.75mm until reaching the CTWD of 34.9 mm. The chemical analysis and mechanical properties of the welds are given in Table 6-11. These welds were performed by the industrial partner and the results other than the penetration were performed by an external lab. The penetration was measured by taking the average of a number of points measuring the height of the fusion line rather than using the volume measurement technique described in the procedure section.

Table 6-11: Properties of varying contact tip to work piece distance

CTWD (mm)	ICP Results (wt. %)			Penetration (mm)	G65 Testing		Hardness	
	Cr	Fe	C		Surface	75% depth	Rockwell	Vickers
25.4	23.6	67.3	3.03	2.18	0.175	0.189	55	563
28.6	22.1	72.3	3.03	2.10	0.16	0.145	53	535
31.8	26.9	68.1	3.63	1.58	0.122	0.132	55	578
34.9	27.5	65.7	3.51	1.73	0.152	0.177	54	580

126

There is not any clear trend to make from the data as the CTWD for the 34.9 mm sample appear to deviate off of any that could be seen in the first three samples.

6.5.3   Discussion

The work on CTWD showed that for the most part the amount of penetration decreased as CTWD increased, which will lead to a decrease in the dilution in the weld metal [62]. There are no clear definitive trends but the wear resistance does appear to improve, the amount of C and Cr increases, and penetration decreases for the two longest CTWDs. The results for the AC welds are much more definitive.

During AC welding the dilution and the heat input both decreased significantly as the balance decreases. This occurred because as more time is spent in DC- the average current decreases because less energy is needed to melt the wire in DC- compared to DC+. Probably the largest effect that this has on the microstructure is that the decrease in dilution leads to an increase in the amount of alloying elements in the weld metal. Increasing carbon and chromium should cause the amount of primary carbides to increase, which is exactly what we see occurring [21, 30, 43]. This increase in primary carbides should increase the wear properties of the chromium carbide overlays [12, 21]. Increasing the balance also had the effect of increasing the volume fraction of hypereutectic microstructure which should make the wear resistance more uniform throughout the height of the overlays.

One trend that was also seen in the AC welds was the decrease in the size of the primary carbides. This opposite to what would be expected for either welds that are cooling faster as is the case with less HI or overlays with more carbon [21, 39]. This shows that there is a secondary factor that may actually play a larger role in the growth of the primary carbides than the cooling rate and carbon amounts. Alloying elements that increase when the dilution decreases could also play a role since Mo and Si have both been found to reduce the rate of carbide precipitation which could possibly lead to the larger carbides [19, 35]. Both increasing the CTWD and decreasing the balance during AC welding could potentially increase the wear properties of overlays because they decrease the amount of dilution. This will increase the amount of alloying elements leading to an increase volume fraction of primary carbides positively affecting the wear resistance.

7.   Production of CCOs Using Different Welding Processes

There are a large number of different processes used for the application of overlays; everything from Oxy Fuel welding to Laser Welding. This thesis examines four different processes; PTAW, SAW, GMAW, and LBW. They all have their own inherent strengths and weaknesses. SAW is good for welding large areas and needs low operator skill. A downside to SAW is it is not suitable for small parts and can only be applied in the 1G position making it difficult to impossible to work on complicated geometries. GMAW on the other hand is very versatile and can often be employed on complex shapes. PTAW can produce very high quality weld deposits with good control over dilution and surface finish but, limitations to PTAW include the inability to weld out of 1G position and relatively high equipment costs. LBW also produces very high quality welds but with some of the highest equipment costs [17]. The differences between GMAW, PTAW, and LBW CCOs will be discussed in depth in the following section. SAW will not be examined in depth because the bulk of the previous portions of this thesis have already discussed it in depth. However, values from some of the SAW welds will be included as comparisons in some of the tables.

7.1.   Weld Appearance

While often superficial the weld appearance is still of importance, how the overlays look and differences in how they are applied may factor into which processes are used for certain applications. The appearance of CCO's varies largely between the different processes. Figure 7-1, Figure 7-2, Figure 7-3, and Figure 7-4 show the weld bead appearances for GMAW, LBW, PTAW and SAW, CCO's respectively.

Figure 7-1 Weld bead appearance of double-layered GMAW chromium carbide overlay GMAW1
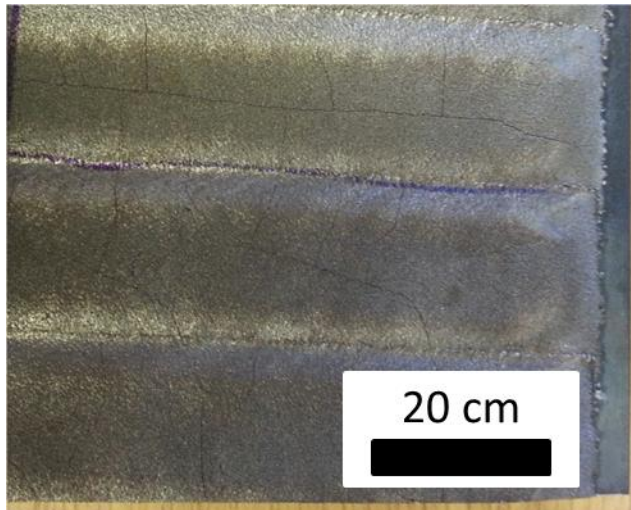
Figure 7-2: Weld bead appearance of four passes of laser cladding CCO's LW1

Figure 7-3: Weld bead appearance of single pass PTAW CCO at 180 A

Figure 7-4: Weld appearance of SAW 100C CCO

The weld bead appearances vary widely for the different processes. GMAW appears quite different because the weld beads are placed down as stringers, while with both PTAW and SAW processes the beads are laid down while the torch is oscillating back and forth to increase the width of the beads. The laser welds are produced using a square beam which is why it does not have the appearance of stringer beads. These differences

in how the overlays are applied can also be seen when examining the transverse cross sections in Figure 7-5. The cross sections show that close to the edges of both the SAW welds and the PTAW there are higher amounts of penetration because of the dwell of the torch at the end of the beads during the weave functions. The LBWs have a relatively flat penetration profile and the GMAWs have many scallops because of the multiple stringer beads. The cross sections also make it apparent that the penetration ranges widely across the processes with the most to least being SAW, GMAW, PTAW, and LBW.
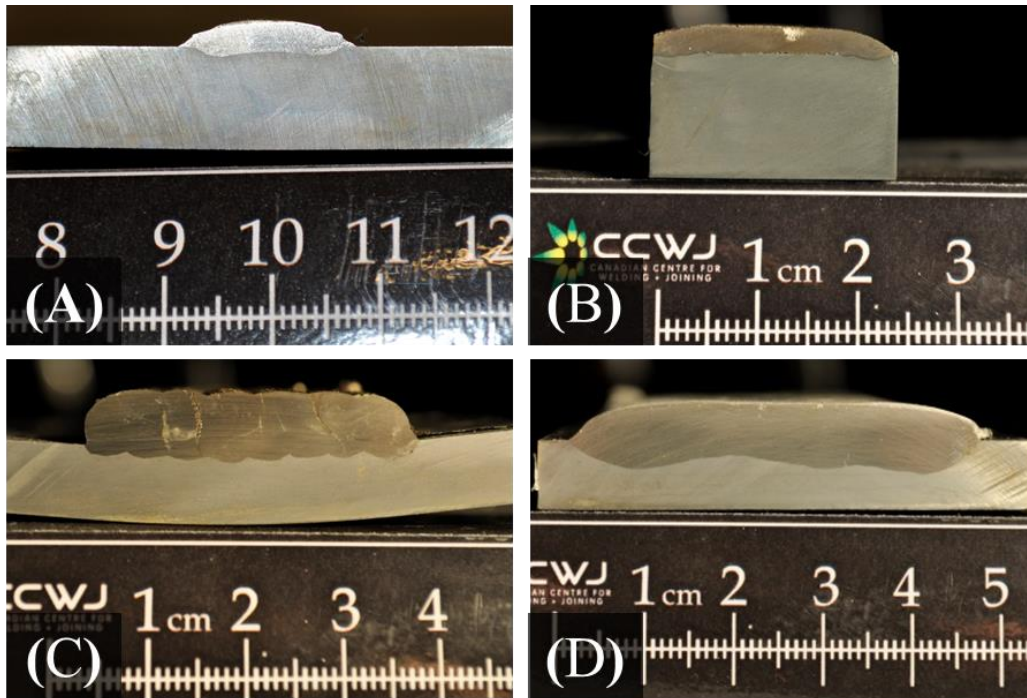
Figure 7-5: Cross section view of overlays from four different processes (A) PTAW 180A (B) LW1 (C) GMAW1 (D) SAW 25^{0}C

7.2.   Discussion

The appearance of the welds all very greatly, the weaving processes, square beam and stringers all give quit different appearances. For generalities the two processes that tend to give the nicest surface finishes are PTAW and LBW. It is much easier to apply thicker passes using the SAW or GMAW processes. The cross sections also make it apparent that the penetration ranges widely across the processes with the most to least being SAW, GMAW, PTAW, and LBW.

7.3.   Welding Parameters

This section examines the differences in the welding parameters and characteristics of the welds that were controlled. A summary of some of the most important parameters of the welds are given in Table 7-1.

Table 7-1: Welding parameters of the different welding processes compared

Sample Name	Voltage (V)	Current (A)	Power (KW)	Total Deposition (g/min)	Travel Speed (mm/s)	Heat Input (Kj/mm)
SAW RT	32.9	583	19.22	279	4.24	4.53
SAW 50	32.9	586	19.30	279	4.24	4.55
SAW 50%	32.8	478	15.73	279	4.24	3.71
GMAW1	24.0	225-220	5.40	49	8.47	0.51
GMAW2	28.0	255-265	7.28	61	8.47	0.69
PTAW 1	21.9	160	3.50	92	10.50	0.20
PTAW 2	28.9	180	5.20	92	10.50	0.30
PTAW 3	28.2	200	5.64	92	10.50	0.32
LBW 1	NA	NA	8.00	151	4.00	0.90
LBW 2	NA	NA	8.00	151	4.00	0.90
LBW 3	NA	NA	8.00	95	7.00	0.51
LBW 4	NA	NA	8.00	95	7.00	0.51

7.3.1 GMAW

Two different welds were made using a low range and conversely high range of the suggested settings. These should give us a fairly large difference in the heat input and cooling rates of the two GMA welds. The main differences between the two welds are shown in Table 7-2.

Table 7-2: GMAW parameters highlighting differences in the welds

Sample Name	Power (KW)	Wire Deposition (g/min)	WFS (m/min)	Heat Input (Kj/mm)
GMAW1	5.40	49.08	4.06	0.51
GMAW2	7.28	61.36	5.08	0.69

In addition to the given settings both of the welds were made using a argon shielding gas, a 17 mm CTWD and an interpass temperature of 150^0 C. The composition of the wire that was welded with is given in Table 7-3.

Table 7-3: Stoody 101 HC-01 Wire Composition

	C	P	Cr	Si	Mn	Fe	Zr	TiO$_2$	Fluorides
Wt. %	4-7	NA	16-24	1-3	1-3	Bal	0.05-2	<5	<2

7.3.2   Laser

The welded samples were made using Coherent's 8 KW laser. There are two pairs of different travel and deposition rates in which each had one sample that was not preheated and one sample that was pre heated. The differences in the settings used are shown in the Table 7-4.

Table 7-4: Welding Parameters

Sample Name	Powder Addition (g/min)	Travel Speed (mm/s)	Inter Pass Temp/ Preheat (Kelvin)	Heat Input (Kj/mm)
LBW 1	151.20	4.00	NA	0.90
LBW 2	151.20	4.00	523	0.90
LBW 3	94.50	7.00	NA	0.51
LBW 4	94.50	7.00	523	0.51

The powder that was used was a custom batch produced by Hoganas. The composition was made in an attempt replicate the initial composition of the Stoody wire. The actual composition of the powder welded with is given in Table 7-5.

Table 7-5: Composition of Hoganas powder used for laser welding

	C	P	Cr	Si	Mn	Fe	O	N
Wt.%	5.17	0.02	20.00	1.94	2.04	Bal	0.02	0.02

By using preheats this should give an idea of what the effect of the cooling rate is on LBW of CCO's. There is also a large difference in the heat inputs between the two samples so we should be able to get an idea of the effect of heat input on LBW CCOs

7.3.3 PTAW

Three different currents were chosen for the three different PTAWs. This should give an idea of what role current plays on the PTAW CCOs. All the weld voltages were measured using a hand held volt meter. The shielding and plasma gas used was argon and the shielding gas cup was placed 6 mm off of the base plate. The other pertinent information is given in Table 7-6 and the composition of the powder is given in Table 7-7.

Table 7-6: Welding parameters for PTAWs

Sample Name	Power (KW)	Travel Speed (mm/s)	Oscillation Speed (mm/s)	Heat Input (Kj/mm)
PTAW 1	3.50	10.50	250.00	0.20
PTAW 2	5.20	10.50	250.00	0.30
PTAW 3	5.64	10.50	250.00	0.32

Table 7-7: Composition of powder used for PTAWs

	C	Mn	Cr	Si	Fe	P	S	Mo	Cu	Al	O
Wt. %	6.14	1.13	50.37	0.45	40.93	0.02	0.02	0.86	0.00	0.04	0.03

The reason for the composition chosen for the powder was the result of trial and error. An attempt was made to match the composition of the SAWs but due to reasons that will be discussed in 7.5.3 it was not possible.

7.4. Discussion

The welding parameters chosen for the different processes were chosen for a variety of reasons. The settings were chosen based on settings that would produce decent quality welds with a hyper eutectic microstructure. Then other welds were chosen that could be examined to hopefully determine the effect of a certain variable on the welds. This way more than just a comparison of the welding processes can be carried out in order to increase the usefulness of this study.

7.5. Weld Microstructure

The microstructures of the different welding processes varied significantly. This section highlights the overall microstructure appearance from low magnifications and also the primary carbide microstructure at higher magnifications. For the GMAW, PTAW, and

LBW. The only measure of the carbides made was total volume fraction of carbide in the different welds. The carbides in the welds made using PTAW, GMAW and LBW are majority primary carbides so this is not a bad measure to compare them all by. Table 7-8 shows how there is a large variation in the total VF of carbides in the different processes. It should be noted that the VF for the GMAW was only taken from the second passes.

Table 7-8: Volume fraction comparison of different processes

Sample	Total VF Carbide
Base	22%
SAW 50%	46%
GMAW CCO1	30%
GMAW CCO2	23%
PTAW 160A	51%
PTAW 180A	30%
PTAW 200A	30%
LBW1	67%
LBW-2	55%
LBW-3	56%
LBW-4	50%

7.5.1   GMAW

Figure 7-6 shows an expanded view of the microstructure of the GMAW CCOs. The two different layers of passes are clearly visible. The bottom passes are completely void of primary carbides while the top pass consists of a hypereutectic microstructure. The weld contains relief cracking that extends through the height of the weld.

Figure 7-6: GMAW overall micrograph of CCO-1

Examining the microstructure at higher magnification in Figure 7-7 it can be seen that there appears to be different groupings of primary carbides because some contain groups of elongated rod like carbides while there are other groups of roughly equiaxed carbides. The eutectic carbide and austenite structure is much finer than in SAW. Due to the fact that the welding wire contains TiO the sample was also examined for TiC using BSD in

SEM as they could act as nucleation points. However, none were found in the sample examined. Some of the primary carbides also had a slightly different morphology where they were more hexagonal in shape and rather than centers with austenite there are thin lines extending in from the edges.
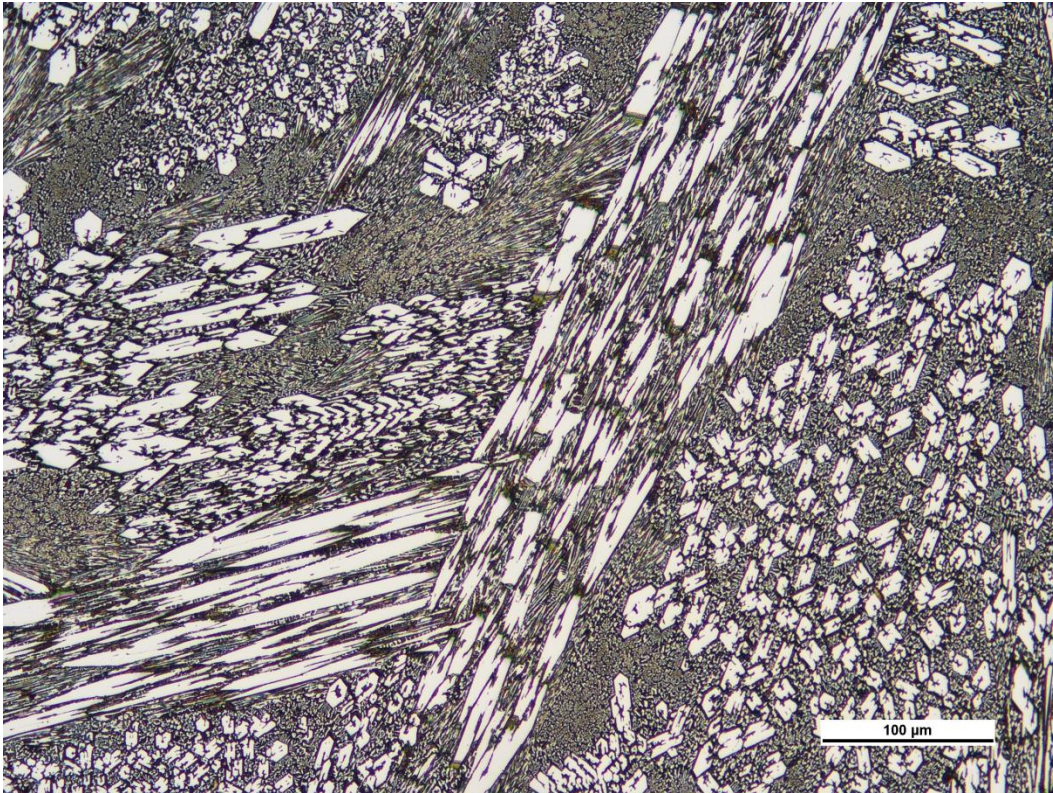
Figure 7-7: High magnification micrograph of CCO-1

7.5.2 Laser

In the laser welds we see a distinctive banding in the overlays with very fine rod like carbides close to the bottom and top of the weld as seen in Figure 7-8. In the middle of the overlay the carbides are much larger and there are more blade like carbides. At the very top of the weld pool are extremely fine carbides. Each of these areas is shown in greater detail in the next three photographs. Figure 7-9 starts by showing the bottom of the weld and Figure 7-10 and Figure 7-11 are the middle and the top of the weld respectively.
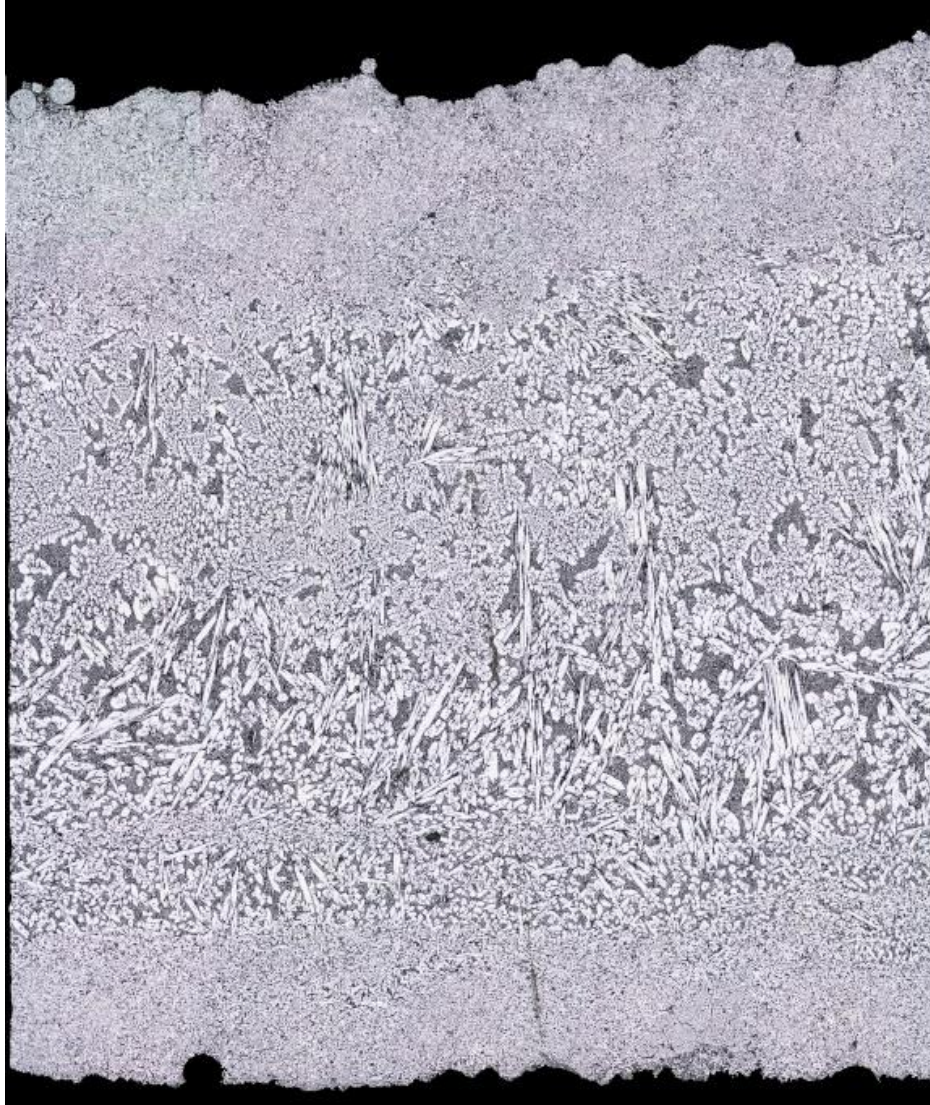
Figure 7-8: Weld microstructure overview of LBW 1
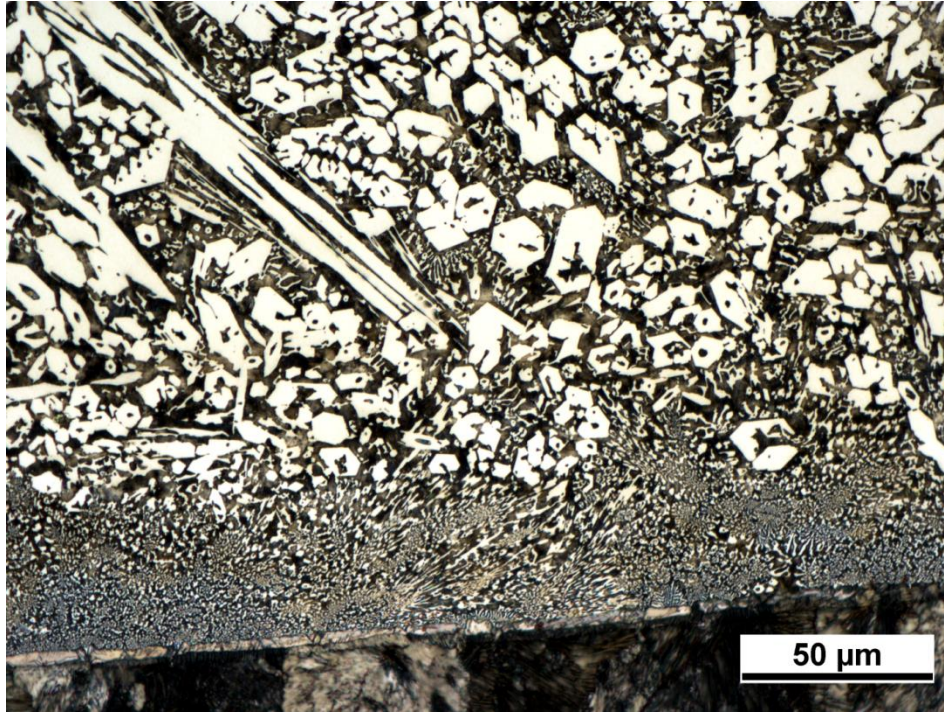
Figure 7-9: Bottom of weld and fusion line from LBW 2

The bottom of the weld had a small dissolution zone that consisted of what appears to be a eutectic of M_7C_3 and austenite. Directly above this zone the microstructure consists of primary carbides surrounded by the eutectic matrix of M_7C_3 and austenite. These microstructural features are not consistent throughout all of the laser welds; in some cases the carbides at the bottom closely resemble the carbides at the top of the weld.
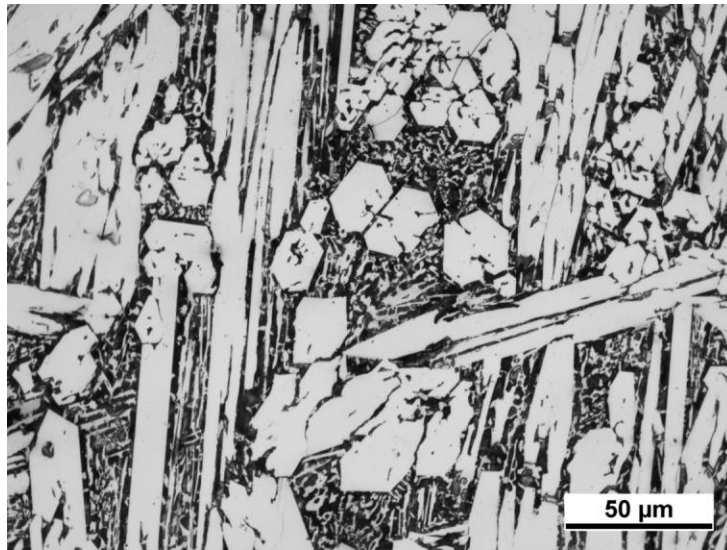
Figure 7-10: LBW 2 middle of weld microstructure

At the center of the welds the microstructure was primary carbides surrounded by a eutectic austenite and M_7C_3.
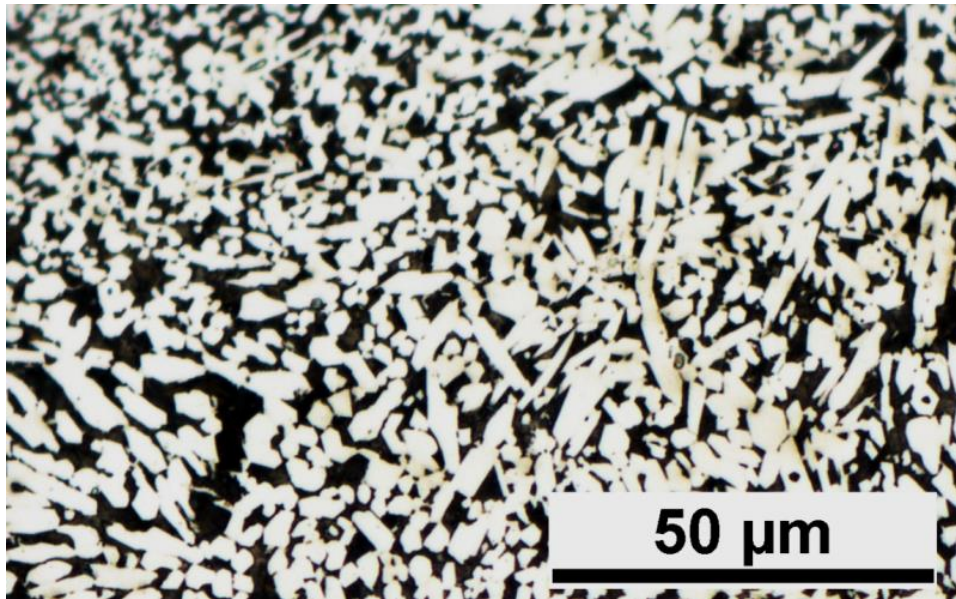
Figure 7-11: LBW 2 top of weld microstructure

The top of the welds consists of many very small type of carbide surrounded by austenite. The morphology of the carbides is significantly different than typical primary carbides. Rather than the hexagonal shapes that often have pockets of austenite inside of them these carbides do not appear to have any cores when examined using optical microscopy, they still have a facetted appearance like the primary carbides. However, when examined at high magnification such as in Figure 7-12 using BSD in a SEM the small carbides do appear to have extremely small cores. The resolution was too low to carry out analysis on the carbides and the cores.
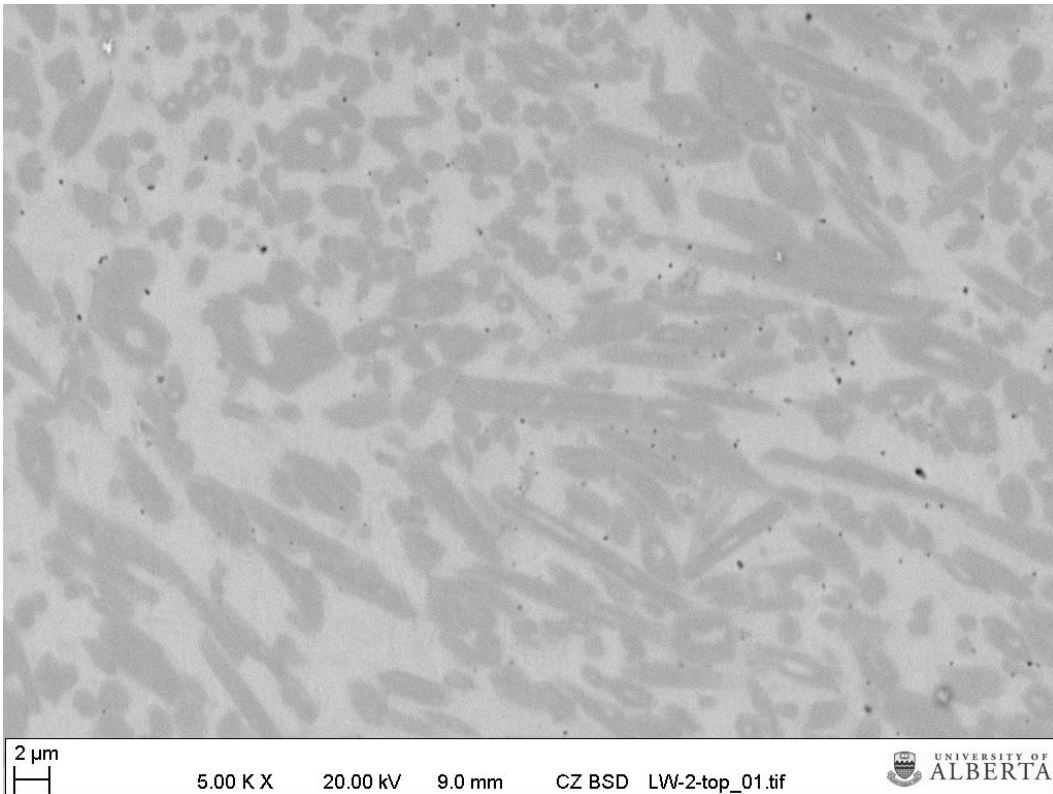
Figure 7-12: SEM BSD high magnification of small carbides at top of LBW2

7.5.3   PTAW

The microstructure of the PTAW welds differs significantly from the other process microstructure because it has a very high volume fraction of unmelted powder particles as seen in Figure 7-13. As previously discussed the first attempts to make the PTAW welds were made using a powder composition that would have given an overlay composition similar to the ones for the SAW.
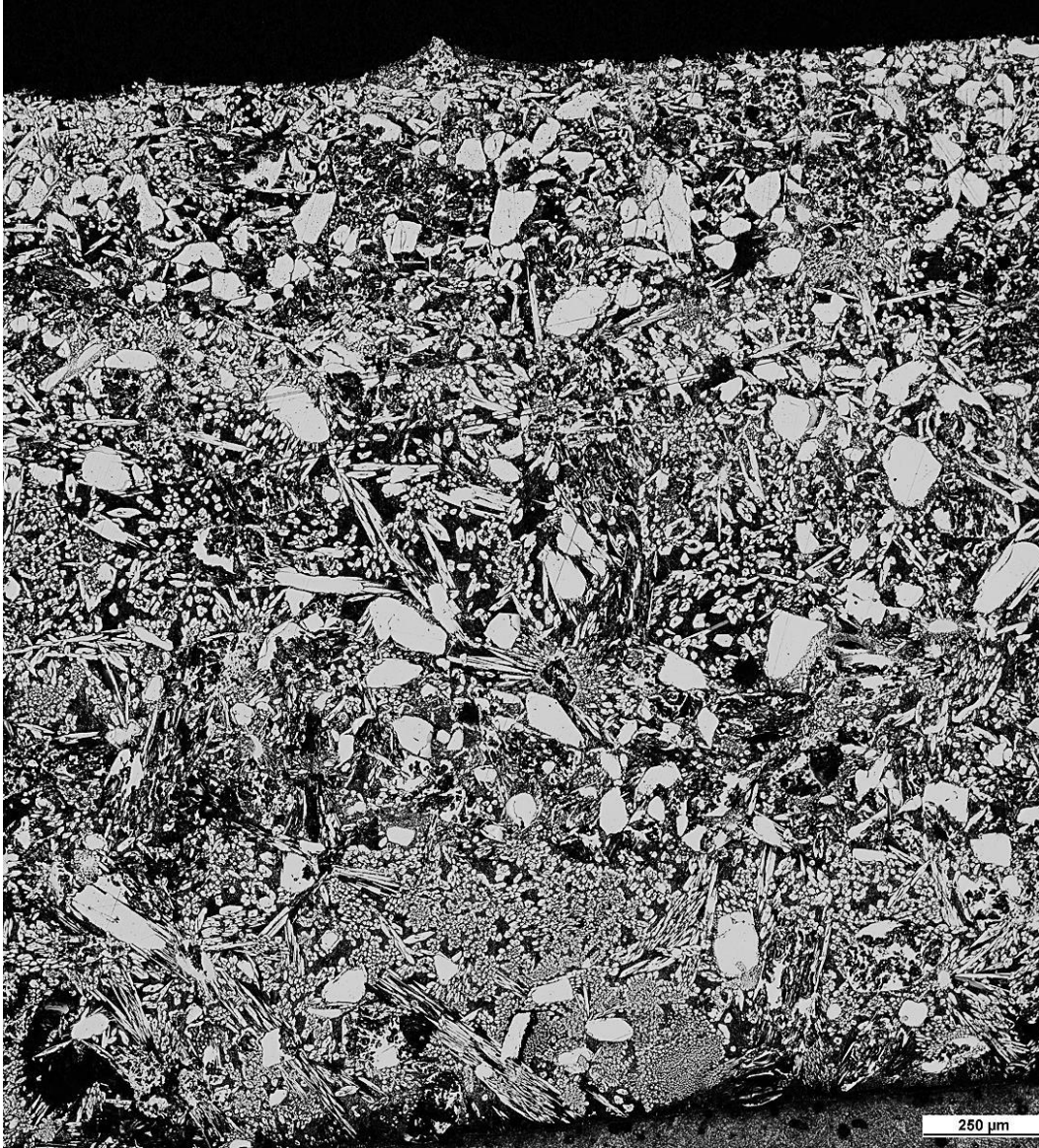
Figure 7-13: Overall micrograph of PTAW weld at 160A

The problem with the first attempts to make the PTAWs was that the microstructure did not consist of any carbide other than the large unmelted ones as seen in Figure 7-14.
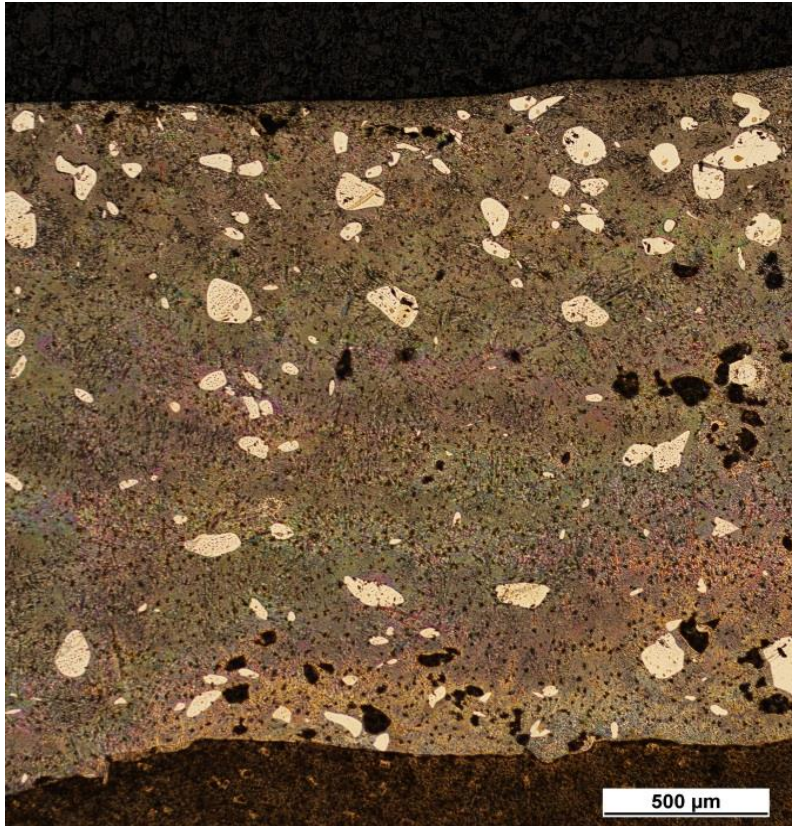
Figure 7-14: PTAW first attempts with no primary carbides

After more trials in which the amount of chromium and carbon was increased and the particle size of the powders was decreased overlays with a large fraction of primary carbides such as shown in Figure 7-15 were produced.
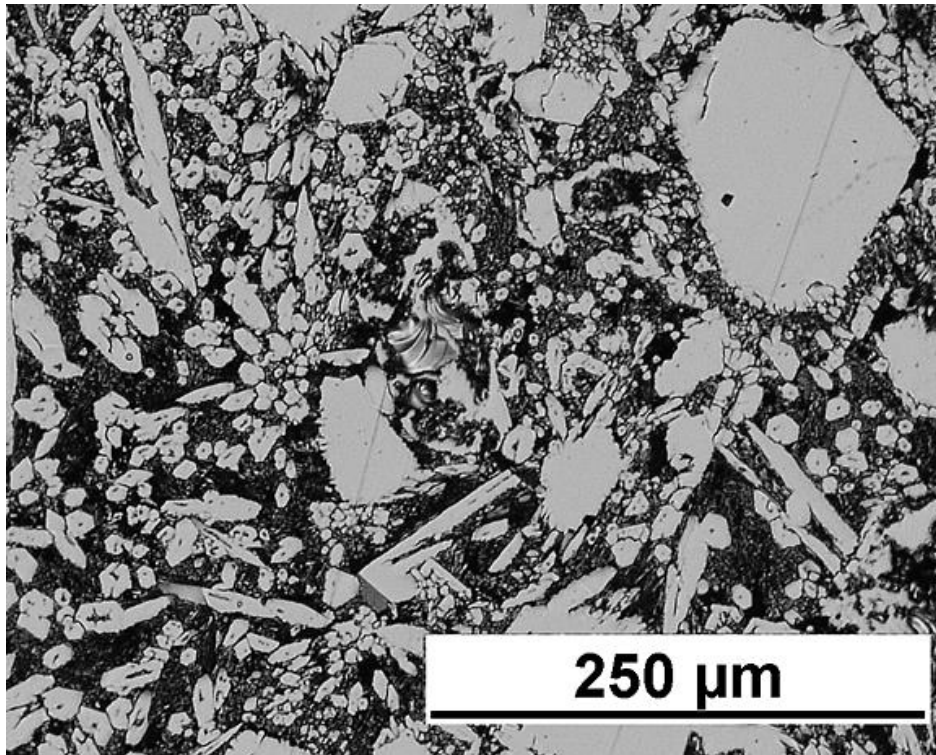
Figure 7-15: PTAW 160a micrograph of hypereutectic microstructure

7.6.   Discussion

The GMAW welds showed clearly one of the main disadvantages to using this process is the high amount of dilution which causes the first pass to be void of primary carbides. The volume fraction of carbides was found to be 23% for the higher heat input and 30% for the lower heat input. One possible reason for this is that the lower current of the lower heat input sample led to less dilution in the weld. The work on the GMAW from section 6.2 showed that there is a lot of blade like primary carbides in them because their orientation is more perpendicular to the base plate than parallel to the base plate. This may be one advantage to GMAW as some research has shown that this orientation is better for impact resistance [56]. One disadvantage to GMAW was its deposition rate was lowest compared to the other processes. Being unable to make custom alloys and relying on manufacturers specifications of wires, and the need for multiple passes are also downsides of GMAW.

The large number of primary carbides in the LBW can be explained because the low amount of dilution means that the resulting composition of the weld is very hypereutectic.

143

The laser welds had between 50 and 67% which only one PTAW was able to reach. Because of this high amount of carbides in LBW we would expect the wear resistance to be high. Another advantage of LBW was the deposition rate was good with only SAWs being higher.

There are a few problems with the LBW overlays. There appears to be some problems with cracking and lack of fusion. The lack of fusion is especially prevalent in LBW 1 and LBW 4. An example of this in LBW 1 is shown in Figure 7-16.
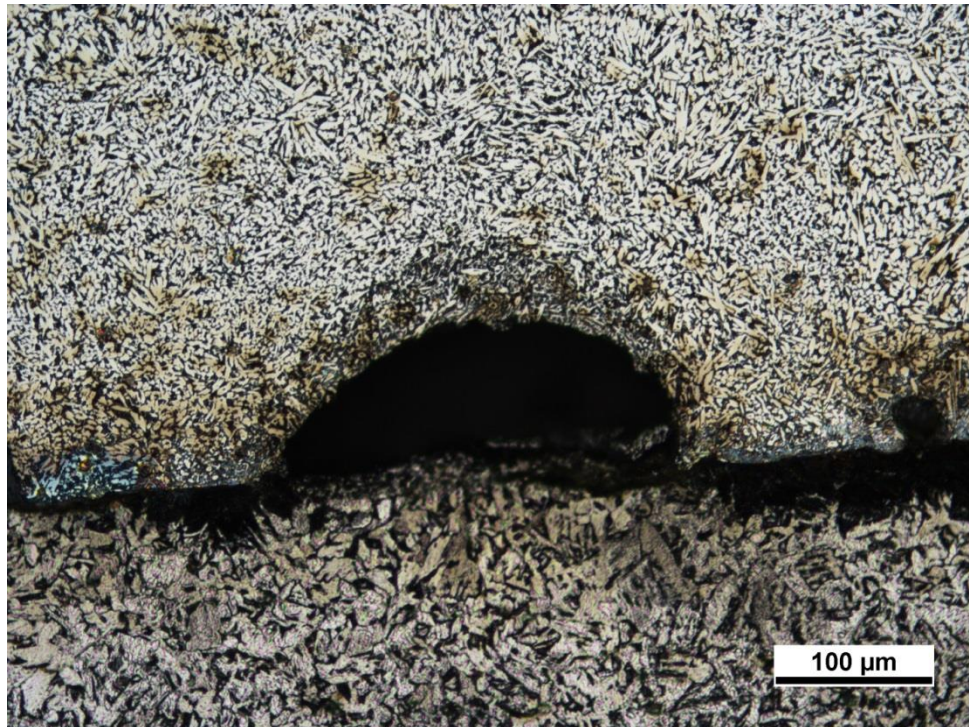
Figure 7-16: Porosity and lack of fusion

The reason for the banding in the microstructure is also unclear but one thing that may be causing it is how the powder is fed. If solid powder is hitting the weld pool as it is freezing behind the arc then this may be increasing the cooling rate which leads to less time for diffusion resulting in the smaller morphology of carbides. The finer carbides on the bottom of the weld can also be attributed to this fact that the cooling rate will be high there.

The size of the carbides appears to be larger for the LBW 1 and LBW 2 compared to the other two welds. This could be attributed to a slower cooling rate because of the slower travel speed and higher heat inputs of LBW 1 and LBW 2. Both LBW 3 and LBW 4 also

have large amounts of fine carbides compared to the amounts found in the other two welds. The effect of the preheats in the LBW appeared to decrease the VF of the carbides.

The low amount of dilution involved with LBW may be an advantage because of the resulting microstructure, but it may have a negative effect by making the overlay more susceptible to spalling especially with the lack of fusion occurring is some locations. Tests should be carried out to see what affect the low diffusion has on the toughness of the overlays. The high cost of LBW equipment is one of the big draw backs but its high deposition and the possibility of extremely high wear resistance because of the high VF of carbides may make it a realistic process for the application of CCOs

The PTAW welds vary quite a bit in their properties, The PTAW made at 160A had very good VF of carbides at 51%, but the other two were lower at 30% each. The heat input of the welds was the lowest of all the processes which may explain why there were so many unmelted particles in the microstructure. The effect that the large amount of unmelted particles has on the wear resistance of the overlays could be a major factor in the success or not of the welds. The PTAWs deposition rate is not the highest but there is still a lot of room for improvements and increased deposition rates which could be advantages of the process. The costs for PTAW machines is lower than for LBW systems, yet it is still substantially more than for GMAW and SAW machines which is a big disadvantage of the PTAW process.

Overall when we compare the different processes it is impossible to come up with a best process for applying CCOs. SAW has the highest deposition rate and volume fraction of carbides can be very high when AC welding is used. PTAW both have advantages of microstructures that can have extremely high fractions of carbides but both have the downside of huge equipment costs. GMAW has the advantages of being the most versatile and having low equipment costs but it is the only process where unless you're a consumables manufacturer you have little control over what goes into your welds. In the end the process that would work best will be very dependent on the application of the CCOs.

8. Conclusions and Recommendations

8.1. Conclusions

This work has looked at two main themes, the microstructure characterization of CCOs and secondly how changes in the SAW process and other welding processes affect CCOs. It is critical to understand the microstructure of CCOs as it is gives them their wear resistance. Also, the more you understand the microstructure the more tools that you can use to control or change them to make higher quality overlays. We found that the rice crispies were unmelted alloy powders that did not dissolve in the weld metal. Examination of them in wear scars showed that may actually increase the wear resistance of the overlay because of their high hardness. The morphology of the primary carbides was also shown conclusively by using a 3D sectioning technique as being long hexagonal rods. We found that the banded structure of hypereutectic microstructure at the top, eutectic and/or hypoeutectic towards the bottom of the welds is caused by concentration differences where the carbon and chromium decrease towards the fusion line.

Balance during AC welding was found to have a large effect on the microstructure and properties of CCOs produced with otherwise identical settings. One major change was that the amount dilution in the samples decreased considerably as the balance was decreased. This decrease in balance led to higher amounts of hypereutectic microstructure, higher volume fraction of primary carbides, and larger average primary carbide size. These changes in microstructure should lead to an overlay that has better wear resistances. In addition using AC welding was shown to successfully eliminate the banding in the microstructure which should give better properties through the entire height of the welds. PTAW and LBW processes were also able to achieve the same benefit of eliminating the banding in the microstructure.

8.2. Recommendations

For further work the wear resistance of the overlays produced using the different processes should be examined by performing G65 wear tests on them to confirm the assumptions that the increased volume fractions would lead to improved wear results in the samples. The experiments for CTWD should be repeated in a lab setting in order to have better control over the parameters and process monitoring capabilities. An experiment should be designed to determine the effect of the rice crispies on the wear resistance. This could be possibly done by producing PTAWs that have a high fraction of

unmelted particles and using very fine and conversely very coarse ferrochrome powders of the same composition. The finer powders should melt more readily and leave a lower volume fraction of the large carbides and contribute more Cr and C to the overall composition of the overlay. To examine the effect of dilution and segregation on the banding structure an experiment could be made where a weld is made onto a substrate that will not contribute to dilution whether this a because it is cooled enough that no fusion occurs or perhaps by welding on a white cast iron of similar composition. This would show whether or not there is segregation that is caused during solidification or dilution. In order to determine if mixing causes any of the differences in composition experiments could be carried out examining the effect of powder profile. It may also be worthwhile to examine the composition of primary carbides throughout the height of a weld and see if there is any pattern to the composition of them.

9. References

[1] C. Lin, C. Chang, J. Chen, C. Hsieh and W. Wu, "Microstructure and wear characteristics of high-carbon Cr-based alloy claddings formed by gas tungsten arc welding (GTAW)," *Surface and Coatings Technology,* vol. 205, pp. 2590-2596, 12/25, 2010.

[2] P. F. Mendez, N. Barnes, K. Bell, S. D. Borle, S. S. Gajapathi, S. D. Guest, H. Izadi, A. K. Gol and G. Wood, "Welding processes for wear resistant overlays," *Journal of Manufacturing Processes, .*

[3] C. K. Kim, S. Lee, J. Jung and S. Ahn, "Effects of complex carbide fraction on high-temperature wear properties of hardfacing alloys reinforced with complex carbides," *Materials Science and Engineering: A,* vol. 349, pp. 1-11, 5/25, 2003.

[4] G. Azimia and M. Shamanian, "Effects of silicon content on the microstructure and corrosion behavior ofFe–Cr–C hardfacing alloys," *Journal of Alloys and Compounds,* pp. 598-603, 2010.

[5] Chia-Ming Chang, Chih-Chun Hsieh, Chi-Ming Lin, Jie-Hao Chen, Chih-Ming Fan and Weite Wu. Effect of carbon content on microstructure and corrosion behavior ofhypereutectic Fe–Cr–C claddings. *Materials Chemistry and Physics* .

[6] R. Chotěborský, P. Hrabě, M. Müller, R. Válek, J. Savková and M. Jirka, "Effect of carbide size in hardfacing on abrasive wear," *Research in Agricultural Engineering,* vol. 55, pp. 149-158, 2009.

[7] M. Kirchgaßner, E. Badisch and F. Franek. Behaviour of iron-based hardfacing alloys under abrasionand impact. *Wear (265),* pp. 772-772-779. 2008.

[8] C. Chang, L. Chen, C. Lin, J. Chen, C. Fan and W. Wu, "Microstructure and wear characteristics of hypereutectic Fe–Cr–C cladding with various carbon contents," *Surface & Coatings Technology,* 2010.

[9] O. Dogan, J. Hawk and G. Laird, "Solidification structure and abrasion resistance of high chromium white irons," *Metall. Mater. Trans. A-Phys. Metall. Mater. Sci.,* vol. 28, pp. 1315-1328, JUN, 1997.

[10] C. Lin, H. Lai, J. Kuo and W. Wu, "Effect of carbon content on solidification behaviors and morphological characteristics of the constituent phases in Cr-Fe-C alloys," *Mater Charact,* vol. 62, pp. 1124-1133, DEC, 2011.

[11] J. F. Flores and A. Neville, "Materials Selection in the Oilsands Industry based on Materials Degradation Mechanisms," *Exploration and Production,* vol. 7, pp. 42-45, .

[12] J. F. Flores, A. Neville, N. Kapur and A. Gnanavelu, "Erosion–corrosion degradation mechanisms of Fe–Cr–C andWC–Fe–Cr–C PTAoverlays in concentrated slurries," pp. 1811-1820, .

[13] G. Fisher, T. Wolfe, M. Yarmuch, A. Gerlich and P. Mendez, "The use of protective weld overlays in oil sands mining," *Australasian Welding Journal,* vol. 57, pp. 12, 2012.

[14] H. Sabet, S. Khierandish, S. Mirdamadi and M. Goodarzi, "The Microstructure and Abrasive Wear Resistance of Fe-Cr-C Hardfacing Alloys with the Composition of Hypoeutectic, Eutectic, and Hypereutectic at Cr/C=6," *Tribol. Lett.,* vol. 44, pp. 237-245, NOV, 2011.

[15] F. Scandella and R. Scandella, "Development of hardfacing material in Fe-Cr-Nb-C system for use under highly abrasive conditions," *Materials Science & Technology,* vol. 20, pp. 93-105, 01, 2004.

[16] B. Gülenç and N. Kahraman, "Wear behaviour of bulldozer rollers welded using a submerged arc welding process," *Mater Des,* vol. 24, pp. 537-542, 10, 2003.

[17] B. G. Mellor, *Welding Surface Treatment Methods for Protection Against Wear.* 2006.

[18] C. A. Natalie, D. L. Olson and M. Blander, "Physical and chemical behavior of welding fluxes," *Annual Review of Materials Science,* vol. 16, pp. 389-413, 1986.

[19] G. POWELL, R. CARLSON and V. RANDLE, "The Morphology and Microtexture of M(7)c(3) Carbides in Fe-Cr-C and Fe-Cr-C-Si Alloys of Near Eutectic Composition," *J. Mater. Sci.,* vol. 29, pp. 4889-4896, SEP 15, 1994.

[20] V. E. Buchanan, P. H. Shipway and D. G. McCartney, "Microstructure and abrasive wear behaviour of shielded metal arc welding hardfacings used in the sugarcane industry," *Wear,* vol. 263, pp. 99-110, 9/10, 2007.

[21] C. Chang, Y. Chen and W. Wu, "Microstructural and abrasive characteristics of high carbon Fe–Cr–C hardfacing alloy," *Tribology International,* pp. 929-934, 2010.

[22] B. Hinckley, K. Dolman, R. Wuhrer, W. Yeung and A. Ray, "SEM investigation of heat treated high-chromium cast irons," in *Materials Forum,* 2008, pp. 55-71.

[23] A. Neville, F. Reza, S. Chiovelli and T. Revega, "Characterization and corrosion behavior of high-chromium white cast irons," *Metall. Mater. Trans. A-Phys. Metall. Mater. Sci.,* vol. 37A, pp. 2339-2347, AUG, 2006.

[24] Y. ZHOU, Y. YANG, D. LI, J. YANG, Y. JIANG, X. REN and Q. YANG, "Effect of Titanium Content on Microstructure and Wear Resistance of Fe-Cr-C Hardfacing Layers," *Welding Journal,* 2012.

[25] G. POWELL, "Solidification of Undercooled Bulk Melts of Fe-Cr-C, Co-Cr-C and Ag-Ge Alloys of Near-Eutectic Composition," *Mater. Trans. JIM,* vol. 31, pp. 110-117, FEB, 1990.

[26] V. Kumar, "Formation and morphology of M7C3 in low Cr white iron alloyed with Mn and Cu," *J. Mater. Eng. Perform.,* vol. 12, pp. 14-18, FEB, 2003.

[27] C. Schon and A. Sinatora, "Simulation of solidification paths in high chromium white cast irons for wear applications RID F-1494-2010 RID B-5107-2010," *Calphad-Comput. Coupling Ph. Diagrams Thermochem.,* vol. 22, pp. 437-448, DEC, 1998.

[28] J. T. H. Pearce, T. Chairuangsri, L. Wiengmoon, N. Poolthong and H. Nomura, "Use of electron microscopy on rnicrostructure characterization of high chromium cast irons," *China Foundry,* vol. 4, pp. 38-43, FEB, 2007.

[29] G. LAIRD, J. RAWERS and A. ADAMS, "Fractal Analysis of Carbide Morphology in High-Cr White Cast Irons," *Metallurgical Transactions A-Physical Metallurgy and Materials Science,* vol. 23, pp. 2941-2945, OCT, 1992.

[30] C. Tabrett, I. Sare and M. Ghomashchi, "Microstructure-property relationships in high chromium white iron alloys," *International Materials Reviews,* vol. 41, pp. 59-82, 1996.

[31] O. Dogan, "Effect of chemical composition and superheat on the macrostructure of High Cr White iron castings," 2005.

[32] G. L. F. Powell, I. H. Brown and G. D. Nelson, "Tough hypereutectic high chromium white iron - A double in-situ fibrous composite," *Frontiers in Materials Science and Technology,* vol. 32, pp. 111-114, 2008.

[33] X. H. Zhi, J. D. Xing, H. G. Fu and Y. M. Gao, "Effect of fluctuation, modification and surface chill on structure of 20%Cr hypereutectic white cast iron," *Mater. Sci. Technol.,* vol. 25, pp. 56-60, JAN, 2009.

[34] Y. Matsubara, N. Sasaguri, K. Shimizu, S. Yu and K. Yu, "Solidification and abrasion wear of white cast irons alloyed with 20% carbide forming elements," *Wear,* vol. 250, pp. 502-510, OCT, 2001.

[35] J. T. H. Pearce, "Structure and Wear Performance of Abrasion Resistant Chromium White Cast Irons," *American Foundry Society Transaction,* vol. 84, pp. 599-622, 1984.

[36] S. Atamert and H. K. D. H. Bhadeshia, "Microstructure and stability of Fe☐Cr☐C hardfacing alloys," *Materials Science and Engineering: A,* vol. 130, pp. 101-111, 11/20, 1990.

[37] J. PEARCE, "Examination of M7c3 Carbides in High Chromium Cast Irons using Thin Foil Transmission Electron-Microscopy," *J. Mater. Sci. Lett.,* vol. 2, pp. 428-432, 1983.

[38] Q. Wang and X. Li, "Effects of Nb, V, and W on Microstructure and Abrasion Resistance of Fe-Cr-C Hardfacing Alloys," *Welding Journal,* vol. 89, pp. 133S-139S, JUL, 2010.

[39] Z. Wang, Q. Wang, L. Cui, A. Yang and D. He, "Influence of cooling rate and composition on orientation of primary carbides of Fe–Cr–C hardfacing alloys," *Science and Technology of Welding & Joining,* vol. 13, pp. 656-662, 2008.

[40] A. Inanlou, S. H. Seyedein and M. R. Aboutalebi, "The Effect of Semi-solid Parameters on the Microstructure and Hardness of high Chromium Cast Irons," *Science and Processing of Cast Iron Ix,* vol. 457, pp. 84-89, 2011.

[41] V. RANDLE and G. LAIRD, "A Microtexture Study of Eutectic Carbides in White Cast Irons using Electron Backscatter Diffraction," *J. Mater. Sci.,* vol. 28, pp. 4245-4249, AUG 1, 1993.

[42] S. Carpenter, D. Carpenter and J. Pearce, "XRD and electron microscope study of an as-cast 26.6% chromium white iron microstructure," *Mater. Chem. Phys.,* vol. 85, pp. 32-40, MAY 15, 2004.

[43] Z. Jiyang and L. Jincheng, "Colour Metallography of Cast Iron," *中国铸造 SCI,* vol. 8, 2011.

[44] R. B. Gundlach, "White iron and high-alloyed iron castings, casting," in *ASM Handbook*Anonymous ASM International, 2008, pp. 896-903.

[45] P. Zhang, Y. Zhou, J. Yang, D. Li, X. Ren, Y. Yang and Q. Yang, "Optimization on mechanical properties of Fe7−xCrxC3 carbides by first-principles investigation," *J. Alloys Compounds,* vol. 560, pp. 49-53, 5/25, 2013.

[46] C. M. Fang, M. A. van Huis and H. W. Zandbergen, "Structural, electronic, and magnetic properties of iron carbide Fe(7)C(3) phases from first-principles theory RID E-9916-2011," *Phys. Rev. B,* vol. 80, pp. 224108, DEC, 2009.

[47] E. Bauer-Grosse, J. Morniroli, M. Khachfi, M. Gantois, T. Lundström and A. Courtois, "Crystallography of M$_7$C$_3$ carbides and M'$_7$B$_3$ borides: The difference in the local order in carbides and borides to explain the nature and density of defects in these compounds," *Journal of the Less Common Metals,* vol. 117, pp. 231-236, 1986.

[48] Y. F. Zhou, Y. L. Yang, Y. W. Jiang, J. Yang, X. J. Ren and Q. X. Yang, "Fe-24 wt.%Cr-4.1 wt.%C hardfacing alloy: Microstructure and carbide refinement mechanisms with ceria additive," *Mater Charact,* vol. 72, pp. 77-86, OCT, 2012.

[49] VANDENBO.J and L. WOLFF, "Growth and Properties of Monovariant (Fe,cr)-(Cr,fe)7c3 Eutectic System," *J. Cryst. Growth,* vol. 15, pp. 11-&, 1972.

[50] G. LAIRD and G. POWELL, "Solidification and Solid-State Transformation Mechanisms in Si Alloyed High-Chromium White Cast Irons," *Metallurgical Transactions A-Physical Metallurgy and Materials Science,* vol. 24, pp. 981-988, APR, 1993.

[51] Z. Jiyang, "White cast iron," in *Colour Metallography of Cast Iron*Anonymous CHINA FOUNDRY, August 2011, pp. 337-337-349.

[52] S. H. M. Anijdan, A. Bahrami, N. Varahram and P. Davami, "Effects of tungsten on erosion-corrosion behavior of high chromium white cast iron," *Materials Science and Engineering A-Structural Materials Properties Microstructure and Processing,* vol. 454, pp. 623-628, APR 25, 2007.

[53] T. OHIDE and G. Ohira, "Solidification of the High Chromium Alloyed Cast Iron," *The British Foundryman,* vol. 76, pp. 7-14, 1983.

[54] GIGLIOTT.MF, G. COLLIGAN and G. POWELL, "Halo Formation in Eutectic Alloy Systems," *Metallurgical Transactions,* vol. 1, pp. 891-&, 1970.

[55] Z. J. Liu, Y. H. Su and J. G. Sun, "Effects of shape and distribution of M7C3 on wear resistance of iron based composite," *Surface Engineering (Icse 2007),* vol. 373-374, pp. 560-563, 2008.

[56] S. Wang, L. Song, Y. Qiao and M. Wang, "Effect of Carbide Orientation on Impact-Abrasive Wear Resistance of High-Cr Iron Used in Shot Blast Machine," *Tribology Letters,* vol. 50, pp. 439-448, JUN, 2013.

[57] Anonymous "Triten™ Guide to the Evaluation & Selection of HARDFACED PLATE," pp. 1-8, .

[58] G. POWELL and P. LLOYD, "A Deep Etching Technique for the Examination of the Carbide of High Chromium Cast-Iron in a Scanning Electron-Microscope," *Metallography,* vol. 14, pp. 271-274, 1981.

[59] D. Kotecki and J. Ogborn, "Abrasion resistance of iron-based hardfacing alloys," *Welding Journal,* vol. 74, pp. 269s-278s, 1995.

[60] S. ATAMERT and H. BHADESHIA, "Comparison of the Microstructures and Abrasive Wear Properties of Stellite Hardfacing Alloys Deposited by Arc-Welding and Laser Cladding," *Metallurgical Transactions A-Physical Metallurgy and Materials Science,* vol. 20, pp. 1037-1054, JUN, 1989.

[61] V. V. Díaz, J. C. Dutra and A. S. C. D'Oliveira, "Hardfacing by Plasma Transferred Arc Process," .

[62] V. I. Sannikov, L. A. Kazakov and V. S. Shulepov, "Influence of the length of stick-out of electrode wire on the coefficient of fusion and the size of the joint," *Chemical and Petroleum Engineering,* vol. 17, pp. 40-41, 1981.

[63] S. Lee, S. Choo, E. Baek, S. Ahn and N. Kim, "Correlation of microstructure and fracture toughness in high-chromium white iron hardfacing alloys," *Metall. Mater. Trans. A-Phys. Metall. Mater. Sci.,* vol. 27, pp. 3881-3891, DEC, 1996.

[64] G. Nelson, "The influence of microstructure on the corrosion and wear mechanisms of high chromium white irons in highly caustic solutions." 2010.

[65] H. Liu, F. Yu, Q. Meng, S. Chen and H. Wang, "Microstructure and properties of Fe-Cr-C hardfacing alloys reinforced with TiC-TiB2," *Science and Technology of Welding & Joining,* vol. 17, pp. 419-423, 2012.

[66] H. Berns and A. Fischer, "Abrasive wear resistance and microstructure of Fe-Cr-C-B hard surfacing weld deposits," *Wear,* vol. 112, pp. 163-180, 11/1, 1986.

[67] R. Menon Ph. D, J. Wallin and T. Barnhart. The development of corrosion-abrasion resistant overlays for oil sands applications.

[68] S. Maldonado-Ruiz, D. Lopez, A. Velasco and R. Colas, "Microstructural evaluation of wear resistant high chromium, high carbon cast irons," *Mater. Sci. Technol.,* vol. 20, pp. 393-398, MAR, 2004.

[69] K. Yamamoto, M. Hashimoto, N. Sasaguri and Y. Matsubara, "Solidification of High Chromium Cast Iron Substituted by 25 to 70 mass%Ni for Fe," *Materials Transactions,* vol. 50, pp. 2253-2258, SEP, 2009.

[70] A. Bedolla Jacuinde and W. Rainforth, "The wear behaviour of high-chromium white cast irons as a function of silicon and Mischmetal content," *Wear,* vol. 250, pp. 449-461, 2001.

[71] X. Wu, J. Xing, H. Fu and X. Zhi, "Effect of titanium on the morphology of primary M7C3 carbides in hypereutectic high chromium white iron," *Mater. Sci. Eng. A-Struct. Mater. Prop. Microstruct. Process.,* vol. 457, pp. 180-185, MAY 25, 2007.

[72] Z. F. Huang, J. D. Xing, X. H. Zhi and Y. M. Gao, "Effect of Ti addtion on the morphology and size of Primary M7C3 type Carbide in hypereutectic high chromium cast iron," *Materials Science & Technology,* vol. 27, pp. 426-430, 2011.

[73] de Melo Leite, Ricardo Vinicius and P. V. Marques, "Comparative study of the wear resistance of three metal-fluxed core wire-welded coatings used in industry," *Welding International,* vol. 25, pp. 917-922, 2011.

[74] M. Dumovic, "Repair and maintenance procedures for heavy machinery components," *Welding Innovations,* vol. 1, pp. 20-25, 2003.

[75] J. Pearce, "Abrasive wear behaviour of alloy cast irons," *Br.Foundryman,* vol. 78, pp. 13-23, 1985.

[76] S. G. Sapate and A. V. Rama Rao, "Effect of carbide volume fraction on erosive wear behaviour of hardfacing cast irons," *Wear,* vol. 256, pp. 774-786, 4, 2004.

[77] A. Kagawa, S. Kawashima and Y. Ohta, "Wear Properties of (Fe, Cr)~ 7C~ 3 Carbide Bulk Alloys," *Materials Transactions-JIM,* vol. 33, pp. 1171-1171, 1992.

[78] A. Klimpel, L. Dobrzanski, D. Janicki and A. Lisiecki, "Abrasion resistance of GMA metal cored wires surfaced deposits," *J. Mater. Process. Technol.,* vol. 164, pp. 1056-1061, MAY 15, 2005.

[79] A. Standard, "G65-04, 2010,"," *Standard Test Method for Measuring Abrasion using the Dry Sand/Rubber Wheel Apparatus," ASTM International, West Conshohocken, PA,* 2010.

[80] S. Buytoz, "Microstructural properties of M_7C_3 eutectic carbides in a Fe–Cr–C alloy," *Mater Lett,* vol. 60, pp. 605-608, 2006.

[81] M. Buchely, J. Gutierrez, L. Leon and A. Toro, "The effect of microstructure on abrasive wear of hardfacing alloys," *Wear,* vol. 259, pp. 52-61, 2005.

[82] M. Jones and R. J. Llewellyn, "Erosion-Corrosion Assessment of Tungsten Carbide-Based Plasma-Tranferred Arc-Welded Overlays," *Corrosion,* vol. 68, pp. 026003, FEB, 2012.

[83] G. Fisher, D. Crick, J. Wolodko, D. Kichton and L. Parent, "Impact Testing Of Materials For Oil Sands Processing Applications," *CORROSION 2007,* 2007.

[84] A. Zikin, I. Hussainova, C. Katsich, E. Badisch and C. Tomastik, "Advanced chromium carbide-based hardfacings," *Surface and Coatings Technology,* vol. 206, pp. 4270-4278, 5/25, 2012.

[85] J. Pepin, M. Yarmuch, G. Casey, H. Henein, D. G. Ivey and L. Choi. The effects of current and voltage waveforms on submerged arc welding productivity.

[86] D. E. Malcolm, "The effects of variable changes in alternating current output in submerged arc welding," in 2012, pp. 1-17.

10. Appendix

A. Analysis of areas around rice crispies

		C	Si	Cr	Mn	Fe	Mo
Rice Krispie	Sample Jan 21 RT	8.009128	0.015051	71.64536	0	20.33046	0
Rim	no starburst	7.198026	0.03829	55.12055	1.167199	35.92716	0.548777
Eutectic		3.610342	0.329728	23.54698	2.02316	69.98255	0.507236
Carbide		7.46887	0.042349	52.74275	1.142548	37.86123	0.742255
Overall		3.961715	0.319493	20.66399	2.321412	71.94351	0.789887
Rice Krispie	Sample Jan 22 RT	11.58084	0.079694	83.72109	0	4.548388	0.069984
Rim	significant starburst	8.041106	0.046334	65.86811	0.143191	25.7472	0.154058
Eutectic		4.130212	0.396019	21.33514	2.099805	71.38083	0.657993
Carbide		7.654138	0.066735	55.26431	1.190222	35.15044	0.67415
Overall		4.667304	0.338927	24.56578	2.203326	67.12084	1.103821
Rice Krispie	Sample Jan 22 -20	7.92218	0.081052	74.41741	0	17.50853	0.070829
Rim	no significant star burst	7.436971	0.044881	55.79681	1.055872	35.20441	0.461057
Eutectic		4.014446	0.347398	21.44819	2.300736	71.34296	0.546267
Carbide		7.44841	0.13275	53.66951	1.31902	36.9025	0.527807
Overall		3.978651	0.428791	19.93564	2.28747	72.56084	0.808607
Rice Krispie	Sample Jan 22 -20	8.261019	0.104666	71.35831	0	20.18594	0.090057
Eutectic	no significant star burst	4.054371	0.372796	22.09262	2.316966	70.19791	0.965338
Carbide (REPEATED DOWN ONE)		7.629894	0.109223	54.47159	0.899003	36.31311	0.577182
Rice crispie	Sample Jan 22 -20	8.893844	0.115424	72.81736	0	18.08587	0.087502
Eutectic	no significant star burst	3.892175	0.378442	22.23222	2.360132	70.3764	0.760632
Carbide		7.629894	0.109223	54.47159	0.899003	36.31311	0.577182
	Sample jan 22 -150						
Rice Krispie (darker core)	bit of star burst	11.16848	0.058386	81.43832	0	7.325958	0.008852
Rim		7.925805	0.061891	60.86916	0.708506	29.96317	0.471469
Eutectic		4.19121	0.376572	23.91856	2.322969	68.62192	0.568767
Carbide		7.308942	0.038097	55.64883	1.243472	35.17706	0.583604
Overall		4.039621	0.33988	21.5752	2.321151	70.83527	0.88887
	Sample 16-40-1						
Darker core of ricecrispie	Star burst	11.49886	0.036648	82.30617	0	6.158322	0
Rice Krispie		8.178703	0.075075	75.53164	0	16.1563	0.058288
Rim		7.659723	0.034896	55.9645	1.257486	34.45922	0.624169
Eutectic		4.790862	0.317199	26.71096	2.370317	64.98909	0.821569
Carbide		7.550408	0.090405	54.83783	1.55928	35.31795	0.644131
	Sample 16-4-02						
Rice Krispie	no star	8.455376	0.057896	71.1343	0	20.33706	0.015367
Eutectic		4.765466	0.343698	25.5115	2.482104	66.04544	0.851792
Rice Krispie (has darker core is w	Starburst	11.79311	0.030286	82.35658	0	5.820023	0
Eutectic		4.488604	0.433299	24.12329	2.554132	67.53604	0.864638
Eutectic		4.183582	0.326686	21.89921	2.654512	70.04976	0.886251
Rice crispie	no starburst	8.455376	0.057896	71.1343	0	20.33706	0.015367
Eutectic		4.89239	0.379014	26.29216	2.568327	65.07873	0.789378
RiceCrispy (weird one)		8.316088	0.036623	75.21476	0	16.40495	0.027585
larger area of rice crispy		6.36556	0.267128	42.58775	2.927784	45.50139	2.350396
Eutectic (where some what star shaped)		4.219141	0.340612	22.26254	2.571192	69.913	0.693514
eutectic not star shaped		5.465425	0.282761	30.80933	2.293885	60.35312	0.795486

B. First Analysis of composition differences in SEM
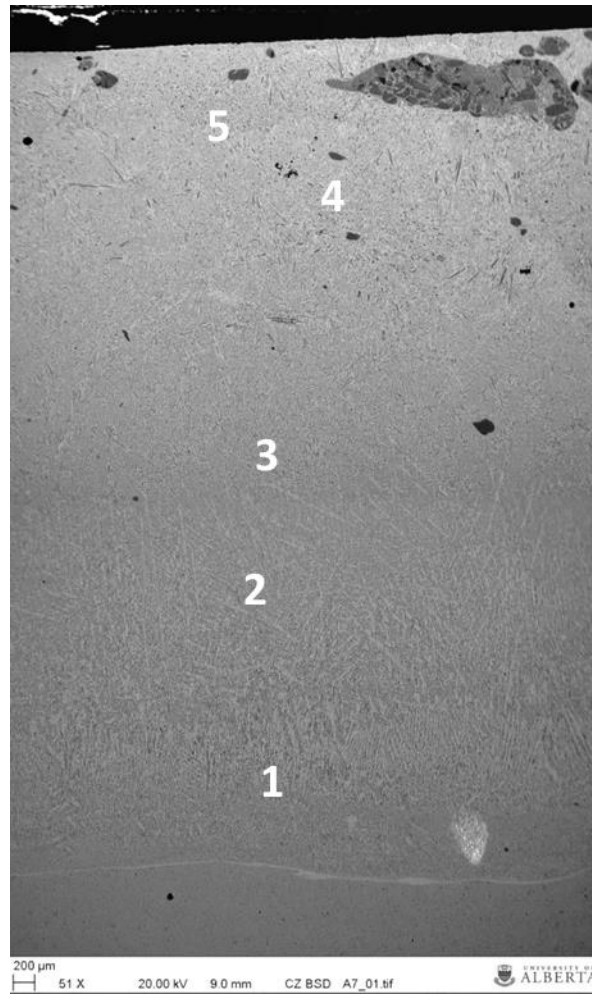
Figure 10-1: Sample A-7

	Point 1	Point 2	Point 3	Point 4	Point 5
Element	[wt.%]	[wt.%]	[wt.%]	[wt.%]	[wt.%]
Iron	77.16	76.44	53.67	67.52	49.6
Chromium	11.5	10.37	22.65	19.13	31.13
Carbon	2.88	3.75	5.97	3.87	6.09
Element	[norm. at.	[norm. at.	[norm. at.	[norm. at.	[norm. at.
Iron	64.44	62.1	43.66	55.96	42.64
Chromium	10.32	9.04	19.79	17.03	28.75
Carbon	11.17	15.74	22.57	14.93	24.33

155

C. Microstructure of areas used to get composition from enlarged
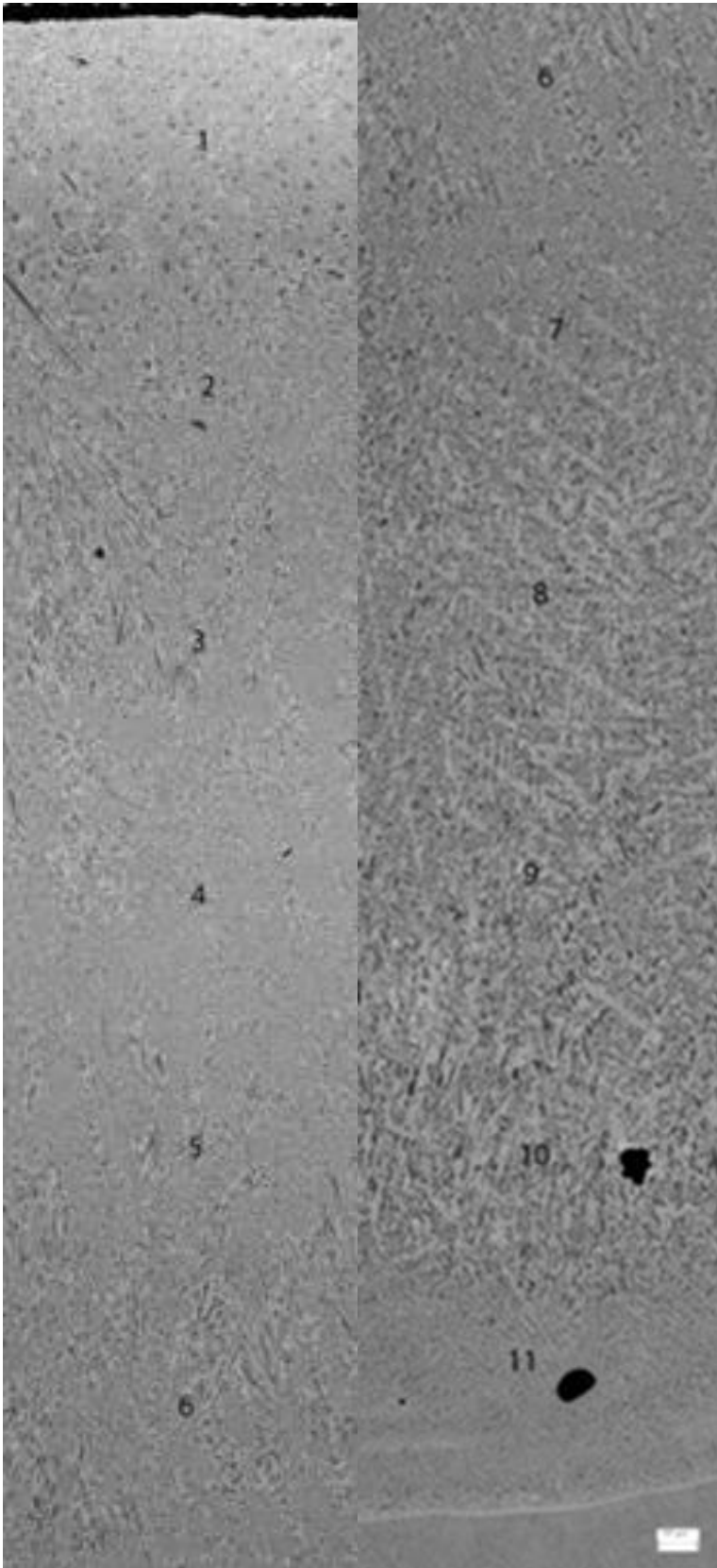
D. Data for ICP Analysis

%wt	Old 1/4 on 1/4					
	ICP			SEM		
	Top	Middle	Bottom	Top	Middle	Bottom
Chromium	26.2	23.7	22.8	23.17835	22.76673	22.35495
Iron	69.3	74	74.1	70.41804	70.89967	71.1001
Manganese	1.95	1.9	1.85			
Molybdenum	0.819	0.794	0.801	0.786096	0.73485	0.82341
Boron	0.21	0.21	0.21			
Phosphorous	0.01	0.01	0.01			
Silicon	0.388	0.366	0.396	0.273007	0.21803	0.238735
Carbon	3.17	3.02	2.82	5.344503	5.380723	5.482804
Sulphur	<0.05	<0.05	<0.05			
Distance from surface um	765	2561	4202	765	2561	4202

%wt	Base					
	ICP			SEM		
	Top	Middle	Bottom	Top	Middle	Bottom
Chromium	26.7	24	23.3	24.77478	23.54815	24.52558
Iron	68.8	71.4	73	65.70015	68.01746	68.90142
Manganese	2.39	2.27	2.26			
Molybdenum	0.799	0.746	0.75	0.835146	0.833265	0.762479
Boron	0.24	0.23	0.23			
Phosphorous	0.02	0.02	0.02			
Silicon	0.529	0.565	0.54	0.339241	0.374473	0.415335
Carbon	3.41	3.19	3.11	8.350682	7.226653	5.395182
Sulphur	<0.05	<0.05	<0.05			
Distance from surface um	725	2361	3623	725	2361	3623

E. Line Scan Data

Position	sition [µm]	Fe	Cr	Mn	Mo	Si	C
0	0	79.67807	14.94928	1.419026	0	0.857972	3.09565
1	0.464385	81.5366	12.38356	2.638965	0.792998	0.359422	2.288455
2	0.92877	77.66815	15.62922	1.407316	0.130294	0.389117	4.775902
3	1.393154	43.53299	47.89967	0.446243	0.156213	0.080264	7.884621
4	1.857539	38.25967	54.58845	1.064226	0.205238	0.174604	5.707811
5	2.321924	34.94652	55.10339	1.315303	0.254342	0.066471	8.313979
6	2.786309	34.19696	58.00851	1.885742	0	0	5.908793
7	3.250693	36.30157	57.81564	2.696835	1.037961	0	2.148003
8	3.715078	34.72939	55.13841	2.737056	0.499021	0	6.896119
9	4.179463	34.68797	56.51366	0.658404	0.761639	0.167457	7.210867
10	4.643848	35.17419	54.97834	2.633921	0.156913	0	7.056633
11	5.108233	32.97884	53.74463	1.671813	1.091919	0.144444	10.36836
12	5.572617	33.73442	60.70737	1.132885	1.303495	0.171533	2.950292
13	6.037002	38.37753	53.36696	1.129855	0.64885	0.237159	6.239636
14	6.501387	32.27962	61.13506	0.924749	0.940405	0.148332	4.571832
15	6.965772	35.9326	56.16941	0.787016	0.164498	0.218893	6.727584
16	7.430156	30.986	58.14383	0.809248	0.575973	0.18089	9.304058
17	7.894541	36.40252	56.94458	0.836012	0.328741	0.260192	5.227955
18	8.358926	38.37427	54.27554	0.854212	0.1125	0	6.383482
19	8.823311	32.62751	55.25797	1.381774	0.221714	0.233045	10.27799
20	9.287696	34.86733	54.09492	2.258183	1.145838	0.087033	7.546697
21	9.75208	45.97493	43.62157	1.840866	1.623088	0.180319	6.759228
22	10.21647	64.33895	28.81909	1.756841	1.426031	0.437685	3.221394
23	10.68085	79.4206	14.78235	1.762794	2.161605	0.813456	1.059196
24	11.14523	84.40843	13.1464	1.376662	0	0.444421	0.624092
25	11.60962	81.33612	15.39347	0.562426	0.613449	0.235984	1.85855
26	12.074	81.75295	12.92157	2.506559	0.099515	0.377843	2.341564
27	12.53839	81.6836	13.6433	1.677866	0.512442	0.497087	1.985701
28	13.00277	74.51384	21.13349	2.723369	0.529175	0.528722	0.571401
29	13.46716	49.10823	42.69706	1.992854	0.392791	0.478007	5.331052
30	13.93154	30.51271	59.04373	2.789489	1.163102	0.074299	6.41667
31	14.39593	31.38645	59.6328	1.317012	0.531747	0.165906	6.966085
32	14.86031	34.60568	56.28911	2.62601	0.343875	0.216039	5.919287
33	15.3247	34.79147	59.30412	0.436125	0.374639	0.376902	4.716746
34	15.78908	32.45319	58.462	1.109641	1.103689	0.051652	6.819828
35	16.25347	31.75679	57.97079	0.301923	0.893051	0.122809	8.954642
36	16.71785	31.09643	59.32487	1.65514	1.14179	0.159004	6.622766
37	17.18224	37.37285	50.89023	1.998554	0.539597	0.123798	9.074973
38	17.64662	32.38478	58.41353	2.446503	0.830154	0.342939	5.582093
39	18.11101	32.96951	55.55936	0.482047	1.160846	0	9.828237
40	18.57539	37.108	53.66073	2.337455	0.524099	0.195679	6.174043
41	19.03978	72.78171	23.52388	1.22675	1.299948	0.396274	0.771443
42	19.50416	80.5063	14.3968	1.279013	0.598237	0.709421	2.510226
43	19.96855	81.10024	13.39687	1.444895	0.389175	0.827387	2.841436
44	20.43293	78.4278	17.67442	1.333133	0.524261	0.644593	1.395797
45	20.89731	49.49609	40.19987	4.306466	0.819795	0.286055	4.891731
46	21.3617	70.21709	23.32551	2.422423	0.911194	0.206642	2.917139
47	21.82608	82.43143	14.71393	2.065087	0	0.348614	0.440937
48	22.29047	83.44063	13.57702	1.018843	0.746043	0.36972	0.847735
49	22.75485	84.51384	12.70848	0.101599	0	0.349015	2.327066
50	23.21924	82.03156	14.28467	1.81122	0	0.844763	1.027788

51	23.68362	58.17804	34.07209	0.106195	0.109712	0.297218	7.236746
52	24.14801	34.90835	55.62256	2.993889	0.603478	0.108024	5.763702
53	24.61239	34.09035	56.47783	1.570025	0.414363	0.326597	7.120842
54	25.07678	34.80732	54.99851	3.030016	0.818445	0.340415	6.005299
55	25.54116	30.15361	57.14956	2.107669	0	0.232249	10.35691
56	26.00555	33.0503	58.38613	1.906216	0.535468	0.153028	5.96886
57	26.46993	36.89892	55.78319	2.154983	0.222811	0.235979	4.704116
58	26.93432	35.72135	57.15827	0.642942	0.703742	0.280783	5.492918
59	27.3987	31.22612	56.74227	1.275432	0.13455	0.275814	10.34582
60	27.86309	34.99742	58.45582	1.126709	0.155577	0.180039	5.08444
61	28.32747	33.78518	56.50069	0.264028	0	0.086802	9.363295
62	28.79186	34.90673	54.36795	0.963403	0.954854	0.23344	8.573625
63	29.25624	36.68598	52.56262	3.664283	0.822983	0.474823	5.78931
64	29.72063	43.97401	48.08813	2.9384	1.214833	0.081669	3.702958
65	30.18501	68.79622	25.66636	1.959352	0.161806	0.200692	3.215565
66	30.6494	82.68945	14.33614	1.364343	0.338309	0.232259	1.039499
67	31.11378	81.42329	14.64147	1.315293	0.256257	0.312139	2.051547
68	31.57816	80.30909	13.80056	1.662152	1.242341	0.752154	2.2337
69	32.04255	75.88287	18.09903	1.819188	0.177008	0.474129	3.547778
70	32.50693	37.62603	50.86132	0.64106	0.234745	0.211991	10.42486
71	32.97132	32.82523	59.58994	1.376598	0.463453	0	5.744771
72	33.4357	33.3961	58.15193	2.237488	0.124066	0	6.090424
73	33.90009	34.65821	59.01461	0	0.967182	0.197244	5.162748
74	34.36447	33.80286	55.54707	1.590082	0.326371	0.153542	8.580082
75	34.82886	34.40726	58.63318	0.773171	0.625954	0.185707	5.374734
76	35.29324	35.23898	52.15416	3.888965	0.688507	0	8.02939
77	35.75763	36.85979	54.58077	0.502326	0.240578	0	7.816536
78	36.22201	34.40153	53.84835	0.966642	0	0.221155	10.56232
79	36.6864	34.27175	55.30618	2.70151	0.83544	0.131594	6.753524
80	37.15078	36.62759	56.69181	1.279546	0.644225	0.052916	4.703911
81	37.61517	34.91037	56.21076	3.654718	0.48607	0	4.73809
82	38.07955	34.60061	56.21995	1.335017	1.628446	0.079255	6.136722
83	38.54394	33.88631	55.53962	2.401776	0.162812	0	8.009489
84	39.00832	35.22799	54.80353	1.506577	1.666484	0.217364	6.578056
85	39.47271	35.28149	55.96833	1.629192	0.268412	0.030157	6.822422
86	39.93709	35.50675	52.92639	1.648558	0.970638	0	8.947663
87	40.40148	33.47549	57.35279	2.051607	0.951338	0.069374	6.099398
88	40.86586	37.07709	57.64414	1.892861	0	0	3.385906
89	41.33025	37.00557	57.10708	1.463601	0.640801	0	3.782943
90	41.79463	32.29084	58.38548	2.351741	0.330595	0	6.641348
91	42.25901	35.86164	55.65572	1.75461	0.657272	0.183309	5.887455
92	42.7234	40.12243	51.70136	4.015995	0.042424	0.144797	3.972992
93	43.18778	77.12912	18.54233	2.102116	0.190703	0.233432	1.802295
94	43.65217	84.96768	12.35467	1.802398	0	0.613525	0.261728
95	44.11655	68.47235	24.06939	0.921197	0.971733	0.16515	5.400185
96	44.58094	53.01996	39.00912	1.294479	0.696409	0.326471	5.653566
97	45.04532	53.97464	38.59685	1.386217	0	0.208866	5.833423
98	45.50971	64.61934	29.33326	0.479075	0	0.143392	5.424935
99	45.97409	76.80717	17.35402	1.601166	0.623838	0	3.613807